

ABSTRACT

Title of Dissertation: ROCK FLUID INTERACTION AND ITS
EFFECT ON BRITTLE ROCK
DEFORMATION

Tiange Xing
Doctor of Philosophy
2019

Dissertation directed by: Professor Wenlu Zhu
Department of Geology

Accurate assessments of Earth's dynamic processes, which produce earthquakes and volcanoes, require better understanding of rock deformation. All rocks, to some extent, contain pores. In the Earth's crust, the pore space is usually filled with water and other fluids such as CO₂. Interactions between a rock and the interstitial fluids can significantly alter the physical and chemical properties of the rock and consequently how the rock deforms. My dissertation research focuses on how fluid-rock interactions affect brittle rock deformation including fracture growth and frictional slip that are central to earthquake mechanics, energy exploration and waste deposits.

I use both conventional experimental methods and the state-of-the-art synchrotron-based X-ray tomography to quantify the changes of mechanical properties and 3-dimensional pore structures of deforming rocks. The two major findings are: 1) olivine carbonation reactions, in which carbon dioxide is chemically incorporated into

silicates to form carbonate, can produce nano- to micro-scale dissolution channels as well as expansion cracks in the host rocks, suggesting that olivine carbonation can be self-sustaining despite its large positive volume change. By identifying the mechanisms that generate porosity during olivine carbonation, this work provides new insights into the application of CO₂ mineral sequestration; 2) increasing pore fluid pressure impedes fracture propagation in intact rocks and stabilizes slip along gouge-bearing faults. The stabilizing effect is positively correlated with pore volume increases, suggesting that dilatant hardening is responsible for the observed strengthening. These results provide new physical understanding of the observed spatial correlation between slow slip events and high pore fluid pressure in many subduction zones where tsunami-generating mega earthquakes occur.

ROCK FLUID INTERACTION AND ITS EFFECT ON BRITTLE ROCK
DEFORMATION

by

Tiange Xing

Dissertation submitted to the Faculty of the Graduate School of the
University of Maryland, College Park, in partial fulfillment
of the requirements for the degree of
Doctor of Philosophy
2019

Advisory Committee:
Professor Wenlu Zhu, Chair
Professor Mong-Han Huang
Professor Laurent G. J. Montesi
Dr. Philip M. Piccoli
Professor Amir Riaz

© Copyright by
Tiange Xing
2019

Preface

The Swiss-American geologist Louis Agassiz once said, “The world is the geologist’s great puzzle-box; he stands before it like the child to whom the separate pieces of his puzzle remain a mystery till he detects their relation and sees where they fit, and then his fragments grow at once into a connected picture beneath his hand.”

Rock deformation is a complex puzzle-box for all geologists. Centuries of studies have been devoted to the topic to uncover the mystery of its mechanism. The deformation of rock can also be affected by many factors. The interstitial fluid, which is ubiquitous throughout the crust, has significant effect on the deformation of rocks. In this dissertation, I have used both conventional and unconventional laboratory approaches to “find the connection between separate pieces” of the rock deformation puzzles to be able to glance into the picture of the fluid-rock interaction both chemically and physically. The work from this study helps in understanding a tip of the iceberg about the rock deformation mechanisms.

Dedication

This dissertation is dedicated to everyone
who has played a part in my life.

You either
give me the hard times,
help me through the hard times, or
drink and laugh with me
after they all pass.

Every one of you has helped in
shaping a part of who I have become.

Acknowledgements

I would like to express my gratitude to everyone who has participated in my academic life for their guidance, comfort and continuous support.

I would like to give my biggest appreciation to my family for their unconditional love. They are the strongest support for me on pursuing my career.

I would like to thank my PhD advisor, Wenlu Zhu for her years of wisdom and energy. Her being a role model in science has inspired and shaped me to become a better scientist. I also thank all faculty members at UMD for the inspiration and help throughout my PhD. I also thank my Master's advisor, Florian Fuisseis for his support during my PhD application and making my academic journey to the U.S. happen.

The four-year long graduate school life became a lot more fun and enjoyable with all the friends and colleagues. I thank Thomas Tamarkin profusely for his always in-time support in and outside the lab. I would also like to thank Harry Lisabeth, Will Kibikas, Jiangyi Hou, Melodie French, Xianghui Xiao and Ted Koczynski for their help at the start of my PhD project. I also thank Takamasa Kanaya, Zach Zega, Ben Belzer and Dashaun Horshaw for the extra hands and eyes they lent me in the lab.

I thank Zixiao Liu and Yishan Xu, my friends since middle school who are also UMD fellows. I also thank Huan Cui, Ming Tang, Hailong Bai, Chao Gao, Xizheng Wang, Quancheng Huang, Meng Guo, Goeun Ha, Kristel Izquierdo, Israel Martinez, Mark and Maggie McAdam, Hui Zhang, Yong (Kevin) Yang, Ziqin (Grace) Ni, Manyi Wang, Bin Xia, Songjie Wang for all the fun and inspiring interactions. My thanks extend to the graduate family at UMD.

And of course, nothing comes free in life and certainly not cheap regarding to scientific research. The work of my PhD study was funded by the Department of Energy, Office of Science, the Office of Basic Energy Sciences, Chemical Sciences, Geosciences, & Biosciences Division under award no. DE-FG-0207ER15916, and by the National Science Foundation under grant no. EAR-1551300 and EAR-1761912. My study was also supported by several fellowship awards from the University of Maryland, including the Ann G. Wylie Dissertation Fellowship, Graduate School Summer Research Fellowship, Green Fellowship in Global Climate Change and Dean's Fellowship.

Some of my trips to conferences, workshops and scientific expeditions were supported by travel grants from Earth System Science Interdisciplinary Center at the University of Maryland, the Gordon Research Conferences, the University of Oslo and the International Continental Scientific Drilling Program, Oman Drilling Project. I thank them for the opportunity of traveling, some of which have contributed significantly to my PhD work.

Table of Contents

Preface.....	ii
Dedication.....	iii
Acknowledgements.....	iv
Table of Contents.....	vi
List of Tables.....	viii
List of Figures.....	ix
Chapter 1: Introduction.....	1
1.1 Brittle Rock Deformation.....	1
1.2 Rock-fluid Interaction.....	5
1.3 Research Outlines.....	9
Chapter 2: Generating Porosity during Olivine Carbonation via Dissolution Channels and Expansion Cracks.....	10
Abstract.....	10
2.1 Introduction.....	11
2.2 Experimental Setup.....	17
2.2.1 Sample Configuration.....	17
2.2.2 Micro- and Nano-tomography.....	20
2.2.3 Image Processing Procedures.....	22
2.3 Data Analysis and Results.....	24
2.3.1 Dissolution in the LGC Sample.....	25
2.3.2 Lack of Precipitation in the LGC Sample.....	26
2.3.3 Porosity Evolution of LGC Compared to SGC.....	28
2.3.4 Fractures in LGC vs. SGC.....	31
2.3.5 Dissolution and Fracturing of Individual Olivine Grain.....	33
2.4 Discussion.....	37
2.4.1 Dissolution and Etch-pitting.....	37
2.4.2 Reaction-induced Fracturing.....	39
2.4.3 Coupled Mechanisms of Dissolution and Precipitation-driven Fracturing.....	45
2.5 Conclusions.....	47
Chapter 3: Stabilizing Effect of High Pore Fluid Pressure on Slip Behaviors of Gouge-bearing Faults.....	49
Abstract.....	49
3.1. Introduction.....	50
3.2. Experimental Procedures.....	54
3.3. Results.....	60
3.3.1 Frictional Strength & Friction Coefficient from CPP Experiments.....	60
3.3.2 Velocity Dependence Factor (a-b) from CPP Experiments.....	62
3.3.3 Characteristic Displacement from CPP Experiments.....	65
3.3.4 Pore Volume Fluctuation from CPP Experiments.....	66
3.3.5 Pore Fluid Pressure Fluctuation from CPV Experiments.....	68
3.3.6 Microstructure of Deformed Gouge.....	71
4. Discussion.....	72
3.4.1 Frictional Behavior Change with Increasing Pore Fluid Pressure.....	72

3.4.2 Pore Volume Change during Shear.....	73
3.4.3 Pore Fluid Pressure Dependence of (a-b)	75
3.4.4 Characteristic Displacement (D_c).....	79
3.4.5 Slow Slip in Serpentine.....	79
3.5. Conclusions.....	81
Chapter 4: Pressure Dials to Tune Slip Events between Slow and Fast	86
Abstract.....	86
4.1 Introduction.....	86
4.2 Sample Configuration and Experimental Procedures	89
4.3 Results.....	92
4.3.1 Pressure Dependence of Slip Events.....	92
4.3.2 Stress Drop and Stress Drop Durations	97
4.3.3 Slip Distance and Elastic Energy	99
4.3.4 Moment Magnitude.....	101
4.3.5 Effect of Slip Velocity on Slip Events	104
4.4 Discussion.....	105
4.4.1 Pressure Dependence of Stick-slip Events.....	105
4.4.2 Elastic Energy and Energy Release Rate	107
4.4.3 Slip Velocity during Slip Events.....	107
4.4.4 Spectrum of Fault Slip Behavior.....	109
4.5 Conclusion	111
Chapter 5: Role of Pore Fluid Pressure on Faulting Stability in Various Crystalline Rocks.....	114
Abstract.....	114
5.1 Introduction.....	115
5.2 Sample Configuration and Experimental Procedures	117
5.3 Results.....	121
5.3.1 Mechanical Strength	121
5.3.2 Fault Nucleation and Propagation.....	123
5.3.3 Micro-structure	126
5.4 Discussion.....	128
5.4.1 Stability of Fault Rupture.....	128
5.4.2 Mechanism of Fault Stabilization	129
5.4.3 Micro-cracks Development.....	131
5.4.4 Stabilization Effect of Different Sample Composition	132
5.4.5 Faulting Stability with the Presence of High Pore Fluid Pressure.....	133
5.5 Conclusion	134
Appendix A. List of Symbols	140
Appendix B. Friction Data Processing.....	142
Appendix C. Data Corrections	144
Appendix D. Image Data Processing Code (MATLAB)	146
Bibliography	152

List of Tables

Table 3.1: Axial displacement rate for the step tests during each experiment	59
Table 3.2: Summary of experiments	59
Table 4.1: Pressure conditions and yield stress for each experiment.	92
Table 5.1: Experimental conditions of all tests.....	120

List of Figures

Figure 1.1: Friction responses to changes in slip velocity.	5
Figure 2.1: Illustration of the mechanisms of reaction-induced fracturing during olivine-fluid interaction.	15
Figure 2.2: Illustration of sample configuration.	18
Figure 2.3: Experimental setup for dynamic microtomography.	23
Figure 2.4: Positions of the subvolumes in the cup wall of a) SGC and b) LGC, where quantitative 3D microstructure analyses were performed.	23
Figure 2.5: Reconstructed images showing the cross-section view of the sample undergoing olivine carbonation.	24
Figure 2.6: a) Dissolution features in the cross-sectional images of the LGC sample. 3D examination reveals that these dissolution features (blue arrowheads) are associated with planar fractures (yellow arrowheads) appeared in b) the radial and c) the tangential section images.	25
Figure 2.7: Best fits for the grey value distribution histograms of the sample at different stages of the reaction in a) subvolume 4 from LGC sample and b) subvolume 2 from SGC sample.	27
Figure 2.8: Comparison of porosity evolution in LGC (this study) versus SGC reported by Zhu et al. (2016).	29
Figure 2.9: Porosity profiles of a) LGC and b) SGC along the radial direction of the sample cup.	30
Figure 2.10: The 3D geometry (in red) of a) dissolution-assisted fracture in LGC is distinctively different from b) the stretching-induced fractures in SGC.	32
Figure 2.11: Reconstructed images from the nanotomography data of the SGC sample's cup wall demonstrate the existence of etch-pits and dissolution channels (white arrows) formed in the olivine grain.	34
Figure 2.12: Network of microcracks (red) in the reaction olivine cup wall from SGC shows a polygonal pattern.	34
Figure 2.13: Volume change of an individual olivine grain (total volume of olivine and precipitates) during carbonation reaction in the SGC experiment.	36
Figure 2.14: Pore distribution within the subvolumes from SGC sample.	43

Figure 2.15: Illustration of porosity generation mechanisms during the olivine carbonation reactions.	46
Figure 3.1: Illustration of the slip events distribution within the subduction zone.	50
Figure 3.2: Sample and equipment configuration.	55
Figure 3.3: a) Friction coefficient of antigorite (green), olivine (blue), quartz (yellow) and chrysotile (red). b) Frictional responses to changes in slip rate.	61
Figure 3.4: Effect of pore pressure on the velocity dependence factor ($a-b$) of all tested gouges a) antigorite; b) olivine; c) quartz; d) chrysotile from velocity increase steps (0.1 to 1 $\mu\text{m/s}$).	64
Figure 3.5: Box plot of the effect of strengthening on ($a-b$) from pore pressure.	65
Figure 3.6: a) Characteristic displacement (D_c) of gouge materials in response to slip velocity change at different steps. b) Characteristic displacement (D_c) of antigorite in response to slip velocity change at different pore pressure conditions.	66
Figure 3.7: Pore volume fluctuation of antigorite (green) and quartz (yellow) during deformation.	67
Figure 3.8: Pore pressure fluctuations of antigorite during locked volume experiments.	69
Figure 3.9: Pore fluid pressurization rate of antigorite (green), olivine (blue), quartz (yellow) and chrysotile (red), during locked volume experiments.	70
Figure 3.10: Micro-structures of antigorite (Atg) and olivine (Ol) gouge at different pore pressure conditions.	72
Figure 3.11: Dilatant hardening mechanism illustration.	76
Figure 3.12: The differential stress vs axial displacement for all tested gouges.	83
Figure 3.13: The velocity dependence factors ($a-b$) of all tested gouge materials deformed at 70 MPa effective pressure.	84
Figure 3.14: Effect of pore pressure on the velocity dependence factor ($a-b$) of all tested gouges a) antigorite; b) olivine; c) quartz; d) chrysotile from all velocity decrease steps (1 to 0.1 $\mu\text{m/s}$).	84
Figure 3.15: Pore volume fluctuation of antigorite (green), olivine (blue), quartz (yellow) and chrysotile (red) during deformation.	85
Figure 4.1: Experimental setup.	90

Figure 4.2: Stress-Strain curves of saw-cut samples deformed at various confinements and pore pressure.	93
Figure 4.3: Effective pressure dependence of slip behavior.	94
Figure 4.4: Pore pressure dependence of stick-slip behavior. Amplitude of stress drops decreases as pore pressure increases.	95
Figure 4.5: Magnitude vs. duration of shear stress drop for individual slip events a) under various confinements and a constant pore pressure of 5MPa; b) under various pore pressures and a constant effective confinement of 70MPa.	98
Figure 4.6: Elastic strain energy release calculation during individual slip events. .	100
Figure 4.7: Elastic energy release vs. slip velocity for individual slip events. a) under various confinements and a constant pore pressure of 5 MPa; b) under various pore pressures and a constant effective confinement of 70 MPa.	101
Figure 4.8: Histogram of moment magnitude distribution for individual slip events a) under various confinements and a constant pore pressure of 5 MPa; b) under various pore pressures and a constant effective confinement of 70 MPa.	103
Figure 4.9: Frequency of moment magnitude for individual slip events a) under various confinements and a constant pore pressure of 5 MPa; b) under various pore pressures and a constant effective confinement of 70 MPa.	104
Figure 4.10: Magnitude of shear stress drop during slip events controlled by both effective confinement and pore pressure.	106
Figure 4.11: a) Slip velocity measurement of individual slip events with comparison to other laboratory studies. b) Pressure dependence of slip velocity.	108
Figure 4.12: Synoptic fault slip model of a subduction zone.	111
Figure 4.13: Yield strength of samples as a function of effective confinement ($P_e = P_c - P_f$)	113
Figure 5.1: Experimental setup.	118
Figure 5.2: Plot of differential stress against axial strain.	122
Figure 5.3: Strain data of a) Oman dunite and b) Westerly granite samples deformed at an effective pressure of 10 MPa.	123
Figure 5.4: Stress drop during fracture propagation for a) Oman dunite; b) Oman harzburgite; c) Twin Sisters dunite; d) Westerly granite deformed at an effective pressure of 10MPa and various pore pressures.	124

Figure 5.5: Fault propagation duration of a) Oman dunite; b) Oman harzburgite; c) Twin Sisters dunite and d) Westerly granite at different pore pressures from 10 to 120 MPa.....	125
Figure 5.6: Reflected light image of the microstructures of the fractured a) Twin Sisters Dunite and b) Westerly granite deformed at an effective pressure of 10 MPa and under low (10MPa) and high (120MPa) pore pressure conditions.	127
Figure 5.7: a) Schematics of slip weakening slope and fault stabilities modified from Rice & Rudnicki, (1979). b) Slip weakening slope of Oman dunite sample tested at pore pressure ranges from 10 to 120 MPa.	129
Figure 5.8: Strain gauge data of Oman Harzburgite samples deformed.	135
Figure 5.9: Strain gauge data of Oman Harzburgite samples deformed.	135
Figure 5.10: Reflected light image of microstructures of fractured Oman Dunite deformed at an effective pressure of 10 MPa and under low (10 MPa) and high (120 MPa) pore pressures.....	136
Figure 5.11: Reflected light image of microstructures of fractured Oman Harzburgite deformed at an effective pressure of 10 MPa and under low (10 MPa) and high (120 MPa) pore pressures.....	137
Figure 5.12: Reflected light image of microstructures of fractured Twin Sisters Dunite deformed at an effective pressure of 10 MPa and under low (10 MPa) and high (120 MPa) pore pressures.....	138
Figure 5.13: Reflected light image of microstructures of fractured Westerly granite deformed at an effective pressure of 10 MPa and under a) low (10 MPa) and b) high (120 MPa) pore pressures.	139
Figure 5.14: Slip weakening of all tested samples at pore pressure ranges from 10 to 120 MPa.....	139

Chapter 1: Introduction

1.1 Brittle Rock Deformation

Earth is a dynamic planet. Rocks are generally subject to substantial mechanical, chemical and thermal loads, and quantitative knowledge of rock deformation is critical for better assessments of Earth's dynamic processes. Experimental rock deformation provides vital information on the evolution of mechanical properties of deforming rocks and elucidates deformation mechanisms that can be used to extrapolate laboratory observations to natural processes.

This study focuses on brittle deformation and aims at improving our understanding of the nature and controls on rock strength, fracture and friction. Studying brittle deformation has many geological and geotechnical implications, including earthquake hazard mitigation, energy exploration, waste disposal, and carbon sequestration.

Brittle fracture occurs when the stress applied on a material exceeds the critical strength. This is well described by the Mohr-Coulomb failure criterion (Jaeger, 1969; Rabinowicz, 1965):

$$|\tau| = \mu\sigma_n + c \quad (1.1)$$

where τ is the shear stress resolved on the resulted fracture plane, σ_n is the normal stress applied to the plane, μ is the coefficient of interal friction, and c describes the cohesion.

It has been well established that the failure process of intact rocks involves the growth of defects such as microcracks. When the crack density becomes sufficiently

high, the cracks nucleate and coalesce to form the macroscopic fault plane (Lockner, 1993; Peng & Johnson, 1972; Reches & Lockner, 1994; Sammis & Ashby, 1986).

The failure criterion can also be used to describe the frictional sliding, in which the cohesion becomes zero, and μ is the coefficient of friction which is similar for most rocks with a range of $0.6 \leq \mu \leq 0.85$ according to Byerlee's Law (Byerlee, 1978). With the exception of clay minerals, Byerlee's law is applicable to most rock types in the absence of fluids. Clay minerals and hydrated mineral phases have lower frictional strength (Kronenberg et al., 1990; Diane E. Moore et al., 1996, 1997, 2004; Morrow et al., 1992).

The frictional behavior is described by the empirical rate- and state-friction law (Dieterich, 1979; Ruina, 1983). The dependence of the dynamic friction coefficient on sliding velocity and other variables can be described as:

$$\mu_s = \mu_1 + a \ln\left(\frac{v_2}{v_1}\right) + b \ln\left(\frac{v_1 \theta}{D_c}\right) \quad (1.2)$$

$$\frac{d\theta}{dt} = 1 - \frac{\theta v}{D_c} \quad (1.3)$$

where μ_1 is the steady-state friction coefficients and μ_s is the dynamic friction coefficients at slip velocity of v_1 and v_2 respectively, a and b are material properties, D_c is the displacement over which friction evolves with slip, and θ is the state variable.

For steady-state friction:

$$\frac{d\theta}{dt} = 0; \quad e.g. \quad \theta = \theta_2 = \frac{D_c}{v_2} \quad (1.4)$$

Therefore, friction changes as velocity changes from v_1 to v_2 , and can be expressed as:

$$\mu_s = \mu_1 + a \ln\left(\frac{v_2}{v_1}\right) + b \ln\left(\frac{v_1 \theta_2}{D_c}\right) \quad (1.5)$$

e.g.

$$\mu_s = \mu_1 + a \ln\left(\frac{v_2}{v_1}\right) + b \ln\left(\frac{v_1}{v_2}\right) = \mu_1 + (a - b) \ln\left(\frac{v_2}{v_1}\right) \quad (1.6)$$

It has been shown that dynamic friction might change in response to a change in slip velocity. The effect of velocity on the friction coefficient is complicated and the net steady state effect depends on the relative contributions from a and b . If the dynamic friction (μ) is defined as steady-state friction at velocity v , then:

$$a - b = \frac{d\mu}{d(\ln v)} \quad (1.7)$$

When $a-b < 0$, then a decrease in friction coefficient takes place when the sliding velocity increases. This is termed “velocity-weakening” (Figure 1.1). It is well established that the onset of instabilities, which might lead to the generation of earthquakes, is inextricably related to the reduction of frictional resistance with increasing slip velocity (i.e. velocity-weakening effects). Conversely, if $a-b > 0$, friction is “velocity-strengthening” and only stable sliding is possible.

In general, by examining the dependency of friction on steady-state sliding velocity, the stability of friction and earthquake occurrence on a fault can be inferred. If the friction increases with sliding velocity (velocity-strengthening) then the sliding will be stable and no earthquakes can be generated; if the frictional resistance decreases with velocity (velocity-weakening), then unstable slip and earthquakes can be expected. There is also a dependence of friction on the slip displacement/ characteristic displacement (D_c), following changes in velocity. The process that causes static friction to increase with static time is the same one that causes velocity-weakening. This is

sometimes called the evolution effect since the friction evolves with time and displacement (Beeler et al., 1994; Dieterich, 1972; Marone, 1998).

However, whether instability can occur also depends on the stiffness of the system surrounding a fault zone k , and the critical stiffness of the fault zone material k_c . This is described by Ruina (1983) using the following equation:

$$k_c = \frac{-(a-b)\sigma_n}{D_c} \quad (1.8)$$

Instability can only occur when $k_c > k$ (Rice & Ruina, 1983). The stiffness depends on several parameters including friction parameters ($a-b$), characteristic displacement D_c , and the effective normal stress σ_n . The elastic stiffness model represents simplified elastic and frictional conditions, but is consistent with more sophisticated models of earthquake nucleation (Liu & Rice, 2007). Numerical studies and laboratory investigations have also demonstrated the existence of the transitional behavior between stable to unstable behavior involving quasi-dynamic, oscillatory sliding behavior when $k_c \approx k$ (e.g., Gu et al., 1984; Leeman et al., 2016; Liu & Rice, 2007; Scholz et al., 1972).

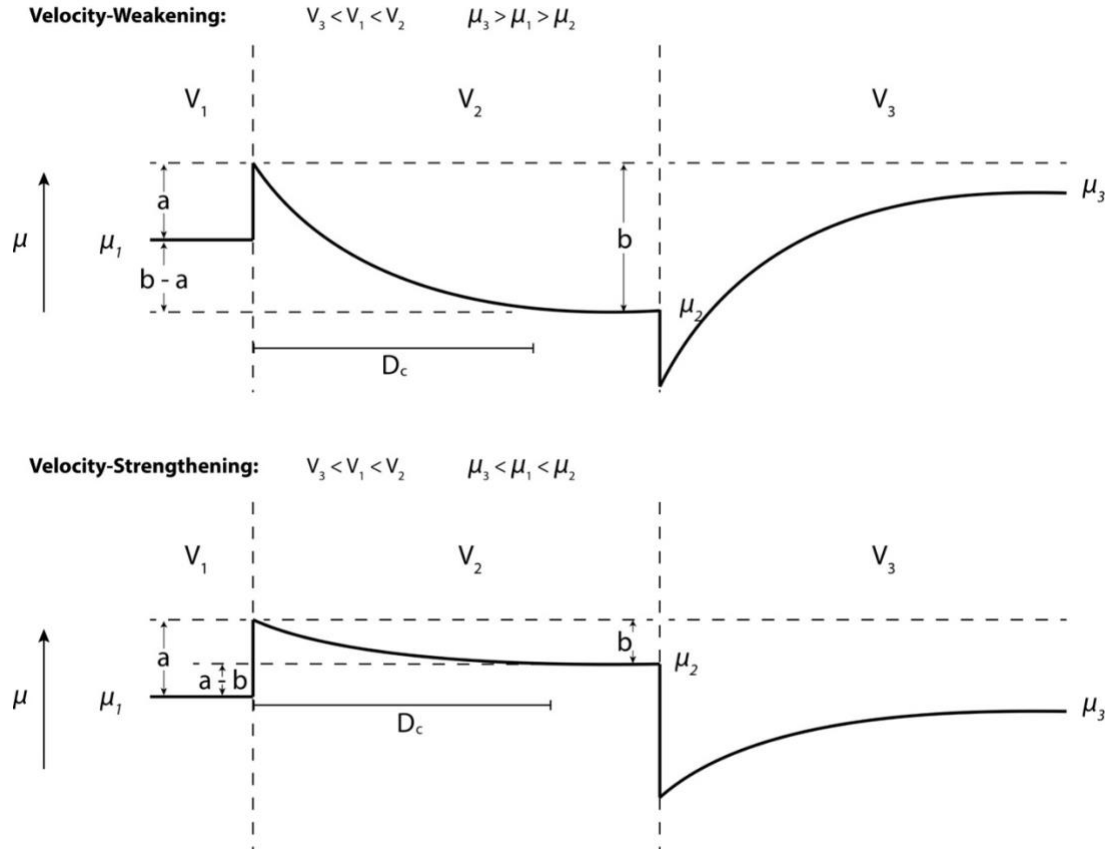


Figure 1.1: Friction responses to changes in slip velocity. a) Velocity weakening behavior where increase in slip velocity is associated with a decrease in the friction coefficient (negative $a-b$). b) Velocity strengthening behavior where increase in slip velocity is associated with an increase in the friction coefficient (positive $a-b$). The characteristic displacement (D_c) is marked by the distance required for the friction coefficient μ to evolve to b/e following a change in slip velocity.

1.2 Rock-fluid Interaction

Within the rock frame, interstitial fluid is ubiquitous. The interstitial fluid can be produced through compaction of sediments (Bredehoeft et al., 1988; Hooper, 1991), dehydration reactions (Hirauchi et al., 2013; Okazaki & Hirth, 2016; Tauzin et al., 2017), etc. Geophysical observations have allowed for the quantification of pore fluid volume and pressure in a variety of tectonic settings (Heise et al., 2013, 2017; Peacock et al., 2011; Saffer, 2017). Available direct measurement of the pore fluid pressure from boreholes at shallow depth show elevated pore fluid pressures of nearly 90% of the

lithostatic pressure (e.g., Davis & Villinger, 2006; Sibson & Rowland, 2003). Seismic studies also reveal anomalous pore fluid pressure within or subjacent to faults (e.g., Bangs et al., 2009; Kato et al., 2010; Kodaira et al., 2004; Park et al., 2002; Park et al., 2010; Song et al., 2009).

Interstitial fluids play an important role in the crustal processes and are inextricably related to tectonics. At depth, the pore fluid can influence melting and have controls over the volcanism in the over-riding plate (e.g., Grove et al., 2009). Studies have also shown that the mechanical behavior of crustal rocks can be significantly affected with the presence of fluid (e.g., Dunning & Miller, 1985; Heard, 1960; Helmons et al., 2016; Rutter & Hackston, 2017). The elevated pore fluid pressure has been used to explain many apparent weakness within fault zones (e.g., Blanpied et al., 1995; Moore et al., 1996; Tembe et al., 2006; Wintsch et al., 1995; Zoback et al., 1987). The presence of these high volume and pressure of pore fluid also seem to be associated with earthquakes. Elevated pore fluid pressure has been interpreted to inhibit shallow seismicity, promote deep and wide seismogenic zones and facilitate the propagation of tsunami-generating mega earthquakes to the trench (Dean et al., 2010; Fagereng & Ellis, 2009; Scholz, 1998). Occurrence of transitional fault slip behaviors such as slow-slip events, very low frequency faulting events and episodic tremors, have also been thought to closely relate to the presence of pore fluid (e.g., Audet et al., 2009; Lowry, 2006; Shelly, 2010; Shelly et al., 2006; Vergnolle et al., 2010). However, to date, there is still a lack of knowledge about the relationship between pore fluid pressure and fault slip modes. In order to produce an accurate model of the crustal dynamics, a large number of constraints regarding the fluid-rock interactions at crustal conditions and

their effect on rock deformation behavior must be obtained from systematic laboratory studies. According to our present knowledge, the interactions between the fluid and rocks can affect the deformation behavior from several aspects, both physically/mechanically and chemically.

Physically, the presence of pore fluid in rocks could alter the local pressure conditions and cause variation in the effective pressure (Handin et al., 1963; Hubbert & Rubey, 1959; Rutter, 1972). The relationship between pore fluid pressure and effective pressure has been well described by the effective pressure law (Terzaghi, 1943):

$$P_e = P_c - P_f \quad (1.9)$$

where P_c is the confinement/overburden pressure and P_f is the pore fluid pressure. The pore fluid pressure counteracts the overburden pressure and reduces the effective pressure and, when combined with the Mohr-Coulomb failure criterion (Jaeger, 1969; Rabinowicz, 1965), would ultimately exert control on the mechanical strength of rocks. Studies show that alteration of the pressure conditions can cause embrittlement of the rock and significantly affect the strength of the rock (e.g., Blanpied et al., 1998; Rice, 1975; Rice & Cleary, 1976). Fluctuations in pore fluid pressure conditions can also activate dilatant hardening and cause strengthening of the deformation (Rice, 1975; Rudnicki, 1984; Rudnicki & Chen, 1988).

Chemically, the addition of fluid could cause kinetic reduction of fracture energy via absorption of fluid on mineral surfaces (Orowan, 1944; Rutter, 1972), activation of fluid-promoted subcritical crack growth/stress corrosion (Atkinson, 1984; Atkinson & Meredith, 1987; Brantut et al., 2013; Kranz et al., 1982; Rice, 1978) and pressure

solution (Zhang & Spiers, 2005), etc. Numerous studies have been conducted to investigate the effect related to the addition of fluid (Kirby, 1983; Kirby & Kronenberg, 1987; Lisabeth & Zhu, 2015; Paterson & Wong, 2005). Fluid does not only affect the rock deformation by favoring fluid-assisted deformation processes; fluid also reacts with rocks, changes the composition of the rocks and alters the pore structure of rocks (e.g., Kelemen et al., 2013; Kelemen & Hirth, 2012; Lisabeth et al., 2017a; Xing et al., 2018; Zhu et al., 2016). Chemical alteration that can lead to the addition of new phases, has a significant effect on changing the strength of the rock (Dunkel et al., 2017; Kanakiya et al., 2017). The chemical effect of fluids on rock deformation is much more complex and remains an active area of research, but it is clear the chemical effect can significantly contribute to deformation.

In reality, the physical/mechanical and chemical effects from fluid never work independently but are always coupled with each other. For example, fluid flow in a material can be described by Darcy's Law:

$$Q = \frac{-\kappa A}{\eta} \frac{dP}{dx} \quad (1.10)$$

where Q describes the flow rate, κ is the permeability of the sample, η is the viscosity of pore fluid, A is the cross-sectional area of the sample and P is the pressure in the sample with a length of x . Fluid flow can be easily affected by variation in hydraulic properties. Fluid flow can cause perturbations in the local chemical equilibration and allow chemically-activated processes to alter the hydraulic characteristic of the material (e.g., permeability, viscosity, etc.) which, in turn, modifies the mechanical properties.

The physical and chemical interactions between fluid and rocks work in concert and can produce a spectrum of deformation behaviors. Systematic experimental

investigations on the rock-fluid interaction would help in unraveling this coupling between the chemical and mechanical effect of rock-fluid interaction and further understand the deformation mechanisms of earth materials, providing insight into the role of fluid in the dynamics of the tectonics.

1.3 Research Outlines

I focus on the effect of fluid-rock interactions on brittle rock deformation, both physically and chemically. Chapter 1 (this Chapter) describes the complexity and questions regarding to the mechanism of fluid-rock interactions and their control on the rock deformation and the geological and geotechnical implications of this study. Chapter 2 discusses the effect of chemical alteration on olivine dominated rocks and shows the effect of alteration on the pore structure evolution of the rock which eventually affects the strength of the sample. Chapters 3 to 5 describe primarily the physical effect of fluid-rock interaction on the rock deformation by varying pressure conditions. Chapter 3 emphasizes the effect of pore fluid pressure on the frictional behavior of gouge materials under stable and quasi-stable sliding conditions. Chapter 4 focuses on the effect of pore fluid pressure on resting of the unstable frictional slip with the emergence of transitional slow slips behaviors. Chapter 5 demonstrates how the brittle fracturing process can also be altered through the variation in pore fluid pressure conditions.

Chapter 2: Generating Porosity during Olivine Carbonation via Dissolution Channels and Expansion Cracks

Xing, T., Zhu, W., Fusses, F., & Lisabeth, H. P. (2018). Generating porosity during olivine carbonation via dissolution channels and expansion cracks. *Solid Earth*, 9(4), 879–896. <https://doi.org/10.5194/se-9-879-2018>

Abstract

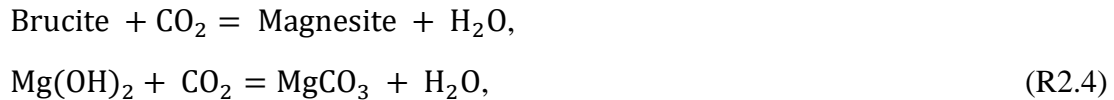
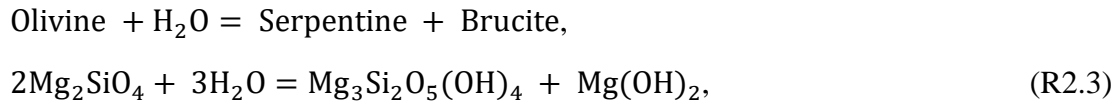
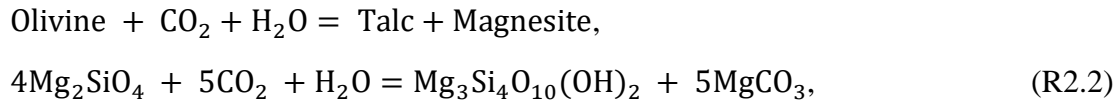
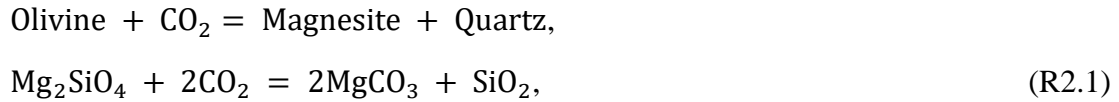
The olivine carbonation reaction, in which carbon dioxide is chemically incorporated to form carbonate, is central to the emerging carbon sequestration method using ultramafic rocks. The rate of this retrograde metamorphic reaction is controlled, in part, by the available reactive surface area: as the solid volume increases during carbonation, the feasibility of this method ultimately depends on the maintenance of porosity and the creation of new reactive surfaces. We conducted in situ dynamic X-ray microtomography and nanotomography experiments to image and quantify the porosity generation during olivine carbonation. We designed a sample setup that included a thick-walled cup (made of porous olivine aggregates with a mean grain size of either ~ 5 or $\sim 80 \mu\text{m}$) filled with loose olivine sands with grain sizes of 100–500 μm . The whole sample assembly was reacted with a NaHCO_3 aqueous solution at 200 °C, under a constant confining pressure of 13 MPa and a pore fluid pressure of 10 MPa. Using synchrotron-based X-ray microtomography, the three-dimensional (3-D) pore structure evolution of the carbonating olivine cup was documented until the olivine aggregates became disintegrated. The dynamic microtomography data show a volume reduction in olivine at the beginning of the reaction, indicating a vigorous dissolution process consistent with disequilibrium reaction kinetics. In the olivine cup

with a grain size of $\sim 80 \mu\text{m}$ in diameter (coarse-grained cup), dissolution planes developed within 30 h, before any precipitation was observed. In the experiment with the olivine cup of $\sim 5 \mu\text{m}$ mean grain size (fine-grained cup), idiomorphic magnesite crystals were observed on the surface of the olivine sands. The magnesite shows a near-constant growth throughout the experiment, suggesting that the reaction is self-sustained. Large fractures were generated as the reaction proceeded and eventually disintegrated the aggregate after 140 h. Detailed analysis show that these are expansion cracks caused by the volume mismatch in the cup walls, between the expanding interior and the near-surface which keeps a nearly constant volume. Nanotomography images of the reacted olivine cup reveal pervasive etch pits and wormholes in the olivine grains. We interpret this perforation of the solids to provide continuous fluid access, which is likely key to the complete carbonation observed in nature. Reactions proceeding through the formation of nano- to micron-scale dissolution channels provide a viable microscale mechanism in carbon sequestration practices. For the natural peridotite carbonation, a coupled mechanism of dissolution and reaction-induced fracturing should account for the observed self-sustainability of the reaction.

2.1 Introduction

Mantle peridotites are exposed widely on the Earth's surface in tectonic settings such as mid-ocean ridges, subduction zones and ophiolites (Escartín et al., 1997a; Fryer et al., 1995). Peridotite is mainly composed of olivine which is unstable at temperatures below $700 \text{ }^\circ\text{C}$ in the presence of water (Evans, 1977) and below $500 \text{ }^\circ\text{C}$ in the presence of CO_2 -rich fluids (Johannes, 1969). The transformation of olivine to serpentine and carbonates due to fluid-rock interaction is extensively observed in peridotite outcrops

(e.g., Beinlich et al., 2012; Falk and Kelemen, 2015; Hansen et al., 2005). Rock deformation experiments have demonstrated that fluid alteration to peridotite can strongly affect the strength and tectonics of the oceanic lithosphere (Deschamps et al., 2013; Moore et al., 1996). Therefore, the study of olivine-fluid interaction is of great importance for understanding the alteration processes of peridotite in a variety of tectonic regions. General peridotite alteration reactions can be formulated as follows (Hansen et al., 2005; Kelemen & Matter, 2008):



Although peridotite weathering reactions occur widely in nature, the rate of olivine carbonation at subsurface conditions is debated. Since the retrograde metamorphic reactions are kinetically fast, the extent of transformation is limited by fluid supply which depends on the accessible fluid pathways. As the hydration and carbonation of olivine results in an up to ~44% increase in solid molar volume (Goff & Lackner, 1998; Hansen et al., 2005; Kelemen & Matter, 2008), carbonation of olivine is generally assumed to be self-limiting: the reaction products would gradually fill up the pore space

and lead to a decrease in the porosity (Emmanuel & Berkowitz, 2006; Hövelmann et al., 2012), which in turn lowers permeability and reduces fluid supply. This negative feedback would ultimately force the alteration to cease. However, naturally occurring completely carbonated peridotites are evidence that these limitations can be overcome. For instance, listvenite is the natural completely carbonated product of peridotite, which is composed of magnesite, quartz and trace minerals (Beinlich et al., 2012; Nasir et al., 2007). This creates a conundrum of how the large extent carbonation can be achieved with the potential self-limitation of reducing fluid pathways.

In order to explain this discrepancy between the theory and the observation, numerous studies have been conducted aiming to find a mechanism to maintain the access for reacting fluid during olivine alteration reactions. In 1985, Macdonald and Fyfe examined naturally altered peridotite and proposed that the large volume change associated with the reaction could generate high local stresses and strains, which would cause episodic cracking. This idea has since been applied to olivine carbonation by Kelemen and Matter (2008), who proposed a positive feedback loop where fractures could be generated during the volume-expanding reaction, porosity and permeability can be maintained or even increased, which in turn would accelerate the carbonation processes (cf. Rudge et al., 2010). In 2011, Kelemen et al. showed that in natural peridotites cross-cutting hierarchical fracture networks filled by syn-kinematic carbonate and quartz veins extend to microscopic scales. These cross-cutting networks indicate coeval carbonate crystallization and fracturing. Several studies also showed that the forces generated by the volume increase should be enough to fracture peridotite (Iyer et al., 2008; Jamtveit et al., 2009, 2011; Ulven et al., 2014).

While reaction-induced fracturing is accepted as a way to maintain fluid access, the mechanical details of the process are poorly understood. As for the mechanism that generates stresses, ‘crystallization pressure’ (also termed ‘force of crystallization’) has been proposed (e.g. Scherer, 2004; Weyl, 1959; Winkler and Singer, 1972). In this model, the precipitation/crystallization of reaction products exert pressure around the growing crystals, and fracturing takes place when that pressure exceeds the local minimum principal stress (Kelemen & Hirth, 2012). Salt crystallization (Scherer, 2004) is a common example where high crystallization forces due to the nucleation of precipitates in pore space cause samples to ‘burst from the inside’ (see Figure 2.1a). However, studies have shown that the crystallization force is low in the olivine carbonation system (e.g. van Noort et al., 2017). Because of the lack of experimental evidence of crystallization forces during olivine alteration, Zhu et al. (2016) proposed an ‘expansion cracking’ mechanism as an alternative model after successfully producing reaction-induced fractures in an in-situ synchrotron X-ray microtomography study. In the ‘expansion cracking’ model, tensile stresses are generated due to the volume mismatch between regions with different precipitation rates, leading to cracks forming in regions that expand slower than their surroundings (see Figure 2.1b).

Beyond fracturing, dissolution has been recognized as an important part of the olivine alteration process (e.g., Velbel, 2009; Velbel and Ranck, 2008; Wilson and Jones, 1983) and proposed as a mechanism to explain the observed complete carbonation of peridotite. In 1978, Grandstaff showed that dissolution could significantly increase the surface area through etch-pitting. Wilson (2004) suggested that the weathering of olivine is controlled by etch-pitting and channel formation due

to preferential dissolution, which assists the migration of fluid and promotes further reaction. Andreani et al. (2009) suggested that permeability may be maintained during peridotite carbonation by the development of preferential flow zones. Lisabeth et al. (2017a, 2017b) observed relevant structures in dunite samples that have been reacted under controlled stress conditions and interpreted them as a pattern of secondary porosity bands formed by dissolution coupled to locally intensified compressional stresses.

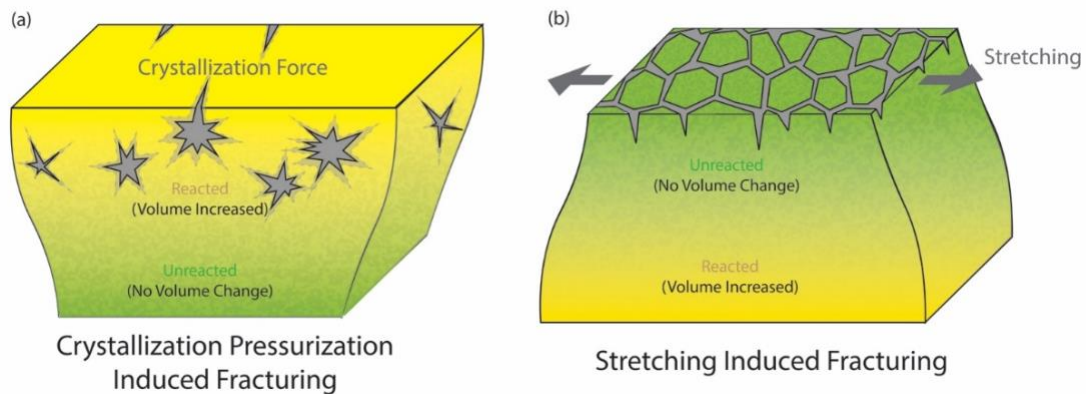


Figure 2.1: Illustration of the mechanisms of reaction-induced fracturing during olivine-fluid interaction. a) The crystallization pressurization model describes the development of fractures caused by crystallization forces exerted on the surroundings due to growth of precipitates. Salt crystallization (Scherer, 2004) is a typical example of the crystallization pressure induced fracturing. The fractures first appear at areas where precipitation is most concentrated and propagate outwards. b) The surface cracking model describes the development of fractures as a result of a contrast in expansion which causes stretching at the surface. A difference in the precipitation rate between the periphery and interior of the sample causes them to expand at different rates with the interior expanding faster than the surface. This builds up the tensile stress at the surface that fractures the sample and leads to a development of a polygonal fracture network. The fractures propagate from the surface inwards.

Previous investigations of olivine carbonation were largely based on the interpretation of naturally deformed samples (e.g., Macdonald and Fyfe, 1985), thermodynamic modeling (e.g., Kelemen and Hirth, 2012) or comparison with reaction systems other than olivine (e.g., leucite to analcime in Jamtveit et al., 2009). While these approaches led to significant advancements, there are limitations to the

understanding of the mechanisms responsible for porosity generation during olivine carbonation that these approaches can provide. The history of natural fault rocks is inevitably complex, and thermodynamic arguments and numerical models can only indicate a potential, while the actual progress of chemical reactions is strongly affected by interfacial structures, which vary considerably in different mineral systems. Thus, it is critical to complement such studies with laboratory experiments on olivine carbonation.

Synchrotron-based X-ray tomography is an advanced non-destructive method to capture three-dimensional images of materials. Where processes affecting these materials are followed through time, a 4-dimensional (3 spatial dimensions + time) dataset is captured. By using X-ray transparent reaction cells (Fusseis et al., 2014), the technique enables the investigation of fluid-rock interaction at controlled and geologically relevant conditions. We examined the carbonation process of olivine on the basis of 4-dimensional images acquired by X-ray microtomographic imaging with synchrotron radiation at the Advanced Photon Source. Zhu et al. (2016) hypothesized that large grains would be preferred sites for precipitation of new crystals, and the contrast in the grain size produced the volume mismatch due to a preferred precipitation on the larger grains and led to the fracturing of the sample. To further test the hypothesis, in the current study, we conducted a new experiment using an olivine aggregate with larger grain size (80-100 μm) compared to the previous experiment reported by Zhu et al. (2016; 0-20 μm). We also performed advanced 3D analyses and quantification of the micro- and nano-tomography data obtained by Zhu et al. (2016). In an advancement of the results presented by Zhu et al. (2016), here we present direct

evidence for the coupled mechanisms of dissolution and precipitation-driven fracturing during olivine carbonation and demonstrate their importance in sustaining the reaction progress at different spatial and temporal scales. We further show direct evidence of how reaction-induced fracturing operates, i.e., how stress is generated through volume-increasing reactions. A better understanding of olivine carbonation directly applies to the geological sequestration of CO₂ (Gislason et al., 2010; Mani et al., 2008). The principle of in-situ carbon mineralization is the conversion of silicate and hydroxide minerals to form carbonate minerals as a stable sink for CO₂ (Power et al., 2013). Peridotite, because of its wide occurrence and high reactivity, is considered one of the best potential feedstocks for CO₂ mineralization (Andreani et al., 2009; Beinlich & Austrheim, 2012); the estimated rate of CO₂ consumption peridotite carbonation could be as high as 2×10^9 tons·km⁻³ per year (Kelemen & Matter, 2008). As the dominant constituent of peridotite, olivine becomes the most important mineral for CO₂ mineralization. Our study provides new insights into carbon sequestration using ultramafic rocks, and our findings on the mechanism of fracture generation during olivine carbonation could provide guidance to industrial applications.

2.2 Experimental Setup

2.2.1 Sample Configuration

In Zhu et al. (2016), the contrast in grain size between the loose grains and the cup wall aggregate is hypothesized as the cause of the non-uniform precipitation which is crucial to the generation of fractures in the experiment. Here, we use coarse-grained

olivine aggregate in the cup wall to reduce the contrast in grain size between the cup wall and the fillings and further test their hypothesis.

The sample assembly consists of a millimeter-sized synthesized San Carlos olivine cup, filled with loose San Carlos olivine sand (grain size 100-500 μm , see Figure 2.2a) and then covered by a lid made of the same material as the cup. Both the olivine cup and its lid are taken from a sintered pellet made from pulverized San Carlos olivine with a grain size of 80-100 μm . This coarse-grained olivine cup is referred to as large grain cup (LGC) in the following discussion. Data obtained from the LGC experiment will be compared to the results of an olivine carbonation experiment conducted by Zhu et al. (2016) at the same experimental conditions, on a fine-grained (grains sizes between 0-20 μm) cup. The fine-grained olivine cup is referred to as small grain olivine cup (SGC) in the following discussion.

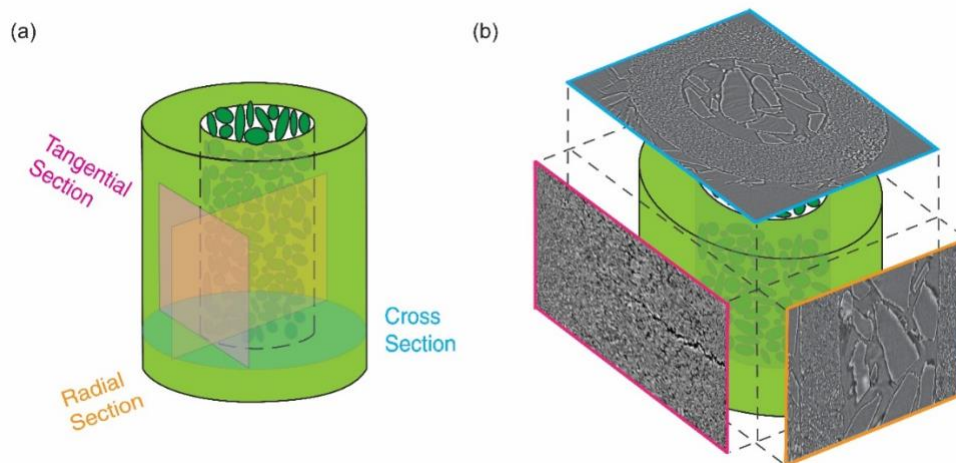


Figure 2.2: Illustration of sample configuration. a) The sample is composed a sintered olivine aggregate cup with loose olivine sand fillings (grain size 100-500 μm). Quantitative microtomographic analyses are conducted on the tangential (pink), radial (orange) and cross (blue) section of the sample. b) Example of the tomographic image that was used in the 2D examination of Zhu et al. (2016).

The cup, which was fabricated by heat-pressing in a procedure described in Zhu et al. (2016), has inner and outer diameters of 1 and 1.8 mm respectively, with a resulting wall thickness of ~0.4 mm. The initial porosity of the cup wall is ~10%. Both LGC and SGC samples were sintered for 4 hours at 1400°C, the LGC sample came out weaker (less cohesive) compared to the SGC sample, and the initial porosity of LGC is slightly higher than that of SGC.

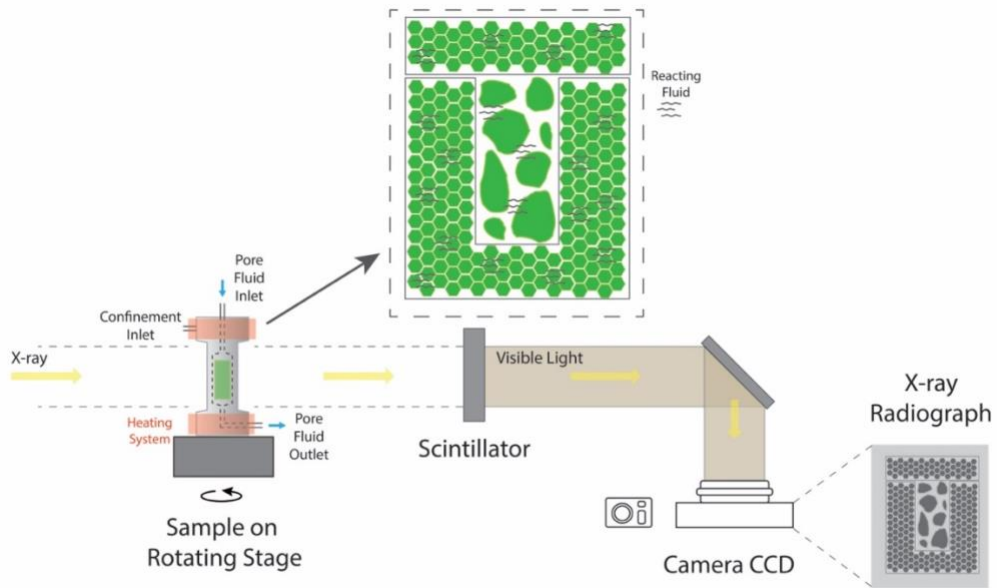


Figure 2.3: Experimental setup for dynamic microtomography. Inside the X-ray transparent pressure cell, the confining pressure, pore fluid pressure and temperature can be controlled independently. The synchrotron radiation imaging records radiographs of the sample at in-situ conditions with ongoing reaction at different angular positions with the sample being rotated.

The loose grains inside the cup allowed the inspection of magnesite growth on free olivine surfaces. The sample assemblies (i.e., olivine cup + loose grains) were jacketed and loaded into an X-ray transparent pressure cell (Figure 2.3). A confining pressure of 13 MPa and a pore fluid of NaHCO₃ aqueous solution (1.5 mol·L⁻¹) at 10 MPa were applied to the sample. The pore fluid pressure downstream is regulated by a pressure regulator while the upstream is controlled by a syringe pump to form a semi-open

system. Both upstream and downstream pore pressures were maintained at 10MPa throughout the experiment. A small axial load is applied independently from the confining pressure by locking the piston at a fixed position. The pressure cell was then heated to 200 °C to initiate the reaction. These conditions were kept constant during the entire microtomography experiment. The reaction of the LGC sample was stopped at 36 hours after considerable secondary porosity generation was observed. No magnesite precipitation was detected in LGC. The SGC sample reacted for 7 days until intense fracturing was observed. Significant magnesite precipitation was detected in SGC (Zhu et al., 2016).

2.2.2 Micro- and Nano-tomography

Third-generation synchrotron facilities produce electromagnetic radiation bright enough to allow rapid imaging even inside experimental vessels, thereby enabling studies of dynamic processes ranging over periods from seconds to days, while acquiring individual 3-dimensional (3-D) data sets in fractions of a second. Synchrotron X-ray microtomography has therefore become one of the most powerful tools in structural geology and rock mechanics studies (see Fusses et al., 2014a for a review and Bedford et al., 2017 for a recent application).

In this experiment, synchrotron-based X-ray absorption microtomography has been used to record the dynamic carbonation of olivine in 4 dimensions. We used an X-ray transparent cell (Fusses et al., 2014), mounted in the upstream experimental station at beamline 2BM of the Advanced Photon Source of the Argonne National Laboratory, 25 m from the source. There, a polychromatic beam filtered by 1 mm aluminum, 15 mm silicon and 8 mm borosilicate glass yielded a photon flux with an energy peak at

65 keV (Zhu et al., 2016). A Cooke pco.edge sCMOS camera with 2560×2160 pixels (pixel size 6.5×6.5 μm^2) was used in a flying scan mode. The sample-detector distance was 300 mm, which introduced a clear phase contrast signal to the data (Cloetens et al., 1996). The camera recorded projections from a 10 μm thick LuAG:Ce single crystal scintillator, magnified through a 10× Mitutoyo long-working distance lens yielding a pixel size of 0.65 μm . Projections were collected with an exposure time of 50 ms while the sample was rotated over 180 ° with 1.2 °·s⁻¹. A total of 1500 projections were collected in 150 s. For the LGC sample, 115 3-D microtomographic data sets were acquired over 36 hours, together forming a 4D data set, with time as the fourth dimension. For the SGC sample, 379 data sets were acquired over 7 days. From these 379 datasets, 19 were chosen for further detailed quantitative analysis. All acquired microtomographic data were reconstructed using the code TomoPy (Gürsoy et al., 2014) into stacks of 2160 images each, with dimensions of 2560×2560 pixels per image. Each of these image stacks contains a 3-dimensional representation of the sample mapped onto a 32-bit image, with the grey values reflecting the local absorption of X-rays (Fusseis et al., 2014a). Where the refractive indices change in the sample, i.e., on edges, this absorption signal is locally overlain by a phase contrast signal (Cloetens et al., 1996). The time series dataset covers the entire duration of the experiment.

After the in-situ acquisition of the microtomography images, a fragment of the cup wall from the SGC was taken to conduct nano-scale imaging. Nanotomography was conducted using a transmission X-ray microscope (TXM) at the beamline 32-ID of the Advanced Photon Source of the Argonne National Laboratory. A monochromatic beam

of X-ray with an energy of 8 keV was used. An X-ray objective lens corresponding to a Fresnel zone plate with 60 nm outermost zone width was used to magnify radiographs onto a detection system assembly comprising a LuAG scintillator, a Zeiss 5X optical microscope objective lens and an Andor Neo sCMOS camera. Nanotomography yields a pixel size of ~60 nm after binning.

2.2.3 Image Processing Procedures

Zhu et al. (2016) conducted preliminary analyses and measurements on 2-dimensional (2-D) image slices (see Figure 2.2b) of SGC through the 3-D microtomography datasets acquired. Here, we present the results of a true 3-D volume quantification of the microstructural changes in the SGC sample (i.e., spatio-temporal changes in grain and pore volumes) and compare them with the results obtained from LGC sample in this study.

In both the SGC and the LGC samples, a sub-region that included both, the cup wall near-surface as well as the interior of the cup wall's was chosen for detailed inspection from all datasets. For each sample, two subvolumes with the dimension of $400 \times 400 \times 400$ voxels were cropped out from the region of interest in the cup wall (see Figure 2.4, subvolume 1 and 2 from SGC and subvolume 3 and 4 from LGC). In the SGC sample, subvolume 2 was further cropped to a volume of $247 \times 400 \times 400$ voxels ($160.55 \times 260 \times 260 \mu\text{m}^3$) to eliminate the boundary of the cup wall.

Image segmentation is the separation and extraction of phases of interests from the 3-D data sets for further analysis and quantification. A large range of segmentation algorithms exists (e.g., Kaestner et al., 2008). In global binary thresholding, images are segmented by identifying the grey value range representing a phase and assigning all

voxels within that range a single value (usually 1) while all other voxels are classified as matrix (and assigned a different single value, usually 0) (Heilbronner & Barrett, 2014). Global binarization was conducted in Avizo Fire 8 to isolate pores from solids.

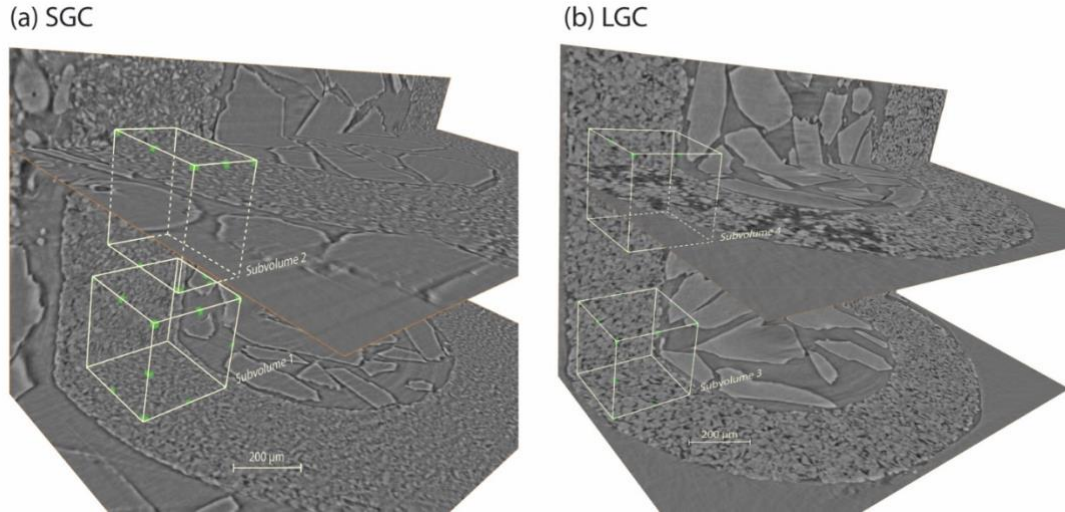


Figure 2.4: Positions of the subvolumes in the cup wall of a) SGC and b) LGC, where quantitative 3D microstructure analyses were performed. In the SGC sample, subvolume 1 (bottom box) is located at the center of the cup wall. Subvolume 2 (top box) is located adjacent to the outer rim of the wall. In the LGC sample, both subvolume 3 (bottom box) and subvolume 4 (top box) are located at the center of the cup wall.

In the SGC sample, at the given spatial resolution, we could not resolve the new crystals that precipitated within the cup wall and only the pore space was segmented there. Pixels with grey values that fall in the range $(-0.00031, -0.000077)$ were assigned to pore space. We used the segmented data to quantify the change in the spatial distribution of pores during the experiment. Each subvolume was further divided into smaller cubes (side lengths $\sim 26 \mu\text{m}$) in which the average porosity is calculated to examine where changes in porosity occurred. In the LGC sample, grey values that fall in the range $(-0.00031, -0.000095)$ were assigned to pore space.

In the nanotomography data, the grey value range (2.97672×10^{-9} , 0.13161) was assigned to pore space. In these data, the olivine is represented by grey values in the range (0.30846, 1.3161). Voxels with intermediate grey values (0.13161, 0.30846) were assigned to reaction precipitates (e.g., magnesite).

2.3 Data Analysis and Results

We have observed the development of secondary porosity during the reaction in both the LGC and SGC experiments (Figure 2.5). Detailed examination has further revealed that the porosity generation in LGC is significantly different from that in SGC.

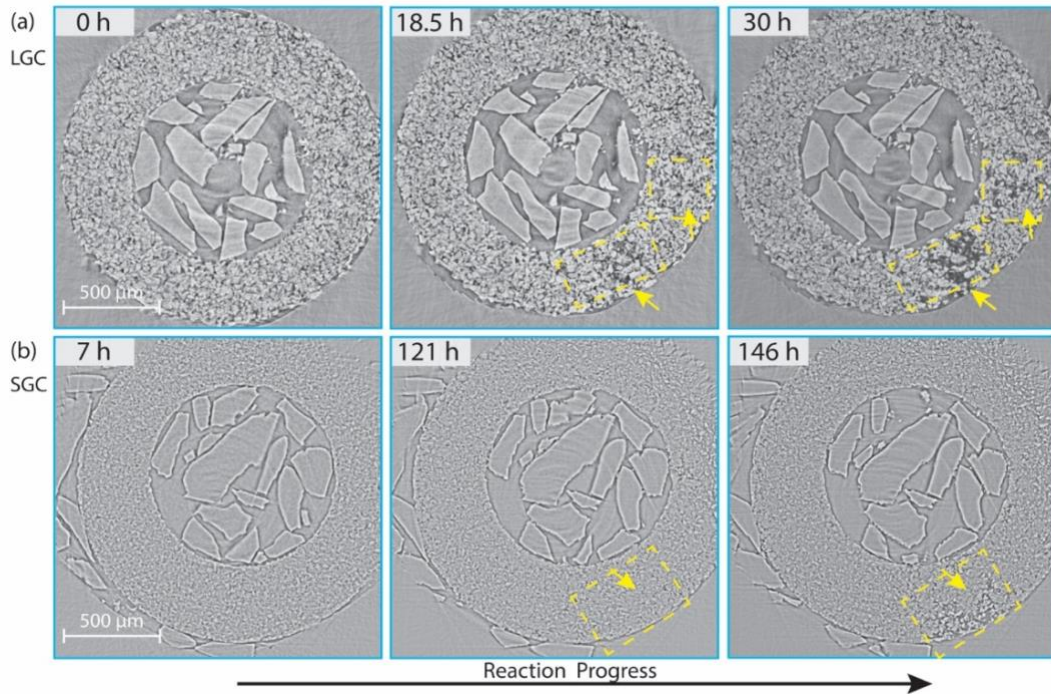


Figure 2.5: Reconstructed images showing the cross-section view of the sample undergoing olivine carbonation. a) In the LGC sample, original olivine grains shrink, and secondary pore space appears (yellow arrows), suggesting dissolution of olivine. Most of the large pore spaces concentrate at the interior of the cup wall (highlighted by yellow dashed lines). b) In the SGC sample, the fractures first developed at the surface of the cup and propagated from the outer rim into the cup wall (highlighted by yellow dash lines). Larger pore space distributes mainly near the rim.

2.3.1 Dissolution in the LGC Sample

As the reaction proceeded, olivine grains in the LGC sample shrank in size and secondary pores were produced (Figure 2.5a). This suggests that dissolution dominated the carbonation reaction in LGC, with little precipitation detected. The secondary pore space formed first at the center of the cup wall and grew outwards (Figure 2.5a), which is opposite to that in SGC where fractures grew from the surface of the cup wall inwards (Figure 2.5b).

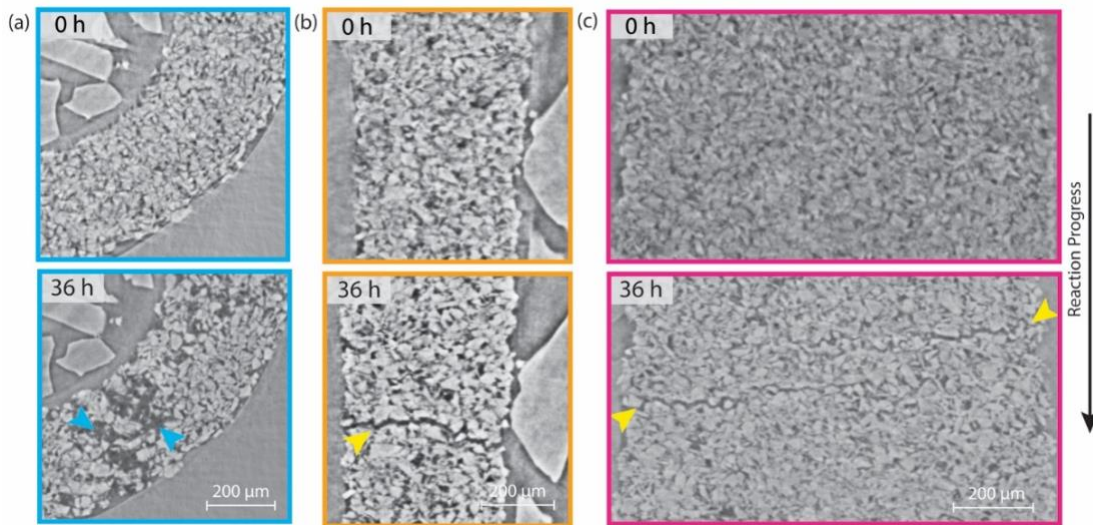


Figure 2.6: a) Dissolution features in the cross-sectional images of the LGC sample. 3D examination reveals that these dissolution features (blue arrowheads) are associated with planar fractures (yellow arrowheads) appeared in b) the radial and c) the tangential section images. The boarder color of each section corresponds to color code given in Figure 2.2.

Planar fractures formed within 36 hours of reaction in LGC (Figure 2.6), and the experiment was stopped shortly after the formation of these fractures. Because of the lack of precipitation, these planar fractures could not be induced by the non-uniform volume expansion as in the SGC sample (Zhu et al., 2016). Under a constant confining pressure, volume reduction in olivine grains (i.e., dissolution) likely shortened the LGC sample length as the reaction proceeded. Because the axial piston was kept at a fixed

position during the experiment, this shortening in sample length resulted a decrease in axial stress. Because the LGC sample is mechanically weak (less cohesion), even though the reduction in axial stress is small, it could be sufficient to cause fracture in LGC in the manner of dilation bands under triaxial extension (e.g., Zhu et al., 1997). Detailed examination of the 3D images revealed the disappearance of small grains along the plane which is clear evidence of dissolution. Thus, we refer to these planar cracks as dissolution-assisted fractures under triaxial extension. The dissolution-assisted fractures were not observed in the SGC sample because it is much stronger due to its fine grain size (e.g., Eberhardt et al., 1999; Singh, 1988). The triaxial extension stress condition would be no longer present once precipitation started (after ~36 hours) and sample volume expansion took place.

2.3.2 Lack of Precipitation in the LGC Sample

Evidence from direct observation and quantitative analysis has shown that the LGC sample has a lack of precipitation.

Within the duration of the reaction, hardly any precipitation was observed in the cup wall. In the microtomographic images, the surface layer of the loose olivine grains remained free of precipitates. Both sides of the cup wall remained straight and showed no spalling due to precipitation-caused non-uniform stretching. The sample did not experience any expansion as seen in the SGC sample.

Apart from the direct observation, grey value histograms of the data also show evidence of lacking precipitation in the LGC sample. The grey value histograms of 4D microtomography data evolve systematically during in-situ experiments, which can be utilized in the evaluation of the reaction progress (Fusseis et al., 2012). Systematic

analysis of the histograms of the grey value distribution revealed the progression of reaction during the experiment (Figure 2.7).

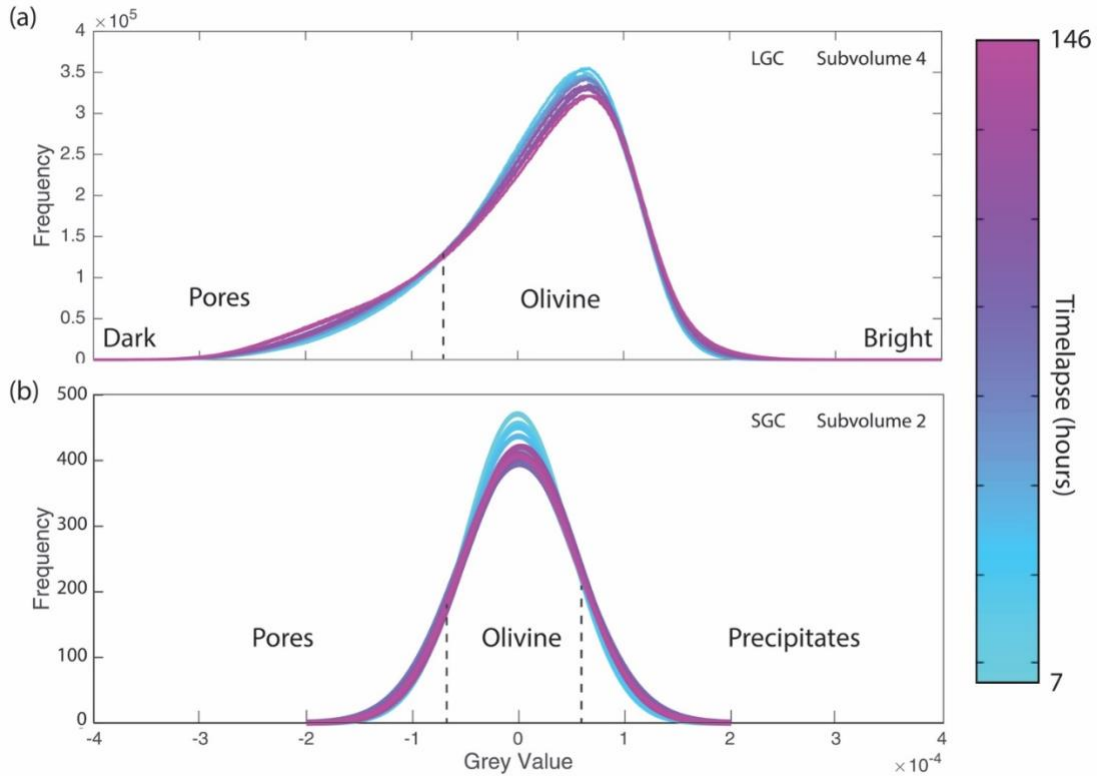


Figure 2.7: Best fits for the grey value distribution histograms of the sample at different stages of the reaction in a) subvolume 4 from LGC sample and b) subvolume 2 from SGC sample. Different colors represent time lapses as shown. Pores, olivine, and precipitates are identified based on their grey value ranges. Higher values correspond to lighter grey (solids). The more negative a value is, the darker the grey color becomes (e.g., pores are black). Histograms of the SGC sample were calculated from a 2D image (Zhu et al., 2016), whereas the histograms of the LGC sample were calculated from 3D datasets.

Comparing the histogram of SGC sample with the LGC sample, the shape of the histograms from the LGC sample (Figure 2.7a) is clearly asymmetric compared to the bell-shaped histograms in the SGC sample (Figure 2.7b). The slope on the precipitation side of the LGC histogram is steep and becomes steeper as the reaction proceeds, indicating dissolution of olivine with little to no precipitation. The slope on the pore

side of the LGC histogram becomes shallower due to the secondary porosity generation due to the dissolution of olivine.

Data from the SGC sample showed that the histograms became uniformly flatter and wider over the duration of the experiment, with an increase in the number of both the darkest and brightest voxels at the expense of the voxels with intermediate grey values. These systematic changes in the absorption behavior can only be caused by the sample reacting and indeed reflect the dissolution of olivine, the generation of pore space and the precipitation of reaction products, in addition to phase contrast around newly generated edges in the sample. The best-fit curves to the histograms evolved systematically during the reaction and intersected in a relatively narrow grey value range (-0.000077, -0.000055) (Figure 2.7). Voxels with grey values darker than -0.000077 correspond to fluid-filled pores, whose volume proportion increases throughout the reaction process.

2.3.3 Porosity Evolution of LGC Compared to SGC

Pore space development in LGC is significantly different from SGC. As shown in Figure 2.5 and 2.6, the secondary pore space in the LGC developed simultaneously at the interior and the near-surface area of the sample. However, in the SGC sample, pore space first occurred in the area close to the surface and propagated inwards.

To further examine the difference in porosity generation of the LGC and SGC samples during the reaction, pore spaces within the subvolumes are segmented from the images and calculated. Figure 2.8 compares the porosity of subvolume 1 and 2 (Zhu et al., 2016) from SGC and subvolumes 3 and 4 from LGC samples. As shown by the figure, initial porosity of the LGC and SGC sample is similar. The rate of porosity

increase in the LGC sample is similar to the SGC during the first 36 hours after the reaction started. Porosity of the LGC sample is increasing throughout the duration of the experiment while porosity of the SGC shows a decrease after 90 hours of reaction. In the LGC sample, the porosity increased ~5% and likely resulted from dissolution. This is consistent with other studies that showed the precipitates do not occur in olivine carbonation within 36 hours of reaction (e.g., Lisabeth et al., 2017a).

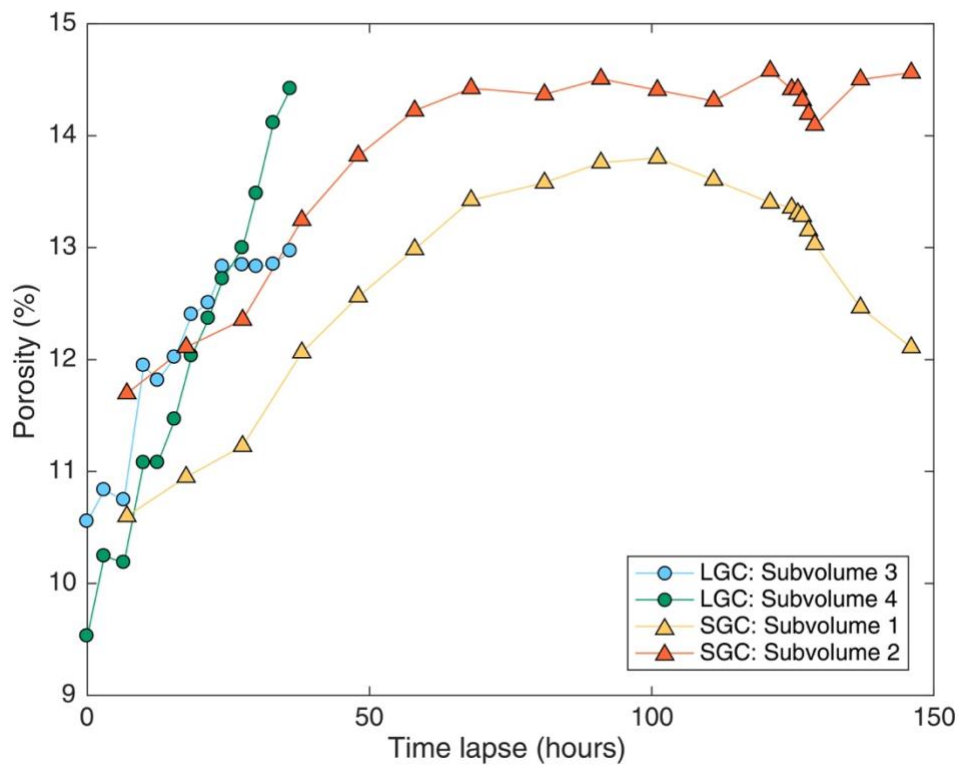


Figure 2.8: Comparison of porosity evolution in LGC (this study) versus SGC reported by Zhu et al. (2016).

We then further evaluated the porosity distribution within the subvolumes by quantifying the porosity of the 2D tangential slice along the samples' radial direction. Figure 2.9 compares the porosity distribution of subvolume 2 from the SGC sample with subvolume 4 from the LGC sample. Subvolume 4 shows a homogeneous increase

in porosity of $\sim 5\%$ throughout the entire subvolume. Subvolume 2, while showing an increase of porosity during the first 30 hours of the reaction, starts to show a porosity decrease in areas close to the center of the cup wall after 81 hours of reaction. Comparison of the subvolumes from SGC and LGC revealed that the porosity generation within the LGC sample is relatively homogeneous while the porosity generation within the SGC sample starts to show contrast between the cup's near-surface area and its interior after 81 hours of reaction. Results from the porosity evaluation further support the finding that the LGC sample is dominated by dissolution with no presence of precipitation.

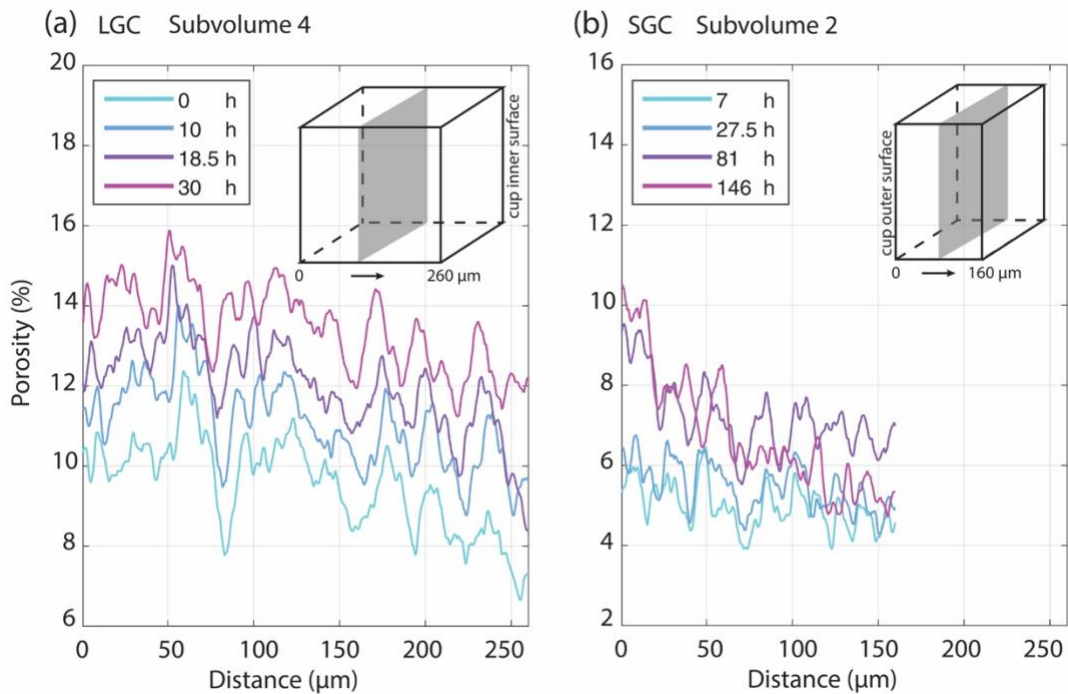


Figure 2.9: Porosity profiles of a) LGC and b) SGC along the radial direction of the sample cup. Different colors indicate reaction time lapse.

2.3.4 Fractures in LGC vs. SGC

As discussed in 2.3.1, the planar fractures observed in the LGC sample are likely a result of the dissolution-assisted extensional crack. This is different from the stretching-induced fractures in SGC (see Zhu et al. 2016) where non-uniform precipitation is indispensable. The dissolution-assisted fracturing in LGC and the stretching-induced fracturing in SGC both generated secondary pore space during the experiments, but the fractures in LGC differ distinctively from those in SGC in many ways:

- Firstly, the dissolution-assisted fracturing is a single, planar feature in 3D with no obvious secondary fractures branching out, while the fractures observed in the SGC sample formed a network of intersecting cracks. Figure 2.10a shows the morphology of the dissolution plane and the fracture network in 3D. It is shown in Figure 2.10b that the fractures intersected with each other and formed a complex wedge shape network with the vertex pointing towards the sample's interior. The dissolution-assisted fracturing mainly developed along a plane and shows less intersection with other features.
- Secondly, the LGC sample dominated by dissolution features shows clear evidence for shrinkage of larger grains and disappearance of smaller grains at the interior of the aggregate (Figure 2.5a). The SGC sample exhibits patches that develop during the reaction which are evidence for the reaction product precipitation (Zhu et al., 2016).
- Thirdly, the development of micron-scale dissolution is simultaneous, with the shrinkage of grains occurring both at the surface and the interior of the cup wall (Figure 2.5 and 2.6a). In contrast, development of the reaction-induced

fracturing is successive with most fractures occurring first at the surface and migrating towards the interior of the cup wall. This caused the observed wedge shape of the fracture network (Figure 2.10b). Development of the fractures also exhibits hierarchical sequence with main fractures appearing first. The secondary fractures branch out from the main fracture and divide the sample into smaller domains (Figure 2 from Zhu et al., 2016).

- In addition, no precipitates were observed along planar dissolution features in the LGC sample, the cup wall remains straight throughout the experiment. But for the SGC, the cup wall shows clear spalling which is a sign of non-uniform expansion that links to precipitation in this experiment.

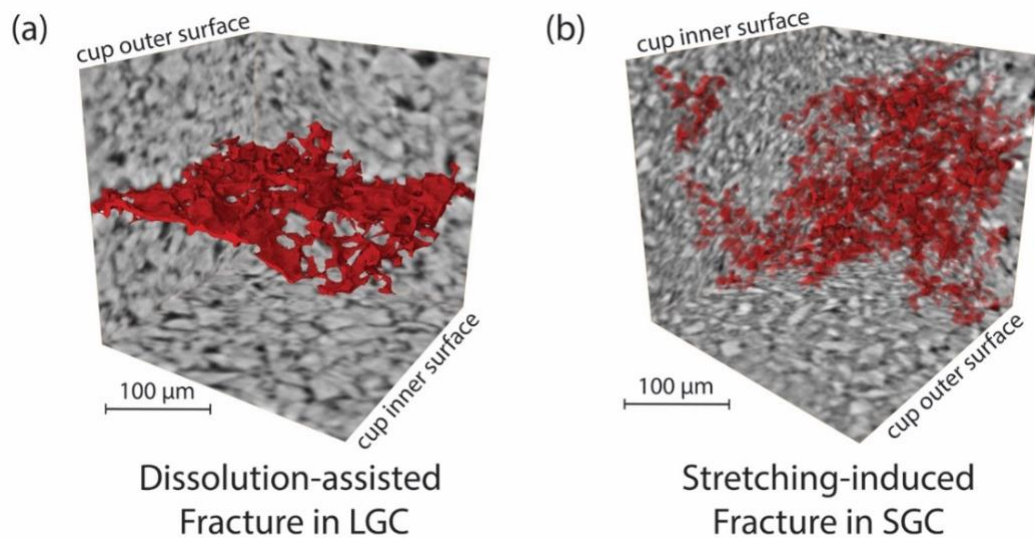


Figure 2.10: The 3D geometry (in red) of a) dissolution-assisted fracture in LGC is distinctively different from b) the stretching-induced fractures in SGC. Both displayed volumes are $260 \times 260 \times 260 \mu\text{m}^3$ in size.

2.3.5 Dissolution and Fracturing of Individual Olivine Grain

The reaction affected not only the aggregate but also the individual olivine grains. Both the dissolution and fracturing are observed at grain scale in the SGC sample. Figure 2.11 shows a series of image slices through a nanotomography dataset, moving through an olivine grain in the cup wall. The grains clearly exhibit channels (etch pits) in the reaction zone. In video S1 (see Xing et al., 2018) it can be seen that these channels penetrate into, and even through olivine grains. As we do not observe any precipitation filling or clogging the tubes, it is therefore reasonable to think that the channels start as etch-pits and grow deeper with the advancing of dissolution and eventually become the through-going channels observed here. The tubular shape and the depth of penetration indicate that they are ‘worm hole’ features, likely resulting from dissolution. The shape and the width of these channels vary, with wider inner channel diameters below the surface suggesting more extensive dissolution at depth. On average, most typical tubes have an inner diameter of around 720 nm.

The fracturing is also observed on individual grains at nanometer scale. Figure 2.12 shows nanotomographic evidence for hierarchical fracturing within olivine grains. The secondary fractures developed from the primary fracture and formed in a direction that is perpendicular to the earlier ones.

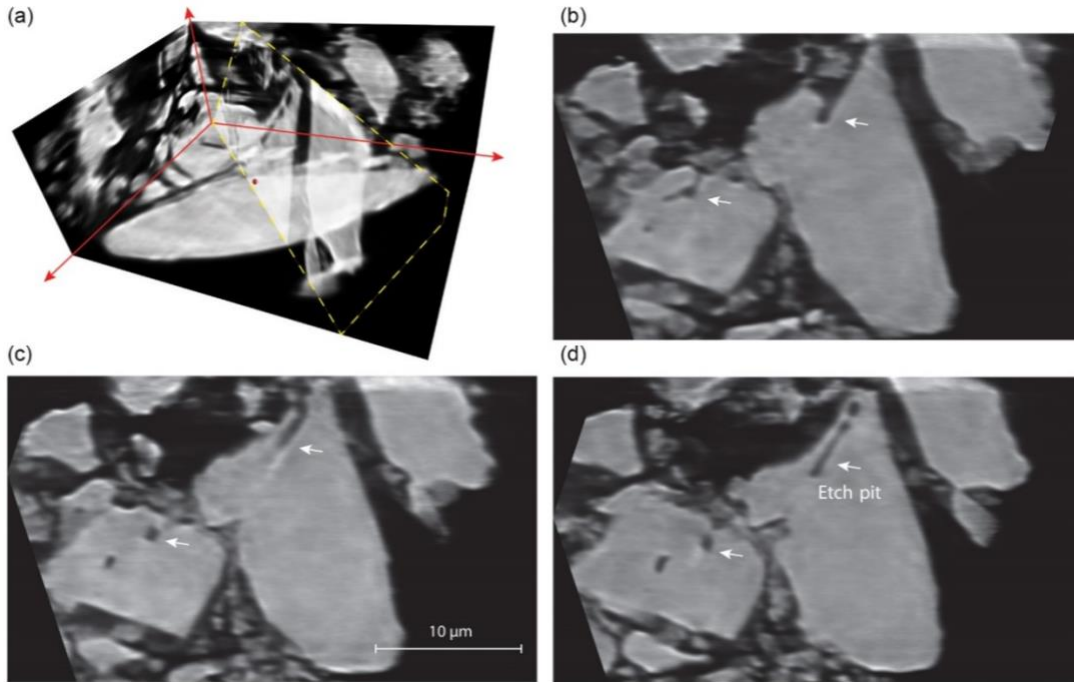


Figure 2.11: Reconstructed images from the nanotomography data of the SGC sample's cup wall demonstrate the existence of etch-pits and dissolution channels (white arrows) formed in the olivine grain. The precipitates (darker grey) partially fill the pore space (black) between olivine grains (lighter grey). The yellow dashed line (a) marks the orientation of the cross-sections (b-d). The vertical distance between each 2D cross-section is ~ 600 nm. Reacting fluid causes a preferential dissolution of the grain which develops small channels that dig into the grain. These features provide a fluid path and eventually break grains, exposing new reactive surfaces.

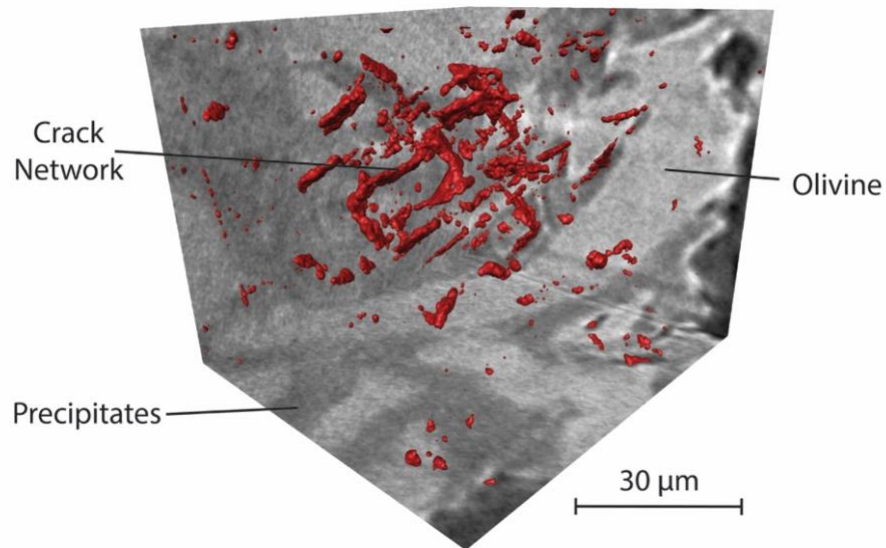


Figure 2.12: Network of microcracks (red) in the reaction olivine cup wall from SGC shows a polygonal pattern. The dissolution channels make the grain (light grey) more susceptible and a stress concentration is also likely to occur around the etch pits.

In the reconstructed microtomographic images of the loose grains from the SGC, we observed the precipitation of secondary minerals on the surface of the olivine grains inside the cup (Figure 2.13). On the basis of their rhombohedral shapes, we identified these as magnesite crystals. However, the phase contrast between the precipitates and olivine grains is very small, and at the current spatial resolution of ~2 micron, we could not segment precipitates from olivine grain with acceptable uncertainties. Other minerals (serpentine, brucite, etc.; see reaction R2.1~R2.4) were likely also present in the sample but could not be isolated at the given image resolution. Measurement of the magnesite circumference revealed continuous growth during the experiment (see Figure 5 in Zhu et al., 2016). The first magnesite crystals emerged after 48 hours, and grains kept nucleating and growing after that. Growth continued until the experiment was aborted and no deceleration could be observed at any point, which indicates that the sample continued reacting. We determined a growth rate for the grain perimeter of $0.772 \mu\text{m}\cdot\text{hour}^{-1}$, which, by assuming cubic shape of the crystal, yields an equivalent growth rate of $7.18\times 10^{-3} \mu\text{m}^3\cdot\text{hour}^{-1}$. We used a density of $3.01 \text{ g}\cdot\text{cm}^{-3}$ and molar weight of $84.314 \text{ g}\cdot\text{mol}^{-1}$ for magnesite (MgCO_3) in our calculation. Assuming a specific reaction surface of $50\times 50 \mu\text{m}^2$, this gave a magnesite growth rate of $2.85\times 10^{-15} \text{ mol}\cdot\text{cm}^{-2}\cdot\text{s}^{-1}$. This is in general in agreement with the calculation of Saldi et al. (2009).

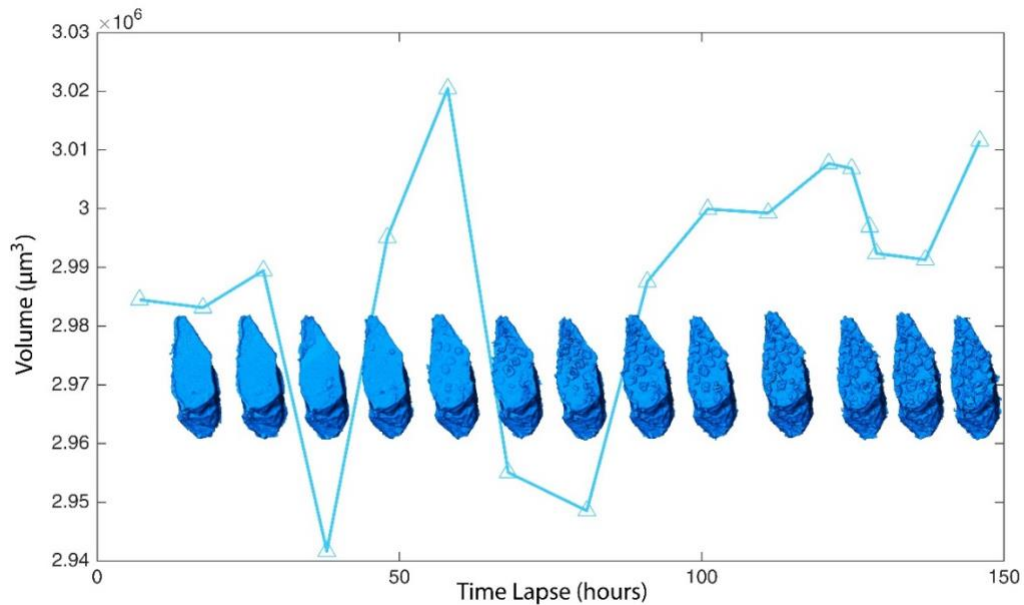


Figure 2.13: Volume change of an individual olivine grain (total volume of olivine and precipitates) during carbonation reaction in the SGC experiment. The precipitates are idiomorphic and referred to as magnesites (see Zhu et al., 2016). This observed volume change results from a combination of the dissolution of olivine and precipitation of magnesites. Fluctuations of the grain volume manifest the altering dominance of dissolution versus precipitation.

The volume change of a loose olivine grain inside the cup was calculated to quantify the competing effect of dissolution and precipitation during olivine carbonation. Individual grains were labeled from the segmented data and their volumes determined. Figure 2.13 plots the volume change of a single grain selected from the loose grains inside the SGC over 13 successive microtomographic datasets (covering 146 hours). Magnesite overgrowth causes a significant roughening of the olivine grain surface. While the volume of the individual magnesite grain steadily increased throughout the reaction (Zhu et al., 2016), the total volume of the grain (olivine plus precipitates) fluctuates from time to time, which reflects variable rates both in the precipitation of magnesite as well as in the dissolution of olivine. A large drop in grain volume occurred at around 38 hours, which is consistent with a period of vigorous olivine dissolution.

The largest continuous grain volume increase took place between 40 and 70 hours, caused by the precipitation of magnesites. At ~70 hours, the grain volume again decreased considerably, indicating that dissolution became dominant once more. This second dissolution episode coincides with the appearance of reaction-induced fractures in the aggregate wall at ~68 hours, suggesting a positive feedback process.

2.4 Discussion

We claim that our experimental observations indicate the activity of two different mechanisms that both create fluid pathways effectively. These are dissolution-dominated fluid pathway generation at micrometer scale in the case of the LGC experiment and at nanometer scale in the case of SGC, and reaction-induced fracturing in the case of the SGC. We detail our interpretation in the following sections.

2.4.1 Dissolution and Etch-pitting

Dissolution and etch-pitting are important mechanisms that affect the grains' surface morphology and the permeability of the sample (e.g., King et al., 2010; Røyne and Jamtveit, 2015). The nanotomographic observation, that etch-pitting incurs extensive dissolution beneath grain surfaces, was also documented by Lisabeth et al. (2017a, 2017b) during the carbonation of dunites. Peuble et al. (2018) also observed nanometer scale veinlets forming oblique to subvertical channels in partially carbonated olivine grains during percolation experiment. The hollowing out of olivines seems especially important in areas where the grain boundary porosity is decreasing due to the precipitation of secondary minerals. There, subsurface dissolution channels in olivine grains preserve important fluid pathways and maintain the reaction. This

supports the hypothesis of Andreani et al. (2009) that the permeability can be maintained by the preferential dissolution even in the cases where the overall porosity is decreasing. Apart from providing access for fluids, subsurface dissolution features also make the grain more susceptible to fracturing and thereby promote the generation of fracturing observed in the experiment.

The permeability of these dissolution channels was calculated using Hagen–Poiseuille’s law (Poiseuille, 1844) and Darcy’s law (Darcy, 1856). Hagen–Poiseuille’s law allows the calculation of the fluid flow inside a tube in dependency of the pressure gradient:

$$Q = \frac{-\pi r^4 \Delta P}{8\eta \Delta L} \quad (2.1)$$

where Q is the volume flow/rate of discharge, r is the radius of the tube, η is the viscosity of the fluid, and ΔP is the pressure difference over the flow length ΔL . Darcy’s law stated that the rate of discharge is proportional to the viscosity of the fluid and the pressure drop over a given distance, i.e., for a tube with a radius in r :

$$Q = \frac{-k\pi r^2 \Delta P}{\eta \Delta L} \quad (2.2)$$

where k is the permeability of the tube. Combining the two equations, k can then be derived as:

$$k = \frac{r^2}{8} \quad (2.3)$$

In this experiment, r is ~ 6 pixels (360 nm). This yields a permeability of $\sim 1.6 \times 10^{-14} \text{ m}^2$, which is high enough to transmit reacting fluids through these channels.

Considering the density of ‘worm hole’ features over the grain, the permeability contributed by the channels could be reduced by two orders of magnitude but is still able to transmit fluid.

These intragranular channels contrast the transgranular fractures. But the development of these etch-pitting dissolution channels also provides a fluid path for the reaction and allows a more extensive degree of alteration of the grain. They weaken the grains, make them more susceptible to disintegration and provide nucleation sites of the later fracturing. While sparse in our data, we think that over geological timescales the contribution by dissolution channels to bulk permeability and the advance of the reaction would be significant. However, on the timescale of our experiments, these features alone are insufficient to explain the observed self-sustainability of the reaction considering the scale and density of the dissolution channels, and we argue that the main contribution must come from volume mismatch cracking in our laboratory study.

2.4.2 Reaction-induced Fracturing

Olivine carbonation could produce up to a 44% increase in solid molar volume assuming the reaction can proceed to completion. If such a volume increase takes place, the crystallization pressure generated could be high enough to fracture the host rock (Kelemen et al., 2013; Kelemen & Hirth, 2012). However, experimental studies on olivine carbonation show no evidence of high crystallization forces (van Noort et al., 2017) but rather suggest that precipitation causes the pore space to fill up and halt the reaction before the crystallization-induced pressure reaches the critical value needed to generate fracture (Hövelmann et al., 2012; van Noort et al., 2017). Our quantitative estimates indicate that in these experiments, the maximum volume expansion is ~5%.

This is not enough to break the host rock, as shown in salt crystallization experiments (Scherer, 2004). Indeed, the nanotomography data show only dissolution features such as etch pits and worm holes, with no evidence of cracks in olivine grains surrounded by precipitates (Figure 2.11). The lack of evidence for crystallization pressure-induced cracking is consistent with other experimental studies (e.g. Hövelmann et al., 2012).

Based on a microtomography experiment, Zhu et al. (2016) proposed an alternative fracturing mechanism during olivine carbonation where crystallization pressure is not high enough to directly break the host rock. In their experiment, the observed fracture patterns in SGC are analogous to desiccation cracks (e.g., Edelman, 1973; Plummer and Gostin, 1981). In the Zhu et al., (2016) model, the loose olivine grains inside the cup act as precipitate traps that keep the surface of the cup wall relatively free of precipitation. In the interior of the cup wall though, away from the precipitate traps, the crystallization pressure builds up and causes expansion. While the crystallization pressure is too low to cause shear fracturing of the cup, the expanding cup wall interior stretches the surface of the cup wall and causes it to fail in tension and tear. This is facilitated by the near-constant surface area (which decreases slightly as a result of dissolution). In analogy with desiccation cracks, the resulting fractures form characteristic and systematic polygonal patterns: The first set of fractures intersects at right angles, and all subsequent fractures divide the sample into smaller polygonal domains with increasing intersection angles. Since the fracture pattern develops successively rather than simultaneously, the higher-order fractures form in a different stress geometry and as a result migrate perpendicular to the surfaces generated by the previous fracturing event.

To evaluate the potential of surface stretching as a fracture generating mechanism, we estimated the stress that could be produced by the volume-mismatch in the cup wall of SGC. We did so by identifying and tracking grains whose spatial coordinates (x, y, z) changed continually as the sample expanded. Distances between these grains were measured at different times. Our measurements indicate an average expansion of $\sim 9.1 \mu\text{m}$ over a distance of $\sim 260 \mu\text{m}$ from 7 hours to 125.9 hours after the start of the experiment. The results revealed an axial elongation of 2.78~4.71% in ~ 120 hours in the LGC sample. However, little to no expansion was observed at the near-surface area of the sample's cup wall. This would translate into an axial strain of ~ 0.03 of the outer layer in order to compensate the volume mismatch. The elastic moduli and strengths of the synthesized porous olivine aggregates are similar to weak sandstones. Using Young's modulus of $\sim 10 \text{ GPa}$ yields extensional stresses generated due to the expansion of $\sim 300 \text{ MPa}$, easily exceeding the tensile strength of the sample ($\sim 10 \text{ MPa}$). Interestingly, our estimate of extensional stress generated by the volume mismatch is of the same magnitude to the stress from crystallization pressurization (e.g. Kelemen et al., 2013). For natural peridotite, Young's moduli range from 108 to 194 GPa (Christensen, 1966), tensile strength is 50 to 290 MPa, and spall strength is $\sim 58 \text{ MPa}$ (He et al., 1996). An equivalent volume expansion of $\sim 10\%$ in nature could lead to a stress of 3.24 GPa. In both cases, the stress is more than sufficient to fracture the material. However, these are simple estimations of stress and strain made with basic assumptions and local conditions. Considering the extent of the local carbonation reaction and how the expansion in the center is affecting straining of the outer layers,

the estimated stress can be considerably lower but should still be in a range that is sufficient to break the material.

To generate the expansion cracks via surface stretching, the volume mismatch must be substantial, which requires keeping the near-surface region free of precipitates. Zhu et al. (2016) suggested that the loose olivine grains inside the sample cup worked as precipitate traps/attractors in this experiment. Because the rate of crystal growth decreases drastically as the curvature of the substrate increases (García et al., 2013; Ziese et al., 2013), large grains in general are preferred sites for precipitation of new crystals. With a size contrast of ~2 orders of magnitude, the loose olivine grains (100-500 μm) in the immediate vicinity of the inner cup surface fulfilled the function of precipitate traps and thereby kept precipitation level at the surface of the olivine cup wall low.

We tested the idea of volume mismatch cracking by conducting the LGC experiment. Now the size contrast between the grains forming the aggregate in the cup wall and the loose grains inside the cup was significantly reduced, and we expected less efficient precipitate trapping, and consequently little to no reaction-induced cracks. The experimental results support this idea. The only planar features observed in the new microtomography experiment are planar dissolution-assisted cracking (Figure 2.6 and 2.10a).

A detailed examination of the dissolution channel shown in Fig. 2.6 revealed no evidence of precipitates there. This places doubt on the crystallization pressure being responsible for fracturing during olivine carbonation. If not, what could be an

alternative explanation for the observed fracturing? To further address this question, we examined the porosity evolution and distribution in the 3-D tomographic datasets.

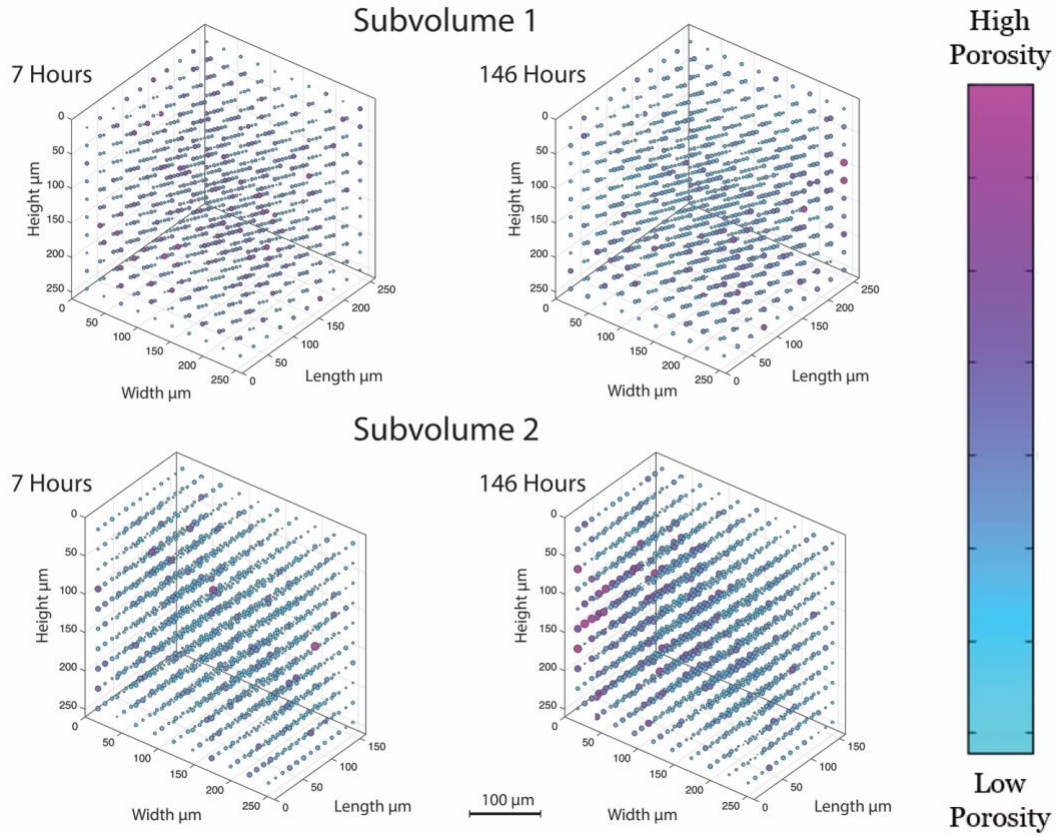


Figure 2.14: Pore distribution within the subvolumes from SGC sample. For subvolume 1 which contains a more interior of the sample, porosity is relatively homogenous among the volume. For subvolume 2, as it contains a more outer part of the sample, a concentration of high porosity can be found in the outer edge compared to the inner edge of the subvolume. This contrast in porosity also reflects a non-uniform precipitation which generates stress that fractures the rock.

Despite the histogram analysis revealing a bulk increase in the porosity of the cup wall during the experiment, the distribution of these newly generated pores was inhomogeneous in the sample (Figure 2.9 and 2.14). This perturbed the initially homogeneous porosity distribution. This effect became particularly apparent in subvolume 2, which started to exhibit higher porosity where it was closest to the outer surface of the sample after 68 hours (see Videos S2, S3, S4 from Xing et al., 2018 for

details). The difference in porosity distribution within the sample became more pronounced as the reaction proceeded, with porosity in the outer surface of the cup wall increasing while the porosity inside the cup decreased. In our interpretation, this change in the pore volume reflects a contrast in the precipitation rate where precipitation proceeded more slowly in the outer part compared to the inner part of the sample wall, leading to different rates of expansion and the generation of tensile stresses.

The ‘expansion cracks via stretching’ mechanism can explain the observed microstructure evolution in two subvolumes of SGC (Figure 2.4). Since subvolume 2 is located at the periphery of the cup, it would be fractured before subvolume 1, which is located in the center of the cup wall. This prediction from the ‘expansion cracks via stretching’ mechanism is consistent with the observed distribution of pore space that most porous area is located close to the periphery. This mechanism also explains why the fractures tend to develop perpendicular to the reaction surfaces. Similar models relating the reaction generated stress and fractures have also been used to explain other exfoliation cracks (e.g. Blackwelder, 1925).

In summary, two fundamental observations from our experiments are inconsistent with the “crystallization pressure induced fracturing” model and form strong arguments against high crystallization forces (i.e., sufficient to break the surrounding rock) (Figure 2.11, 2.14). Firstly, if the cracks were generated directly by crystallization pressure, we should expect them to initiate in a region with intense precipitation and porosity reduction. However, in the outer layer of our sample where the fractures are observed, no precipitates formed prior to the fracturing. Secondly, on the nanoscale, the channels formed by dissolution show hollow and smooth inner surfaces and no precipitation of

magnesite (or any other minerals) which shows evidence of low crystallization pressure.

Our detailed analyses provide quantitative support to the “surface cracking via volume mismatch” model first proposed by Zhu et al. (2016). Previous experimental studies on olivine carbonation show that the crystallization force is low (van Noort et al., 2017), suggesting that breaking host rocks by crystallization pressure as in salt crystallization is unlikely which is in contrast to fracture networks that are commonly observed in naturally occurred serpentinized and carbonated peridotites (Iyer et al., 2008; Macdonald & Fyfe, 1985). We present a resolution to this conundrum by documenting a process that allows fracturing without a high crystallization force.

2.4.3 Coupled Mechanisms of Dissolution and Precipitation-driven Fracturing

The findings of this study can be summarized in a mechanism that couples dissolution and precipitation during olivine carbonation. If dissolution and precipitation are heterogeneously distributed in a rock, non-uniform volume expansion can cause breaking of the host rock via surface stretching. In nature, heterogeneity in the porosity and permeability of a rock formation is common, which may cause non-uniform concentration of reaction and distribution of precipitation (Wells et al., 2017). As shown in our study, the resulting volume mismatch could lead to expansion fractures. The fractures provide new fluid pathways and expose fresh reactive surfaces to sustain the carbonation. In the long term, fluid pathways may be provided by “worm-hole” etch pitting. Dissolution channels could deteriorate rock strength over longer timescales (Figure 2.15).

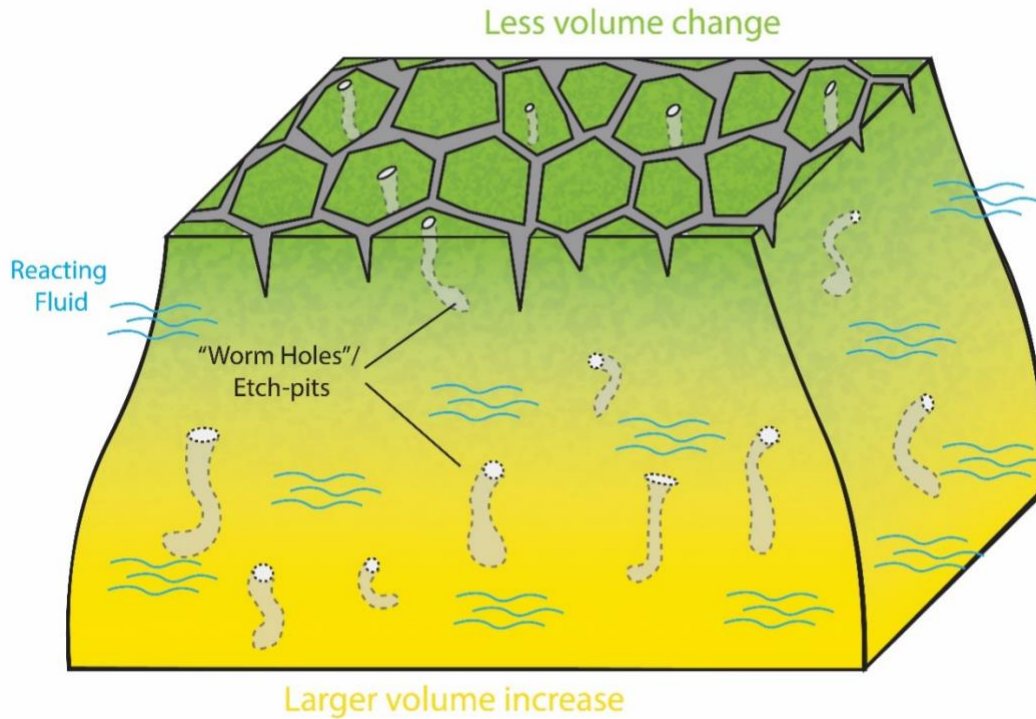


Figure 2.15: Illustration of porosity generation mechanisms during the olivine carbonation reactions. A combined mechanism of surface cracking and the dissolution channelization plays an important role in the porosity generation. Heterogeneity in the micro-structure of the material would cause non-uniform distribution of precipitation. This would lead to the generation of surface cracking via volume mismatch and generate secondary porosity. Dissolution also produces pore spaces and fluid pathways through etch-pitting channelization which makes the grains susceptible to the cracking on a longer timescale.

In a field study on serpentinization of peridotites at ocean ridges, Rouméjon and Cannat (2014) show that the reaction-induced fracturing occurs in the early stages of serpentinization (probably before 20% of serpentinization) while the rest of the volume increase is accommodated by the serpentine itself and dissolution processes dominate until completion of the reaction. Clearly, natural processes are more complex. Laboratory studies are not capable of simulating nature settings due to the vastly different length and timescale. Instead, we focus on understanding the underlying mechanism of porosity generation during olivine carbonation reaction. Using the coupled dissolution and fracturing model described above, we postulate that at the

beginning of a carbonation reaction, dissolution plays an important role in maintaining porosity. As reaction progresses, non-uniform expansion of the rock due to precipitation could lead to fractures. Once the host rock is fractured, accelerated reaction takes place to achieve 100% carbonation.

In general, several different mechanisms seem to facilitate olivine carbonation and contribute to sustaining it. On relatively short timescales, rapid reaction-induced tensile fracturing could be the dominating mechanism that maintains the reaction, whereas on a longer timescale, dissolution and the formation of channel-like structures may dominate.

2.5 Conclusions

Using synchrotron-based micro- and nano-tomography, we documented and quantified the reaction progress during olivine-fluid interaction on the micron scale. This allowed us to identify mechanisms that sustain the reaction despite its large positive volume change.

In summary, our experiment results suggest the following:

- The reaction-induced fracturing observed in our experiments results from non-uniform volume expansion. Tensile stresses arise from heterogeneous precipitation and the resulting contrast in the expansion between a faster-expanding interior and a slower expansion near the surface.
- Even though the dissolution cannot be used alone to explain the sustainability of the experimental timescale olivine carbonation, it provides evidence that dissolution etch-pits can provide fluid path and fresh reaction surface for the reaction to proceed. This helps in explaining the naturally occurring complete

alteration of peridotite, as the timescale for natural carbonation ranges from thousands to million years. Even if the dissolution channelizing would only allow slow fluid flow, it could still induce significant alteration given time.

- The coupled mechanism of dissolution and reaction-induced fracturing accounts for maintaining the reaction processes during olivine carbonation. It explains on different time and space scales the formation of observed natural outcrops of completely carbonated peridotite.
- The results from our experimental study also provide new insights into the application of CO₂ mineral sequestration.

Chapter 3: Stabilizing Effect of High Pore Fluid Pressure on Slip Behaviors of Gouge-bearing Faults

Abstract

We conducted experiments to investigate the influence of pore fluid pressure on the frictional strength and slip behavior of gouge bearing faults. Saw-cut porous sandstone samples with a layer of gouge powders placed between the pre-cut surfaces were deformed in the conventional tri-axial loading configuration. A series of velocity-step tests were performed to measure the response of the friction coefficient to variations in sliding velocity. Pore volume changes were monitored during shearing of the gouge. Our results demonstrate that, under constant effective pressure, increasing pore fluid pressure stabilizes the frictional slip of faults with all four gouge materials including antigorite, olivine, quartz and chrysotile. The stabilizing effect is the strongest in antigorite gouge, which shows an evolution of friction parameters from velocity-weakening towards velocity-strengthening behavior with increasing pore pressure. Experiments with controlled pore volume show that the pore volume reduction diminishes under high pore fluid pressures, implying an increasing dilation component at these conditions. Based on these observations, we propose that dilatant hardening is responsible for the observed strengthening. These results provide a possible explanation to the observed spatial correlation between slow slip events and high pore fluid pressure in many subduction zones.

3.1. Introduction

Geophysical observations reveal a variety of slip behaviors along the subduction interface, including the seismogenic slip, slow slip and aseismic creep. Compared to regular earthquakes, slow slip events exhibit slower slip rates, smaller stress drops, and generally lack high frequency components (Peng & Gomberg, 2010). Slow slip events are observed at both the up- and down-dip limits of subduction seismogenic zones, often in regions where elevated pore fluid pressures are inferred (Figure 3.1). For instance, the down-dip limit at the Nankai Trough where tremor and slow slip events are observed (e.g. Obara, 2002; Shelly et al., 2006) exhibits evidence of near-lithostatic pore fluid pressure (e.g., Kodaira et al., 2004; Peacock et al., 2011; Shelly et al., 2006). Heise et al. (2013, 2017) also show that reduced fluid content is associated with seismicity while fluid overpressure correlates with aseismic creep. These observations together suggest that high pore fluid pressures may promote slow slip behaviors.

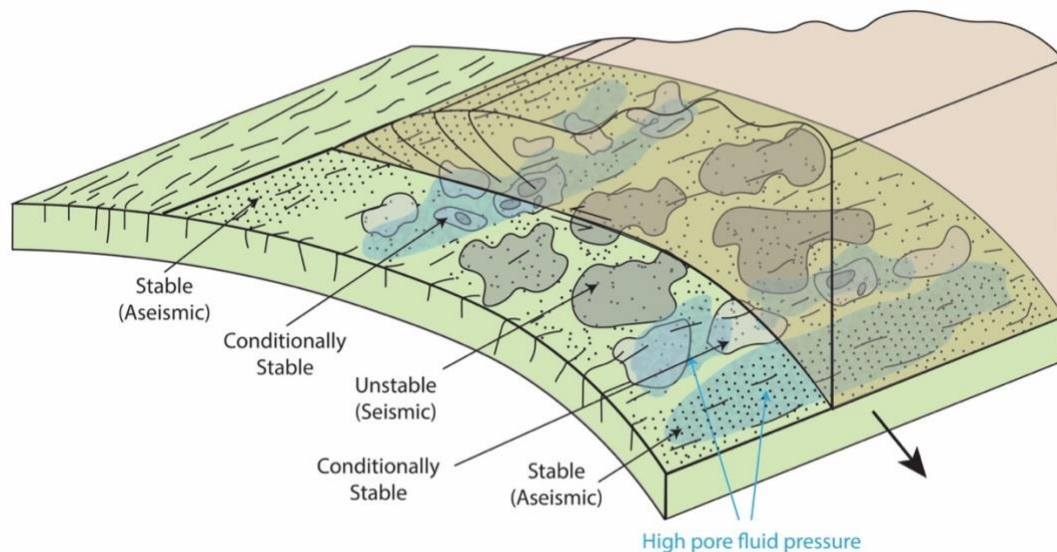


Figure 3.1: Illustration of the slip events distribution within the subduction zone. A variety of slip behaviors can be found along the subduction interface. High pore fluid pressures may play a role in the occurrence of transitional slip behaviors (modified from Bilek & Lay, 2002).

For a fault with a normal stress σ_n and a pore fluid pressure P_f , the effects of pore fluid pressure on fault slip are usually quantified under the law of effective stress ($\sigma_n - P_f$) (e.g. Terzaghi, 1943). Fault slip occurs when the shear stress along the fault, τ , reaches a critical value, $\tau_c = \mu (\sigma_n - P_f)$, where μ ($0.6 \leq \mu \leq 0.85$ for most rocks) is the coefficient of sliding friction (Byerlee, 1978). An increase in pore fluid pressure reduces the effective normal stress and causes the fault to slip at a lower shear stress. This stress threshold model of fault slip, however, does not predict whether the slip induced by high pore fluid pressure is seismogenic or aseismic.

Using the rate-and-state models derived from laboratory experiments on frictional sliding, slip instability can be appraised by the difference between two empirical frictional parameters a and b , representing the rate and state dependence of the frictional strength (e.g. Dieterich, 1979a; Ruina, 1983). A negative velocity dependence factor ($a-b$) indicates decreasing frictional resistance with increasing sliding velocity. Such a velocity weakening system has the potential for dynamic runaway (Gu et al., 1984). A positive ($a-b$) corresponds to velocity strengthening conditions in which frictional resistance increases with sliding velocity, resulting in stable sliding. Slow slip events may arise from faults that are nearly velocity neutral, i.e., at $(a-b) \sim 0$ (e.g. Rubin, 2008) or when the effective pressure is low (e.g. Leeman et al., 2016). The stability of frictional sliding can be described by the critical stiffness k_c (Rice & Ruina, 1983):

$$k_c = \frac{-(a-b)\sigma_n}{D_c} \quad (3.1)$$

In case where $(a-b) < 0$, the slip can accelerate to instability when the critical stiffness k_c is lower than the system stiffness k (Gu et al., 1984; Rice & Ruina, 1983).

The slip stability can be affected by a third frictional parameter, D_c , the characteristic slip weakening distance. Larger D_c favors stable slip.

The rate and state frictional parameters of a rock can be affected by a variety of factors, such as the mineral composition (e.g. Moore & Lockner, 2011), porosity (Blanpied et al., 1995; Takahashi et al., 2011), strain rates (Goldsby & Tullis, 2002; Niemeijer et al., 2010; Rabinowicz, 1958), temperature (Chernak & Hirth, 2010; Chester, 1994; Chester & Higgs, 1992; Lockner et al., 1986) and pressure conditions including both effective pressure and interstitial pore fluid pressure (e.g. Carpenter et al., 2016; Morrow et al., 1992; Sawai et al., 2016). Among these factors, the interstitial fluid pressure has been observed to exert important controls on fault slip behaviors (e.g. Rutter & Hackston, 2017; Sawai et al., 2016).

French et al. (2016) investigated the controls of pore fluid pressurization and pressurization rates on the slip style of experimental faults in saw-cut samples. They show that increasing pore fluid pressure alone is insufficient to induce accelerated slip events unless the confining mechanical stresses decrease. Ikari et al. (2009) show that excess pore fluid pressure developed during the shear of fault gouge hinders gouge consolidation and cementation, and consequently inhibits seismic nucleation. Other experimental studies, however, suggest that high fluid pressure reduces the velocity-dependence factor and favors rupture nucleation (Niemeijer & Collettini, 2013). Change in pore fluid pressure also reduces effective pressure. Sawai et al. (2016) demonstrate that decrease in effective pressure causes a transition from stable to unstable slip behavior in blueschist samples. Scuderi et al. (2017) also show that fluid pressurization could overcome strengthening friction and cause fault instability. The

apparent disagreements in whether high pore fluid pressure enhances or impedes unstable slip could be due to the different rock materials tested. It is important to note that in these experimental studies, the change in slip behaviors were discussed in the context of variations in the effective pressure (as a consequence of varying pore pressure) in addition to pore fluid pressure variations.

French & Zhu (2017) studied the rupture, localization, and slip of faults in serpentinite rocks under varying pore fluid pressure conditions. They showed that at the same effective pressure, high pore fluid pressure reduced the rate of fault propagation in intact serpentinite and caused a transition in brittle faulting from dynamic to quasi-stable (French & Zhu, 2017). Ougier-Simonin & Zhu (2013, 2015) also observed that shear localization in porous rocks could be stabilized by increasing pore fluid pressure during the post failure stage of faulting. This stabilizing effect of high pore fluid pressure has been explained by the dilatant hardening mechanism where the growth of cracks during brittle deformation leads to an increase in pore space, causing the pore fluid pressure to drop and the local effective stress to rise, making it harder for cracks to grow. As such, dilatancy in a fluid-saturated rocks stabilizes fault propagation and strengthens the bulk rock (Brace & Bombolakis, 1963; Frank, 1965; Rice, 1975; Rudnicki & Chen, 1988).

In this study, we investigated whether the strengthening effect of high pore fluid pressure stands true for frictional slip along gouge-bearing experimental faults. We studied phyllosilicate gouges, antigorite and chrysotile, because slow slip events have been repeatedly observed in phyllosilicate bearing seismogenic faults (e.g., Shelly, 2010). For comparison, we also studied olivine and quartz gouges. A series of velocity-

step tests were performed to measure the response of friction coefficient to variations of sliding velocity. We also measured the rate and state frictional parameters ($a-b$) and characteristic displacement D_c to quantify the slip stability. In all tests, we kept the effective pressure constant so that the effect of pore fluid pressure alone on the frictional properties of gouge materials could be discerned. We also performed microstructural observations to understand the deformation mechanisms. Our goal is to gain a better understanding of the effect of high pore fluid pressure on frictional behavior, which has important implications on the occurrence of different types of slip events in subduction zones.

3.2. Experimental Procedures

Phyllosilicate-rich rocks are common along seismogenic faults and plate boundaries. The frictional behavior of serpentines is thought to have a great influence on the behavior of faults that exhibit diverse slip modes (Okazaki & Katayama, 2015; Reinen et al., 1994; Takahashi et al., 2011). Therefore, in this study we investigate two serpentine gouge powders, the Verde Antique antigorite and Zimbabwe chrysotile. Together with olivine and quartz, San Carlos olivine and quartz powders from U.S. Silica respectively, our samples include common minerals present along plate boundaries.

For each experiment, a layer of gouge composed of 2 grams of fine-grained (<150 μm) dry serpentine powders was placed along a 30° saw-cut surface in a cylindrical porous sandstone (25.4 mm in diameter and 50.8 mm in height) shearing block (Figure 3.2). The saw-cut surface was ground with 120 grit diamond wheel to ensure a consistent surface property. The sandstone shearing blocks were made of Berea

sandstone which has a porosity of $\sim 20\%$ and permeability $\sim 5 \times 10^{-13} \text{ m}^2$ (Zhu & Wong, 1997). We added a few drops of distilled water into the dry powder to spread the gouge evenly over the saw-cut surface. The thickness of the gouge is $\sim 1 \text{ mm}$. Because the density differences between serpentine ($\sim 2.52 \text{ g/cm}^3$), olivine (3.27 g/cm^3) and quartz (2.65 g/cm^3), we adjusted the weight of the powders, i.e., $\sim 2.6 \text{ g}$ for olivine and $\sim 2.1 \text{ g}$ for quartz, in order to maintain a consistent gouge thickness.

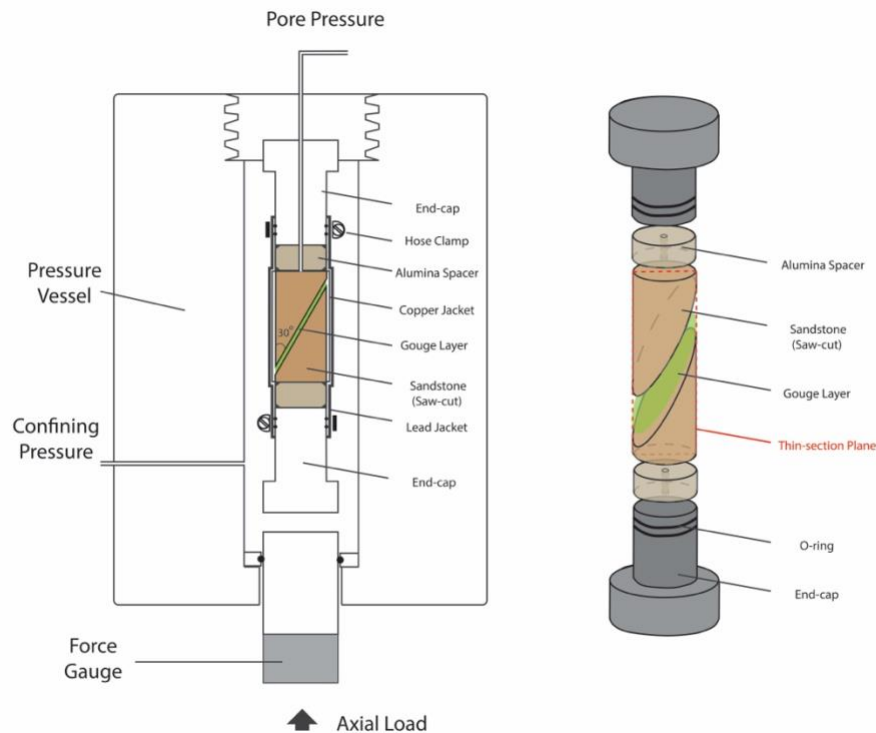


Figure 3.2: Sample and equipment configuration. A traditional tri-axial deformation apparatus is used in this study. The confining pressure and pore fluid pressure are controlled individually through external servo-controlled intensifiers. Thin sections of the sample are made along the plane marked by the red dashed line. The equipment configuration is for illustration only and is not to scale.

The gouge-filled saw-cut sample was first jacketed in a 0.0508 mm thick copper foil. The foil wrapped sample was then inserted into a 1.27 mm thick lead tube with an inner diameter of $\sim 53 \text{ mm}$. The sample assembly also included two alumina spacers and

end caps, and the lead jacket was then sealed by hose-clamps and o-rings on the end-caps (see Figure 3.2). The pore fluid access to the sample was provided by small centric holes in the alumina spacers and end caps. Argon gas and deionized water were used as the confining medium and pore fluid respectively.

Before each experiment, the sample was first brought to a confining pressure (P_c) of 20 MPa for a pre-compaction of ~15 hours. Then a pore fluid pressure (P_f) of 10 MPa was applied to purge air bubbles from the system. After that, the confining and pore pressures were changed to the desired experimental conditions for the friction experiments. For experiments conducted at 70 MPa effective pressure ($P_c - P_f$), the pore pressures ranged from 5 to 60 MPa, and the confining pressure was adjusted accordingly to keep the effective pressure constant at 70 MPa. For experiments conducted at 30 MPa effective pressure, the pore pressures ranged from 10 to 90 MPa. All experiments were conducted at room temperature.

Two series of experiments were conducted. In one series, the pore fluid pressure was kept constant under servo-control (referred to as constant pore fluid pressure experiments, CPP). Velocity stepping tests were performed and rate-and-state frictional parameters were obtained. In the CPP series, the changes in pore volume during shearing of the gouge were measured. In the other case, the pore volume was held constant during sliding by locking the piston of the pore fluid pressure intensifier (referred to as constant pore volume experiments, CPV). In the CPV tests, the change in P_f due to sample dilation and compaction were monitored. In the CPV tests, we unlocked the pore fluid pressure intensifier intermittently to keep the pore fluid pressure relatively stable. The maximum pore fluid pressure change allowed was ~5

MPa in CPV tests. Because of the changing pore fluid pressure during CPV tests, measurements of $(a-b)$ and D_c were less consistent and showed large variation due to pressure fluctuations. Thus, the $(a-b)$ and D_c from CPV experiments were not used to discuss slip behaviors.

Samples were deformed at a constant axial displacement rate (loading velocity) of 0.5 $\mu\text{m/s}$. For each deformation test, once slip along the saw-cut surface occurred (at ~ 1.5 mm axial displacement), the axial displacement velocity was stepped in increments between 0.1 and 5 $\mu\text{m/s}$ (see Table 3.1). To ensure a drained condition of gouge, during all CPP experiments, sliding velocity was chosen between 0.1 to 1 $\mu\text{m/s}$. Following each velocity change, we allowed 0.5 mm axial displacement. This gave sufficient displacement for the steady state friction to evolve and stabilize and produced a reliable measurement of rate and state friction parameters. The axial displacement was measured by a linear variable differential transformer (LVDT) affixed to the axial piston. An external force gauge was mounted at the piston outside the vessel from which the axial load (σ_1) was measured (see Figure 3.2). From the force gauge reading, differential stress ($\Delta\sigma = \sigma_1 - P_c$) can be calculated. Because the load cell was located outside the pressure vessel, a seal friction correction has been made to the differential stress reading in order to account for the o-ring seal friction (see Appendix C).

The friction coefficient μ (shear stress τ normalized by the effective normal stress on the fault plane ($\sigma_n - P_f$)) is calculated from differential stress ($\Delta\sigma$) based on the following equation:

$$\mu = \frac{\tau}{\sigma_n - P_f} = \frac{0.5\Delta\sigma\sin(2\phi)}{\Delta\sigma\sin^2(\phi) + P_c - P_f} = \frac{0.5\Delta\sigma\sin(2\phi)}{0.5\Delta\sigma(1 - \cos(2\phi)) + P_c - P_f} \quad (3.2)$$

where ϕ is the angle between the gouge layer and the axial load σ_1 . There are several sources of errors in the different stress measurements due to the apparatus configuration. In order to obtain the true stress applied on the sample, a series of corrections are required. The potential error sources and methods used to make corrections are discussed in Appendix C.

The velocity dependence factor ($a-b$) of the friction coefficient is deduced from the measurements using the rate- and state-dependent friction model (Dieterich, 1979; Ruina, 1983). Characteristic displacement (D_c) describes the displacement required for the slip to evolve to 1/e of the friction change to a new steady state following a change in slip velocity (Kilgore et al., 1993). Calculation of the velocity dependence factor ($a-b$) and the measurement of D_c are discussed in detail in the Appendix B. Pore volume changes during the experiment are calculated from the pore fluid pressure intensifier piston displacement measured by an LVDT.

The samples were epoxy impregnated after the deformation and were cut perpendicular to the shear plane and parallel to the slip vector (see Figure 3.2). Thin sections of antigorite and olivine gouges were made after the experiments and were used for microstructure analysis.

Step #	1	2	3	4	5	6	7
Velocity Steps ($\mu\text{m/s}$)	0.1 to 1 ⁽⁺⁾	1 to 0.1 ⁽⁻⁾	0.1 to 1 ⁽⁺⁾	1 to 0.1 ⁽⁻⁾	0.1 to 1 ⁽⁺⁾	1 to 0.1 ⁽⁻⁾ for CPP 1 to 5 ⁽⁺⁾ for CPV	0.1 to 1 ⁽⁺⁾ for CPP 5 to 1 ⁽⁻⁾ for CPV
Axial Displacement (mm)	~0.5	~0.5	~0.5	~0.5	~0.5	~0.5	~0.5

Table 3.1: Axial displacement rate for the step tests during each experiment. For step 6 and 7, the axial displacement rate is 1 to 0.1 and 0.1 to 1 $\mu\text{m/s}$ for CPP experiments, and 1 to 5 and 5 to 1 $\mu\text{m/s}$ for CPV experiments. (+): velocity increasing steps; (-): velocity decreasing steps.

Constant Pore Pressure Experiments (CPP)								
Gouge	P_c (MPa)	P_f (MPa)	$P_c - P_f$ (MPa)	μ	σ_{yield} (MPa)	$(a-b)^+$	$(a-b)^-$	D_c (mm)
Atg [^]	75	5	70	0.570	157.8	-0.0042 \pm 0.0010	-0.0044 \pm 0.0020	0.1471 \pm 0.0225
Atg [^]	100	30	70	0.582	155.1	-0.0025 \pm 0.0010	-0.0030 \pm 0.0016	0.1596 \pm 0.0368
Atg [^]	130	60	70	0.602	151.1	-0.0015 \pm 0.0010	-0.0035 \pm 0.0007	0.1791 \pm 0.0470
Ctl [^]	75	5	70	0.330	71.1	0.0072 \pm 0.0015	0.0047 \pm 0.0020	0.0193 \pm 0.0087
Ctl [^]	100	30	70	0.331	71.5	0.0069 \pm 0.0017	0.0072 \pm 0.0010	0.0293 \pm 0.0225
Ctl [^]	130	60	70	0.328	68.1	0.0072 \pm 0.0015	0.0069 \pm 0.0006	0.0227 \pm 0.0057
Ol [^]	75	5	70	0.694	151.0	0.0059 \pm 0.0009	0.0050 \pm 0.0009	0.0323 \pm 0.0374
Ol [^]	100	30	70	0.686	148.0	0.0064 \pm 0.0005	0.0057 \pm 0.0006	0.0316 \pm 0.0108
Ol [^]	130	60	70	0.650	145.9	0.0063 \pm 0.0005	0.0054 \pm 0.0005	0.0369 \pm 0.0094
Qz [^]	75	5	70	0.678	163.6	0.0041 \pm 0.0005	0.0025 \pm 0.0003	0.0491 \pm 0.0213
Qz [^]	100	30	70	0.678	161.4	0.0042 \pm 0.0003	0.0026 \pm 0.0006	0.0484 \pm 0.0160
Qz [^]	130	60	70	0.685	159.2	0.0043 \pm 0.0006	0.0032 \pm 0.0009	0.0523 \pm 0.0182
Atg [^]	40	10	30	0.651	69.8	0.0068 \pm 0.0020	0.0070 \pm 0.0019	0.0396 \pm 0.0097
Atg [^]	60	30	30	0.721	76.5	0.0073 \pm 0.0018	0.0056 \pm 0.0015	0.0363 \pm 0.0074
Atg [^]	90	60	30	0.640	64.7	0.0033 \pm 0.0181	0.0055 \pm 0.0045	0.0321 \pm 0.0079
Atg [^]	120	90	30	0.719	76.4	0.0083 \pm 0.0023	0.0094 \pm 0.0008	0.0323 \pm 0.0103
Controlled Pore Volume Experiments (CPV)								
Gouge	P_c (MPa)		P_f (MPa)		$P_c - P_f$ (MPa)		μ	σ_{yield} (MPa)
Atg [*]	40		10		30		0.737	63.7
Atg [*]	60		30		30		0.718	70.0
Atg [*]	90		60		30		0.629	62.2
Atg [*]	120		90		30		0.678	66.4
Ctl [*]	40		10		30		0.445	32.0
Ctl [*]	120		90		30		0.434	28.5
Ol [*]	40		10		30		0.764	70.4
Ol [*]	90		60		30		0.742	66.2
Ol [*]	120		90		30		0.747	66.8
Qz [*]	40		10		30		0.721	73.9
Qz [*]	120		90		30		0.732	73.6

Table 3.2: Summary of experiments. Atg: Antigorite; Ctl: Chrysotile; Ol: Olivine; Qz: quartz; (^): tests under constant pore pressure (CPP); (*): tests under controlled pore volume (CPV); (+): velocity increasing steps; (-): velocity decreasing steps. The $(a-b)$ values are the average of steps test \pm the standard deviation.

3.3. Results

3.3.1 Frictional Strength & Friction Coefficient from CPP Experiments

Stress-strain curves show that the yield strengths of the samples with the same gouge material deformed under the same ($P_c - P_f$) are in very good agreement (i.e., $< \sim 5\%$ variation, Figure 12), indicating that the mechanical strength obeys the effective pressure law, with effective pressure of ($P_c - P_f$). Both serpentine gouges exhibit strain hardening to a peak strength followed by subsequent strain weakening to a steady state strength (Figure 3.3a). In contrast, olivine and quartz gouges both exhibit strain hardening until a steady state strength is achieved. These results are consistent with previous experimental studies (e.g. Escartín et al., 1997; Den Hartog et al., 2014; Proctor et al., 2014).

The friction coefficient of a given gouge shows no obvious correlations with pore fluid pressure magnitude (Figure 3.3a). The two serpentines exhibit lower friction coefficients than those of olivine and quartz. Chrysotile shows the lowest friction coefficient of ~ 0.33 , while antigorite shows a range from ~ 0.57 to 0.60 . These observations are consistent with previously reported strength of serpentines (e.g. Moore et al., 1996, 2004; Proctor et al., 2014). The friction coefficients of olivine and quartz show a range from ~ 0.65 to 0.69 in agreement with previous observations (e.g. Dieterich & Conrad, 1984; Takahashi et al., 2011).

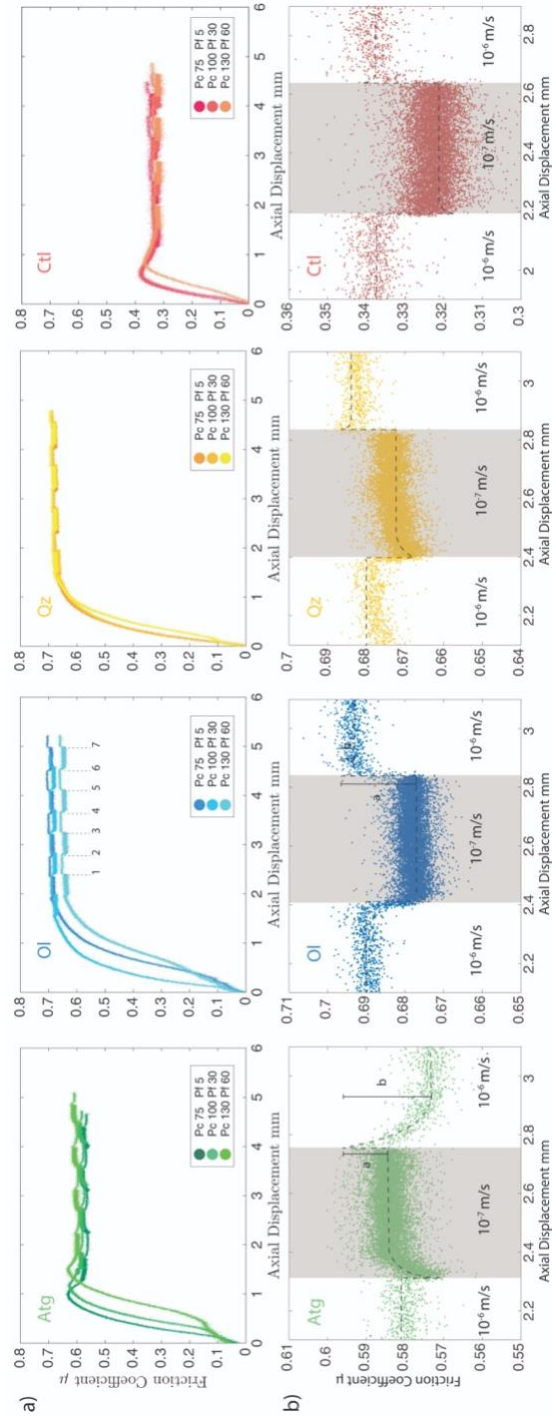


Figure 3.3: a) Friction coefficient of antigorite (green), olivine (blue), quartz (yellow) and chrysotile (red). The velocity steps where slip velocity is changed are marked in sequence in the plot of olivine friction. Results shown here are all from constant P_f experiments. b) Frictional responses to changes in slip rate. The shaded area represents friction with slower slip rate ($0.1 \mu\text{m/s}$). The frictional responses are from experiment conducted at $100 \text{ MPa } P_c$ with constant P_f of 30 MPa .

3.3.2 Velocity Dependence Factor ($a-b$) from CPP Experiments

The rate and state frictional parameter a for all gouge materials does not vary measurably for gouges of different compositions (Figure 3.3b). However, the value of b is measurably higher in antigorite compared to quartz, while olivine and chrysotile show near 0 values for parameter b (Figure 3.3b). In this study, the velocity dependence factors ($a-b$) is much better constrained from experimental data than the parameters a and b individually (Verberne et al., 2010). Therefore, only the steady state velocity-dependence ($a-b$) is discussed in further detail (Table 3.2).

Among all gouges studied here, only antigorite shows velocity-weakening behavior, ($a-b$) <0 in slip-response at the testing conditions (Figure 3.3b). Olivine, quartz and chrysotile gouges all exhibit velocity-strengthening behavior, ($a-b$) >0 . Chrysotile, while having the lowest friction coefficient, shows the most positive ($a-b$) among all the materials tested. This is consistent with the result of Ikari et al. (2011), that gouge with friction coefficient of $\mu < 0.5$, exhibit only stable sliding behavior.

An asymmetric frictional response to velocity increases and decreases is observed in ($a-b$) values (see Figure 3.13), where ($a-b$) calculations from velocity decrease steps (1 to 0.1 $\mu\text{m/s}$, Table 3.1) are lower than those from velocity increase steps (0.1 to 1 $\mu\text{m/s}$, Table 3.1). The asymmetry is more significant in olivine and quartz friction experiments. Rathbun & Marone (2013) reported that D_c is larger in velocity decrease steps than the velocity increase steps, and argued that this was due to shear localization and changes in shear fabric in fault gouge. These differences in shear localization and shear fabric may also affect the ($a-b$), leading to the asymmetry observed in our study. Due to this asymmetry, mixing ($a-b$) from velocity increases and decreases thus

exaggerates the scattering. To better illustrate the change of $(a-b)$ under different pore fluid pressure conditions, we compare results from velocity increase and decrease steps separately. The $(a-b)$ values for all velocity increase steps (0.1 to 1 $\mu\text{m/s}$) are calculated and plotted against the pore fluid pressure conditions (Figure 3.4). The $(a-b)$ results for all velocity decrease steps are given in Figure 3.14. The velocity dependence factor of the gouge materials correlates with the pore pressure. The positive slopes in Figure 3.4 shows that the $(a-b)$ values increase with increasing pore fluid pressure for all gouge materials. This indicates an apparent strengthening effect of increasing pore fluid pressure on fault slip. The strengthening effect is most significant in antigorite. Olivine, quartz and chrysotile show less significant effects from pore fluid pressure on the $(a-b)$ compared to antigorite.

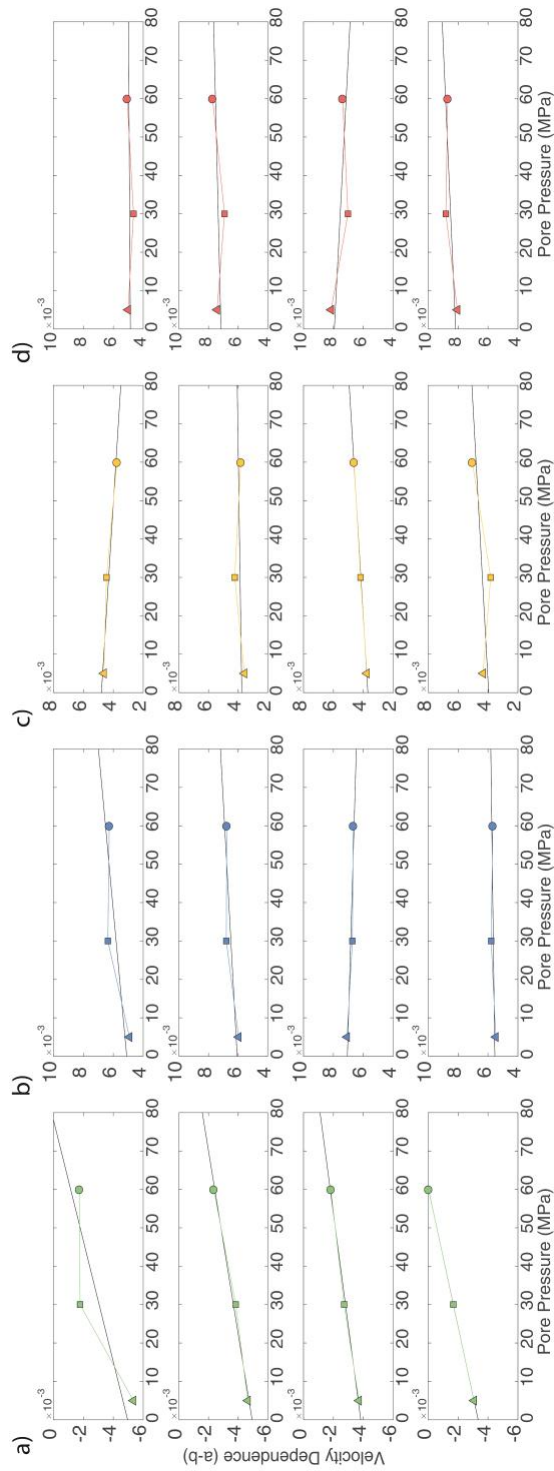


Figure 3.4: Effect of pore fluid pressure on the velocity dependence factor (*a-b*) of all tested gouges a) antigorite; b) olivine; c) quartz; d) chrysotile from velocity increase steps (0.1 to 1 $\mu\text{m/s}$). The strengthening rate of (*a-b*) from pore fluid pressure is calculated based on the slope of the fitted line in the plot. This strengthening rate is calculated for each step individually. Results shown here are all from constant P_f experiments.

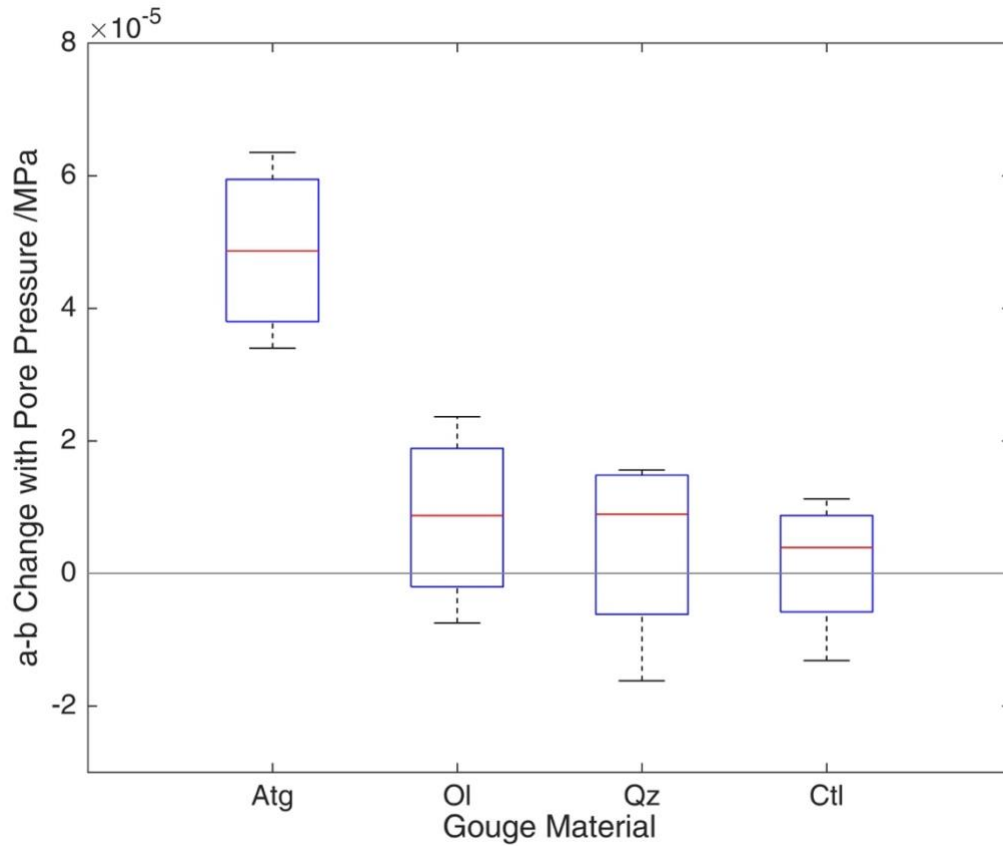


Figure 3.5: Box plot of the effect of strengthening on $(a-b)$ from pore fluid pressure. The rate of $(a-b)$ changes correspond to the slope of the fitted line in Figure 3.4. Only $(a-b)$ from velocity increase steps (0.1 to 1 $\mu\text{m/s}$) are presented in this plot.

3.3.3 Characteristic Displacement from CPP Experiments

The characteristic displacement (D_c) for each step is calculated for all materials (see Figure 3.6a) using experimental data obtained at conditions of P_c 100 MPa and P_f 30 MPa. The uncertainties in the absolute D_c values could be considerable due to the specific machine configuration. Nevertheless, the relative values of D_c for different gouges obtained at the same experimental conditions can be compared. D_c for antigorite shows an average around 0.12 mm while the D_c for olivine, quartz and chrysotile show an average of around 0.05. D_c is the largest in antigorite compared to all other materials.

We also compared D_c for each step during tests on antigorite conducted at different pore pressures ranging from 5 to 60 MPa (Figure 3.6b). Notwithstanding some scattering, D_c is generally higher in experiments at pore pressures of 30 or 60 MPa than those at 5 MPa. This suggests that higher pore fluid pressure could cause an increase in the characteristic displacement.

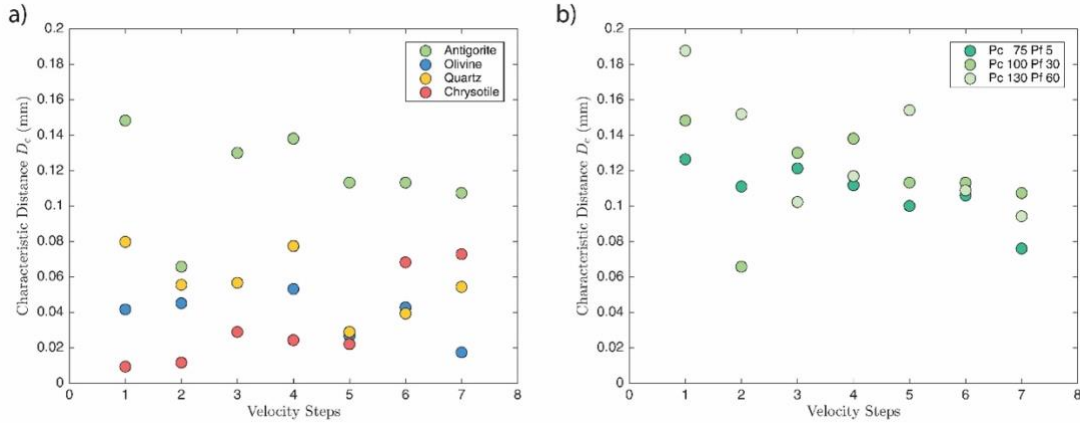


Figure 3.6: a) Characteristic displacement (D_c) of gouge materials in response to slip velocity change at different steps. All experiments shown here are conducted at 100 MPa P_c and 30 MPa P_f ; b) Characteristic displacement (D_c) of antigorite in response to slip velocity change at different pore fluid pressure conditions.

3.3.4 Pore Volume Fluctuation from CPP Experiments

Before the start of deformation in each experiment, the pore volume within the P_f intensifier is adjusted to the same level. Thus, we can assume that the total pore volume in the sample and the system is similar among all experiments at the beginning of each test. For the data presentation, pore volume at the beginning of the deformation is neutralized to 0. Compaction of the pore space is represented by negative pore volume change and dilation represented by positive pore volume change.

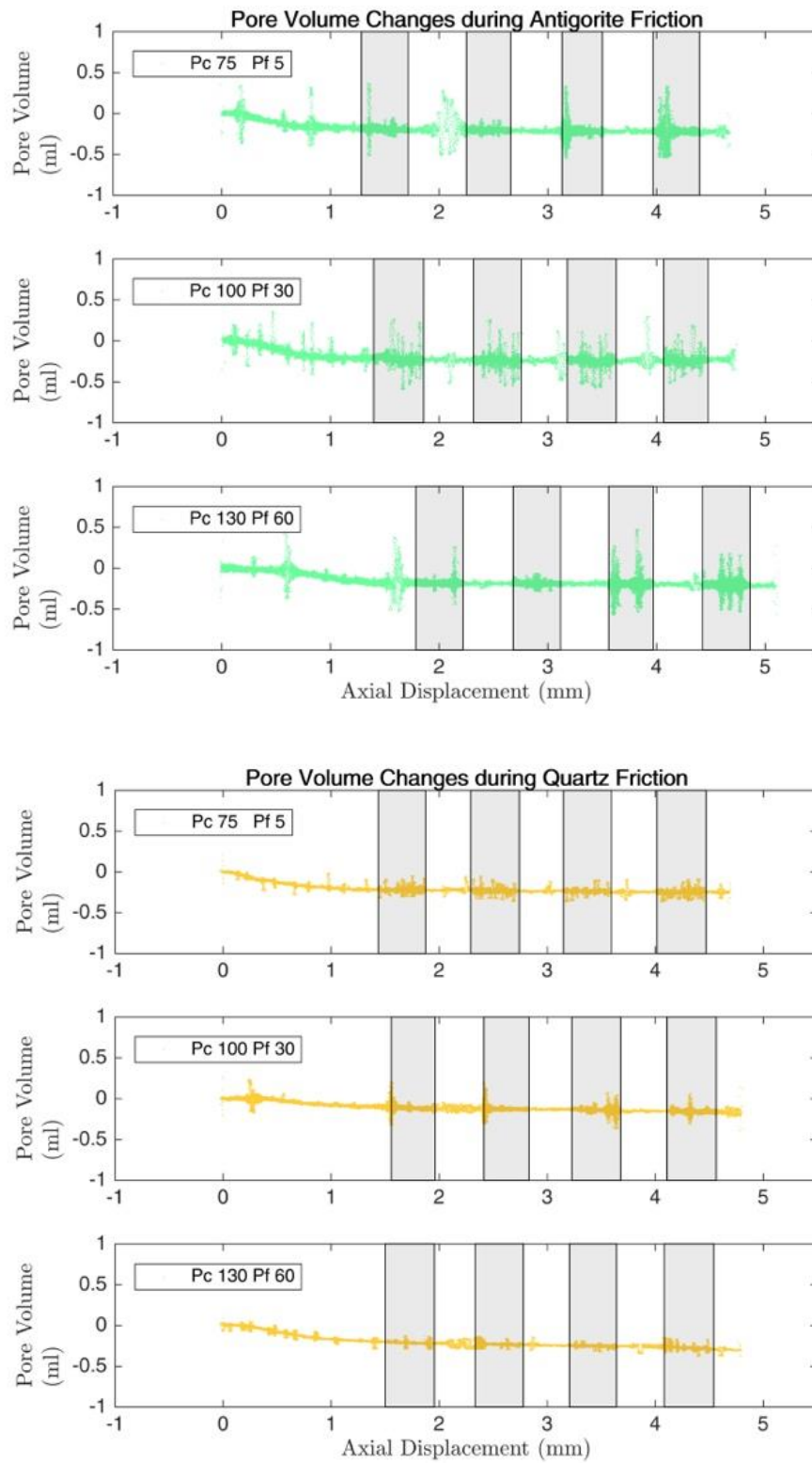


Figure 3.7: Pore volume fluctuation of antigorite (green) and quartz (yellow) during deformation. The shaded area marks the step where slip velocity is low ($0.1 \mu\text{m/s}$).

All experiments showed a net pore volume reduction (compaction) during frictional sliding (Figure 3.7). In addition, we observed transient fluctuations in pore volume, likely reflecting the responses of the servo-control to sudden changes in pore volume. Figure 3.7 shows that the pore volume fluctuation (i.e., from -0.5-0.3 mL) becomes more frequent at higher pore fluid pressure in antigorite. Comparing quartz with antigorite, the amplitude of pore volume fluctuation (i.e., -0.2-0.1 mL) is smaller. Because the (*a-b*) strengthening is more significant in antigorite than in quartz under high pore pressures, the possible link between the pore volume fluctuation and the strengthening were investigated.

3.3.5 Pore Fluid Pressure Fluctuation from CPV Experiments

To better constrain pore volume change during frictional sliding, additional experiments were conducted whereby pore volume was fixed by locking the pore fluid pressure intensifier. In this case, any change of pore volume in the sample would cause a change in the pore pressure. In the CPV experiments, the axial displacement rate for each frictional steps followed the rate listed in Table 3.1 with slip velocity ranging from 0.1 to 5 $\mu\text{m/s}$.

In samples deformed at initial pore fluid pressures less than 60 MPa, a clear and repeatable pore fluid pressure increase was observed after stopping the pore fluid pressure servo-control by locking the intensifier (Figure 3.8). In order to maintain consistent experimental conditions as in the CPP tests, we capped the pore fluid pressure fluctuation within 5 MPa by regaining servo-control of pore fluid pressure intensifier. In samples deformed at initial pore fluid pressures higher than 60 MPa,

however, little pore fluid pressure increase was observed following the lock of the intensifier.

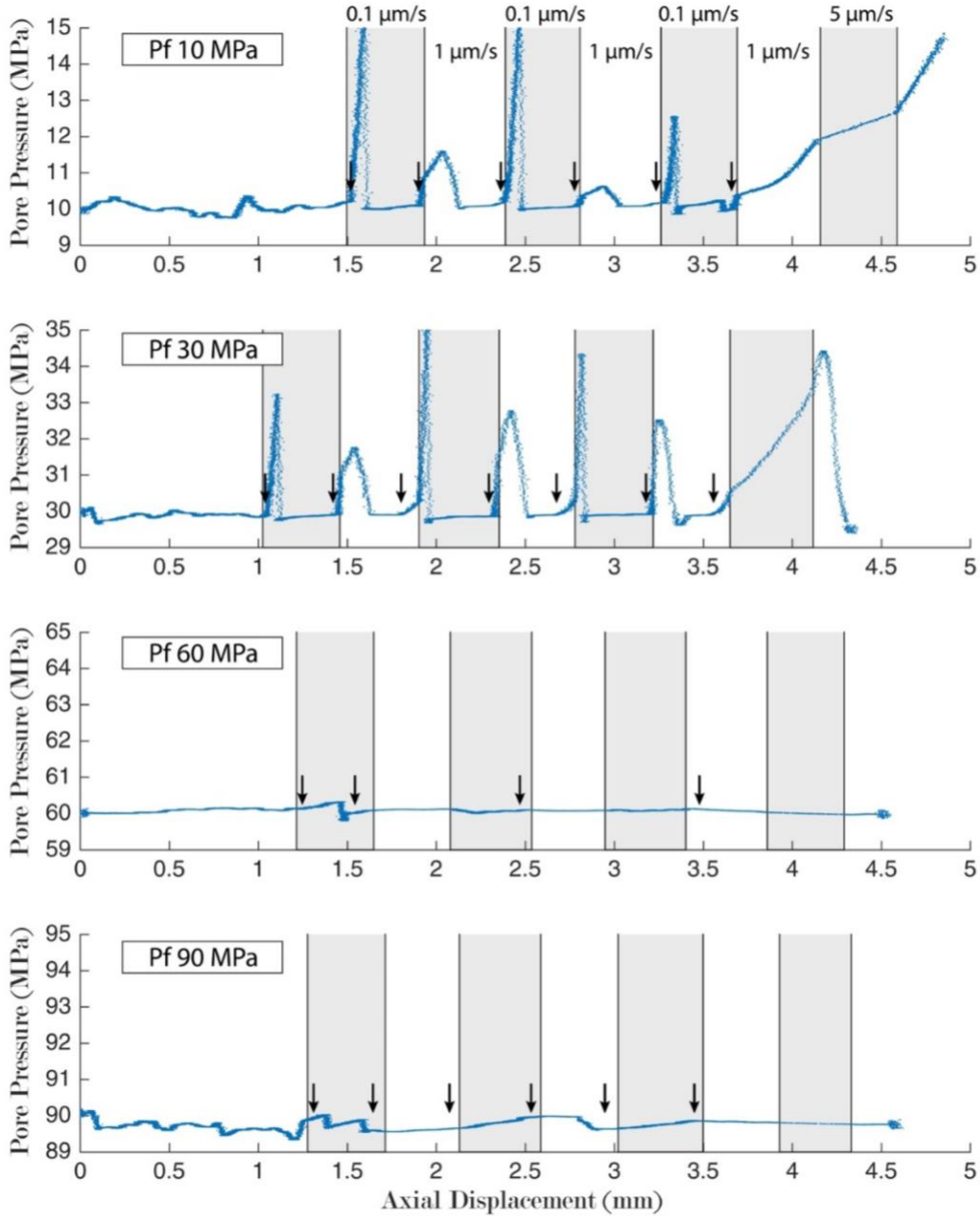


Figure 3.8: Pore fluid pressure fluctuations of antigorite during locked volume experiments. The shaded area marks the step where slip velocity is low ($0.1 \mu\text{m/s}$), except the fourth shaded area which represents a slip velocity of $5 \mu\text{m/s}$. The black arrow heads mark the point where pore volume is fixed by locking the pore fluid pressure intensifier.

During frictional sliding, both compaction (e.g., pore collapse) and dilation (e.g., fracturing) take place within the sample (e.g. Morrow & Byerlee, 1989). The competition between the compaction and dilation components determines the net (global) pore volume change. Our CPV data indicate that high pore fluid pressure suppresses compaction and/or promotes dilation.

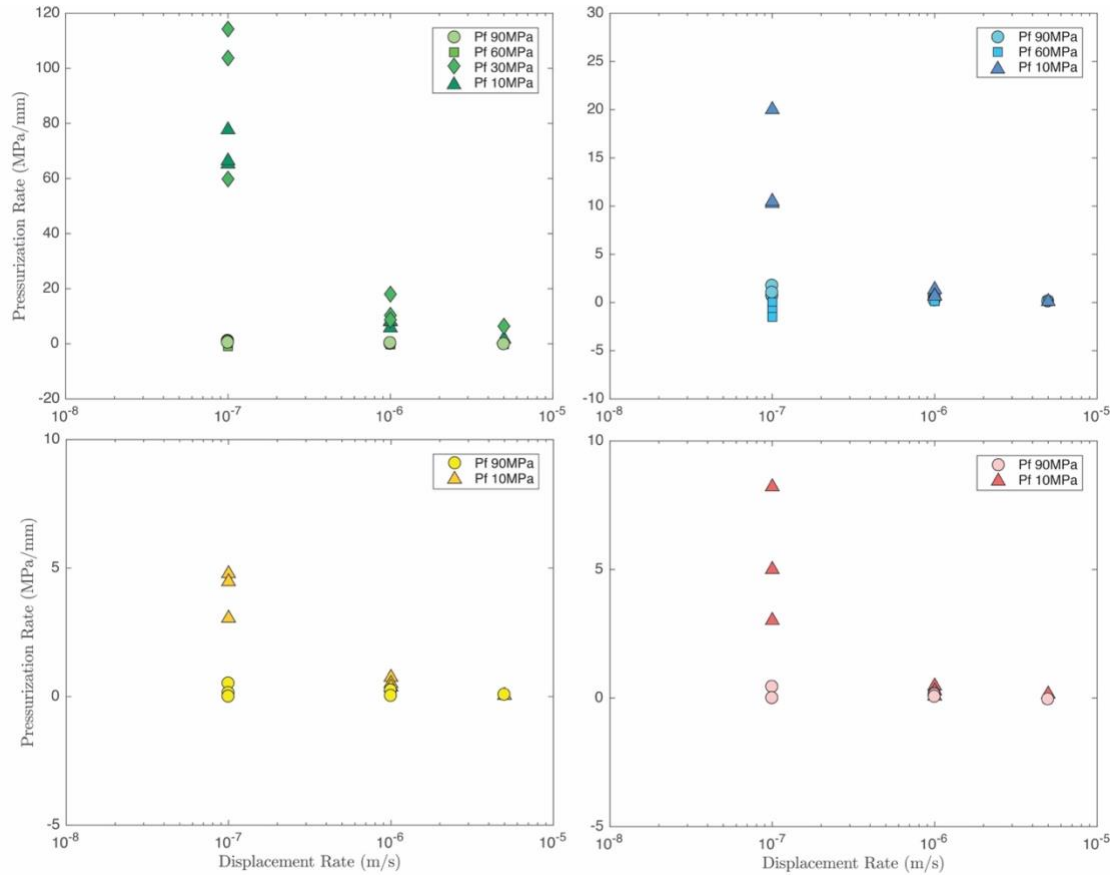


Figure 3.9: Pore fluid pressurization rate of antigorite (green), olivine (blue), quartz (yellow) and chrysotile (red), during locked volume experiments. Contrast can be observed between the fluid pressurization rate at low and high pore fluid pressure experiments.

We also calculate the pressurization rate (shown by the slope of the transient event during pore fluid pressure increase in Figure 3.8) at different pore fluid pressures following each pore volume lock and the results are shown in Figure 3.9. The pressurization rate appears higher in samples deformed at low initial pore fluid

pressures than that at high pore fluid pressures. This decrease in pressurization rate with increasing pore fluid pressure is observed in all materials (Figure 3.9). The antigorite shows the largest contrast in rate of pressurization between low and high pore fluid pressure.

The rate of pore fluid pressurization decreases with increasing slip velocity (Figure 3.9). This leads to a decrease in the contrast in pressurization rate between low and high pore fluid pressure experiments at slip velocities greater than 1 $\mu\text{m/s}$.

3.3.6 Microstructure of Deformed Gouge

The microstructure of the gouge materials is shown in Figure 3.10. Both antigorite and olivine gouges exhibit R_1 (Riedel) shear fractures at higher pore fluid pressure experiments, but not at low pore fluid pressure despite the fact that the starting materials for each experiment are independent of pore fluid pressure. Samples deformed at high pore fluid pressure seem to have fewer large grains than those deformed at low pore fluid pressures despite that the effective pressure is constant at 70 MPa for these experiments. This demonstrates that there is more extensive grain size reduction at higher pore fluid pressure than at low pore fluid pressure in antigorite and olivine. From the microstructure, the zone of comminution also seems to be much thicker in experiments with high pore fluid pressure comparing to the one at low pore fluid pressure. This indicates a thicker zone of shear at high pore fluid pressure conditions, i.e. less localization. The development of shear fracture and cracking during grain size reduction can all contribute to the pore volume dilation during deformation.

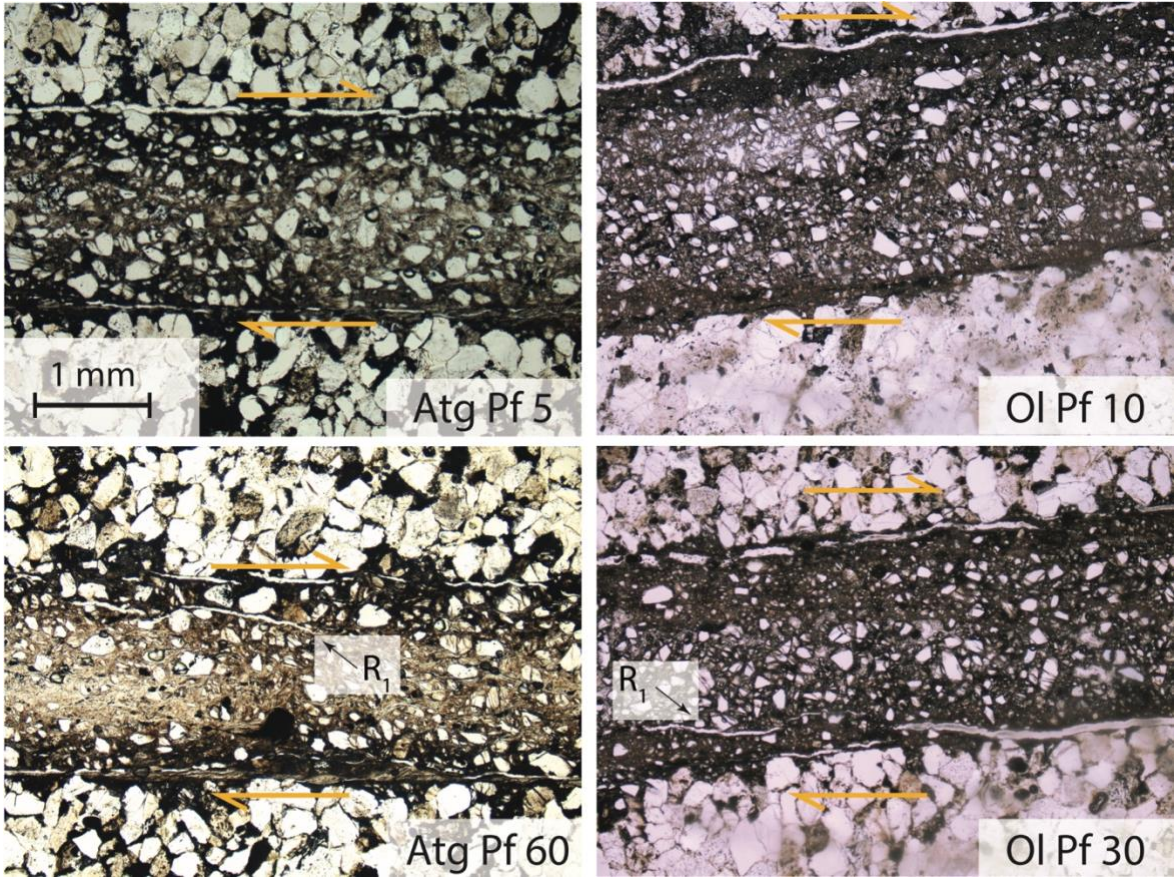


Figure 3.10: Micro-structures of antigorite (Atg) and olivine (Ol) gouge at different pore fluid pressure conditions. The orange arrow marks the shearing direction.

4. Discussion

3.4.1 Frictional Behavior Change with Increasing Pore Fluid Pressure

The friction coefficients of the tested materials are consistent with previous studies which report that the serpentines are weaker than olivine and quartz (Beeler, 2007; Dieterich & Conrad, 1984; Takahashi et al., 2011). Chrysotile is the weakest and promotes stable sliding at our experimental conditions (Ikari et al., 2011; Diane E. Moore et al., 1996, 2004).

Calculations of the velocity dependence factor ($a-b$) demonstrate that higher pore fluid pressures can cause an increase in ($a-b$), thereby stabilizing frictional slip. For

antigorite, we observed an increase in $(a-b)$ of $\sim 5 \times 10^{-5} \text{ MPa}^{-1}$ with increasing pore fluid pressure. This corresponds to $\sim 1\%$ of $(a-b)$ per MPa increase in pore fluid pressure. The lowest $(a-b)$ observed at the experimental conditions employed here is about 4×10^{-3} . This suggests that, under the same effective pressure condition, an increase in the pore fluid pressure of $\sim 80 \text{ MPa}$ could lead to a transition of the frictional behavior of antigorite from velocity-weakening to velocity-strengthening. This would correspond to a change in slip behavior from potential unstable to stable slip.

3.4.2 Pore Volume Change during Shear

The increase in pore fluid pressure that occurs during experiments where the pore volume is fixed (CPV), and the inverse correlation of pressurization with the magnitude of pore fluid pressure cannot be explained by the dependence of water compressibility on pore fluid pressure. The compressibility of water (β) is described by the equation:

$$\beta = -\frac{1}{V_p} \left(\frac{\partial V_p}{\partial P} \right)_T \quad (3.3)$$

where V_p is the specific volume, P is the pore fluid pressure, T is the temperature. From Fine & Millero (1973), we obtained the compressibility of water with respect to pore fluid pressure at room temperature. The compressibility of water decreases with increasing pore fluid pressure from $4.41 \times 10^{-4} \text{ MPa}^{-1}$ at 10 MPa to $3.62 \times 10^{-4} \text{ MPa}^{-1}$ at 90 MPa. This indicates that for the same change in pore space, a larger pore fluid pressure change should be expected at higher pore fluid pressure conditions, which is the opposite of our observations.

In our antigorite experiment from CPV, we observed a 5 MPa pore fluid pressure increase over $\sim 0.08 \text{ mm}$ of axial displacement following a lock on the pore volume during the deformation, which corresponds to a pore fluid pressurization rate of ~ 74

MPa/mm. This 5 MPa increase in pore fluid pressure is equivalent to a pore volume reduction of ~0.03 mL, assuming a total pore volume (sample + intensifier) of 14 mL. For a cylindrical sample of 25.4 mm in diameter and 50.8 mm in height, this correspond to a sample volume reduction of ~0.12%. Assuming that all pore structure change is due to gouge deformation. This would correspond to a gouge volume reduction of ~3.2%, assuming a gouge porosity of ~15% after shearing (Raleigh & Marone, 1986). Considering the change in water compressibility, the same sample volume reduction would cause 5.9 MPa pressure increase at 90 MPa pore fluid pressure. However, the observation shows almost no pressure increase at 90 MPa. This shows that the compressibility is not able to explain the change in pore fluid pressure in our study. The compaction from deformation is most likely compensated for by the greater amount of pore volume dilation at higher pore fluid pressure. We cap the pore fluid pressure change at ~5 MPa before regaining control of the pore fluid pressure intensifier using the servo. The increase in pore fluid pressure while pore volume is locked shows no trend of slowing down and would continue to increase if we had not interfered.

Based on the observations, we propose that gouge deformation (granular flow) following a change in the slip velocity is a competition between pore volume compaction and dilation (e.g., Morrow and Byerlee, 1989). If the deformation is dominated by compaction, then the net effect will be an increase on the pore fluid pressure, and likewise a decrease in pore fluid pressure indicates that the deformation is dominated by dilation. The decrease in pressurization rate with increasing pore fluid pressure demonstrates that the deformation changes from compaction-dominated at

low P_f to dilation-dominated processes at high P_f . These data suggest that compaction is suppressed and dilation is enhanced at higher pore fluid pressure conditions. In actual deformation, the compaction cannot proceed to infinite. We can then expect the compaction to become plateaued after steady state friction is achieved following a change in slip velocity. However, because the compaction and dilation take place during the evolution of friction following a change in slip velocity, we expect the competition to affect the resulted steady state friction and the evolution of friction parameters (a - b).

3.4.3 Pore Fluid Pressure Dependence of (a - b)

We propose that the pore fluid pressure dependence of (a - b) of antigorite friction may be explained by a dilatant hardening mechanism that occurs on a local scale despite the net volume changes are compactions (see illustration in Figure 3.11). When dilation takes place locally during deformation, the transient effective stress could approach the normal stress, which causes strengthening on the frictional behavior of gouge materials (Marone, 1998). By keeping (P_c - P_f) constant, the local normal stress is higher in samples under high pore fluid pressure conditions. In other words, a higher pore fluid pressure P_f level would lead to a larger effect from dilatant hardening on the strengthening of frictional behavior of materials.

This local dilation and transient effective pressure model can explain the different degrees of velocity strengthening behaviors observed in different gouges. Lower permeability gouges would be more likely to hinder draining of transient changes in fluid saturated layer and could cause stronger ‘relative strengthening’ of gouge deformation. The fact that the pore fluid pressure dependence of (a - b) is higher in

phyllosilicate gouges is consistent with experimental observations that show low permeability of phyllosilicate gouges (Faulkner & Rutter, 1998; S. Zhang et al., 1999, 2001), which would promote undrained behavior. This is also consistent with other studies that show quartz-rich gouges can maintain a high permeability, therefore limiting pore fluid pressure build up (Ikari et al., 2009; Samuelson et al., 2009).

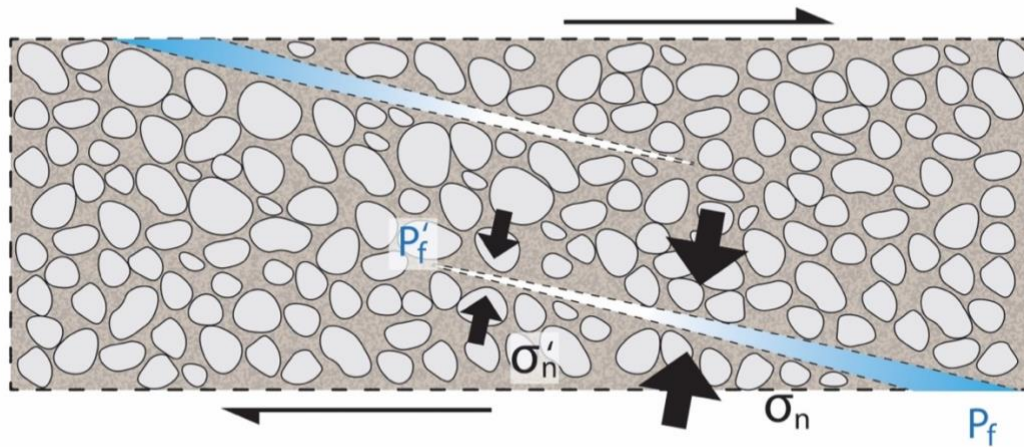


Figure 3.11: Dilatant hardening mechanism illustration. During the deformation, the far field normal stress σ_n is not perturbed. Development of cracks could cause local reduction of pore fluid pressure P'_f and lead to an increase in the local effective stress σ'_n which causes strengthening of the deformation.

The pore volume data from CPP corroborate the observed pore fluid pressure dependence of $(a-b)$. The CPP tests demonstrate that less total compaction, which we infer reflects more local dilation, occurs at higher pore fluid pressures. Greater local dilation corresponds to stronger hardening effects and is consistent with the larger increase on $(a-b)$ of the gouge materials during deformation at high pore fluid pressures.

The effect of slip velocity on fluid pressurization in the CPV tests can be explained by the effect of slip velocity on dilation. As slip velocity increases, the amount of dilation increases and compensates the compaction, leading to a decrease in the pressurization rate of pore fluid. This effect of slip velocity on dilation has also been shown by previous studies (e.g. Morrow & Byerlee, 1989). This stands true for all tested gouge although the largest effect is seen during deformation of antigorite. It is noted that at high slip rates, it is harder to ensure the pore fluid drains effectively. Under undrained conditions, the pore fluid pressure data do not reflect the actual pore fluid pressure changes within the gouge. However, at low slip rates, the gouge is considered as drained and the pore fluid pressure measurement would more accurately track the pressure within the gouge. We calculated the diffusion time which describes the time for the fluid in the gouge to equilibrate after perturbations using the following equation:

$$t = \frac{h^2 \beta \eta}{2k} \quad (3.4)$$

where h is the diffusion length, β is the compressibility of the gouge, η is the viscosity of the fluid and k is the permeability of the gouge. We adopt the compressibility value of 10^{-10} Pa^{-1} and fluid viscosity of $0.001 \text{ Pa}\cdot\text{s}$ based on Faulkner et al. (2018). We assume a gouge permeability of 10^{-20} m^2 (Coble et al., 2014; Ikari et al., 2009). The calculated diffusion time is $\sim 1.25 \text{ s}$. The gouge compaction takes place at grain contact scale of $\sim 1 \mu\text{m}$. When slip rate is at $5 \mu\text{m/s}$, the time scale for compaction is $\sim 0.2 \text{ s}$. In this case, the gouge can be considered as undrained. While at slip rate of $1 \mu\text{m/s}$ or lower, the compaction takes place at a time scale of $1\sim 10\text{s}$. Therefore, the gouge is drained at slip rate of 0.1 to $1 \mu\text{m/s}$.

Because the (*a-b*) measurement discussed here are all taken from CPP experiment, where steps test are conducted with slip rate between 0.1 to 1 $\mu\text{m/s}$, the (*a-b*) dependence on pore fluid pressure from this experiment is not affected by the undrained conditions. According to the observations from CPV experiments, change in the pressurization rate is most significant in antigorite with increasing pore fluid pressure conditions. This indicates a larger amount of change in dilation, thereby larger increase in strengthening from dilatant hardening is expected in antigorite which leads to the more significant increase in (*a-b*). Apart from the pore fluid pressure data, the presence of R_1 shear fractures from microstructure analysis in the gouge at higher pore fluid pressure conditions could also be the evidence for higher amount of dilation and larger effect from dilatant hardening. The larger amount of grain size reduction could also contribute to the dilation through the associated cracking, and eventually strengthening on (*a-b*) of the materials.

The effect of dilatant hardening on the deformation has been observed in previous studies. Ikari et al. (2009) suggested that a low pore fluid pressure could reduce the potential for velocity strengthening because compaction in forms of consolidation and cementation is favored at low pore fluid pressure. However, this is discussed in a context of high effective pressure due to the low pore fluid pressure. Our observations suggest that dilation may also be affected by the absolute pore fluid pressure level where dilation increases as the pore fluid pressure level becomes elevated. French & Zhu (2017) have found that high pore fluid pressure impedes the rate of fault propagation in intact serpentinite, leads to strengthening of the material and more stable failure. The results from this study demonstrated that dilatant hardening could have a

significant effect on the friction deformation of gouge materials and lead to an apparent strengthening on the friction parameters with increasing pore fluid pressure.

3.4.4 Characteristic Displacement (D_c)

The characteristic displacement of antigorite appears to be ~5 times higher than any other gouge materials. In the critical stiffness friction stability criterion, larger D_c would lead to a lower critical stiffness of the antigorite gouge. This suggests that the slip of antigorite is more likely to favor slow-slip than all other materials studied here under room temperature conditions.

For antigorite friction, higher pore fluid pressure also leads to an increase in the characteristic displacement (Figure 3.6b). This observation is consistent with the discovery of French & Zhu (2017), who suggested that the dilatancy hardening causes an increase in the slip weakening distance. Increase in D_c would reduce the critical stiffness and, therefore, favor stable sliding. The parameter D_c has been correlated with the thickness of the zone of localized shear strain (Marone & Kilgore, 1993). The thicker zone of comminution from the microstructure of high pore fluid pressure experiments also seems to support a more distributed zone of deformation (Figure 3.10). The distributed deformation would favor a more stable slip comparing to localized deformation. This is also consistent with our observation on the increase of $(a-b)$ due to higher pore fluid pressure.

3.4.5 Slow Slip in Serpentine

The observed dependence of friction parameters on pore fluid pressure suggests that, in addition to the inherent material properties, dilatant hardening in gouge

materials could potentially lead to slow slip (Segall et al., 2010). From the observations of this study, the largest effect of dilatant hardening is seen during deformation of antigorite. It is reasonable to infer that frictional deformation characteristics of antigorite are the most likely to produce slow slip of the gouges that we tested. We propose that slip that occurs in regions with large presence of the antigorite or gouge with similar frictional properties and high pore fluid pressure would likely favor slow slip.

The strengthening effect of the dilatant hardening mechanism has been discussed in several studies. However, our study showed that it is necessary to consider the absolute level of pore fluid pressure especially when pore fluid pressure is high. The enhanced rate-strengthening of friction could come from both effective pressure reduction and pore fluid pressure increase. For antigorite gouges, the high pore fluid pressure could cause a transition in the frictional behavior from unstable to stable slip. This observation is especially important in regions such as subduction zones, transform faults, and mid-ocean ridges where large amounts of fluid are brought to the fault slip plane to induce extensive serpentinization.

Although our experiments are all conducted at room temperature, the findings of this study also seem to be valid at high temperature conditions. Takahashi et al. (2011) observed stick-slip behavior in serpentine at $\sim 500^{\circ}\text{C}$. Interestingly, Okazaki & Katayama (2015) found slow slip in serpentine at above 500°C , and argued that dehydration in serpentine was responsible for the observed slow slip. It is plausible, that the slow slip is linked to the elevated pore fluid pressure produced by serpentine dehydration at higher temperature. This implies that our observation that high pore fluid

pressure promotes slow slip could also apply to high temperature conditions. French & Zhu (2017) found that high pore fluid pressure has a stabilizing effect on fault propagation at 23 and 150°C. These findings suggest that the strengthening effect of pore fluid pressure observed in this study may be applicable to high temperature conditions as well.

3.5. Conclusions

Based on the observations in this study, we have found that:

- Serpentine minerals (both antigorite and chrysotile) show lower friction coefficient compared to the olivine and quartz.
- Chrysotile, olivine and quartz are velocity strengthening with similar magnitude of (a-b) while antigorite is velocity weakening with negative (a-b). However, stick-slip events are not observed in this study.
- High pore fluid pressure leads to an increase in (a-b) of gouge materials with the largest effect seen in antigorite.
- At the same effective pressure, the net pore volume reduction during shear diminishes at high pore fluid pressures, indicating less compaction and/or more dilation at these conditions.
- The dilatant hardening mechanism seems to be a possible explanation of the effect of high pore fluid pressure on increasing the magnitude of the values of (a-b).
- Under the same effective pressure conditions, increasing pore fluid pressure would likely lead to a transition in friction from velocity-weakening to velocity

strengthening, which favors transitional slip behaviors such as slow slips and tremors.

The experimental results of this study demonstrate that high pore fluid pressure can promote the increase of velocity dependence ($a-b$) of gouge materials and can change the frictional behavior from velocity-weakening to velocity-strengthening. This could potentially result in a transition from seismic slip to aseismic creep fault behavior. It helps in explaining the resting of stick-slip earthquakes in regions with the presence of high pore fluid pressure. This study shed light on the importance of taking into the account high fluid pressure when discussing fault slip. It is also likely that other types of minerals will also exhibit modifications of fault behavior with the presence of high fluid pressure. This remain to be tested through further extensive study on other materials.

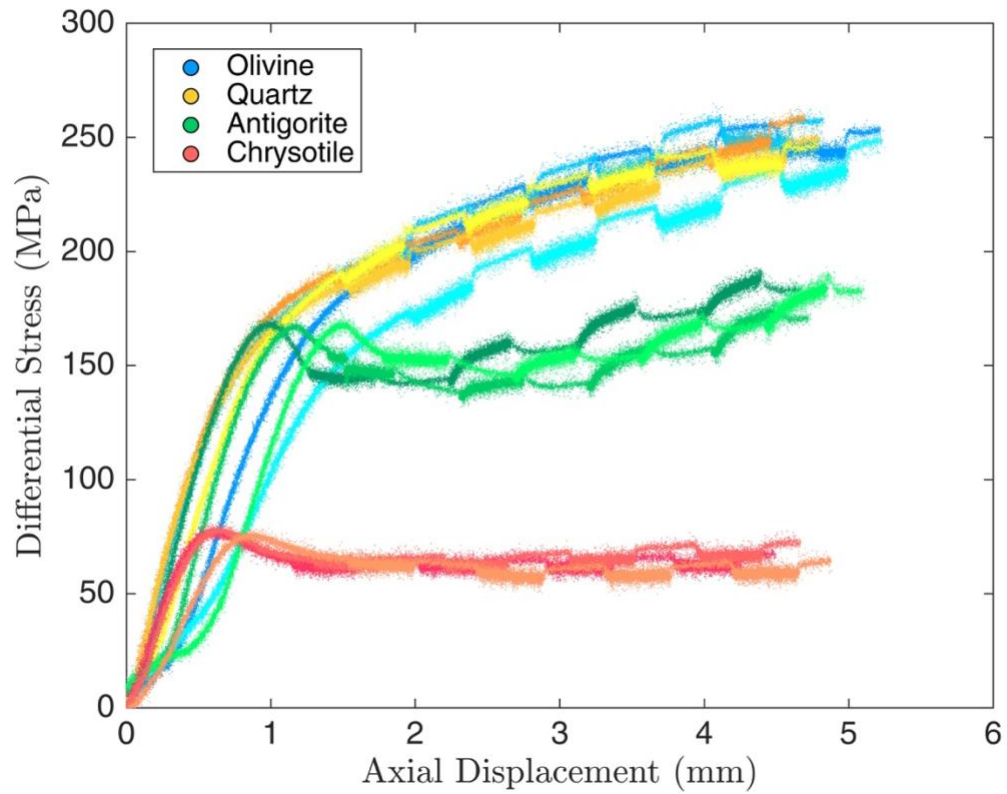


Figure 3.12: The differential stress vs axial displacement for all tested gouges. The experiments presented here were all conducted at 70 MPa effective pressure, with pore fluid pressure from 5 to 60 MPa. The samples show similar loading curves and yield points.

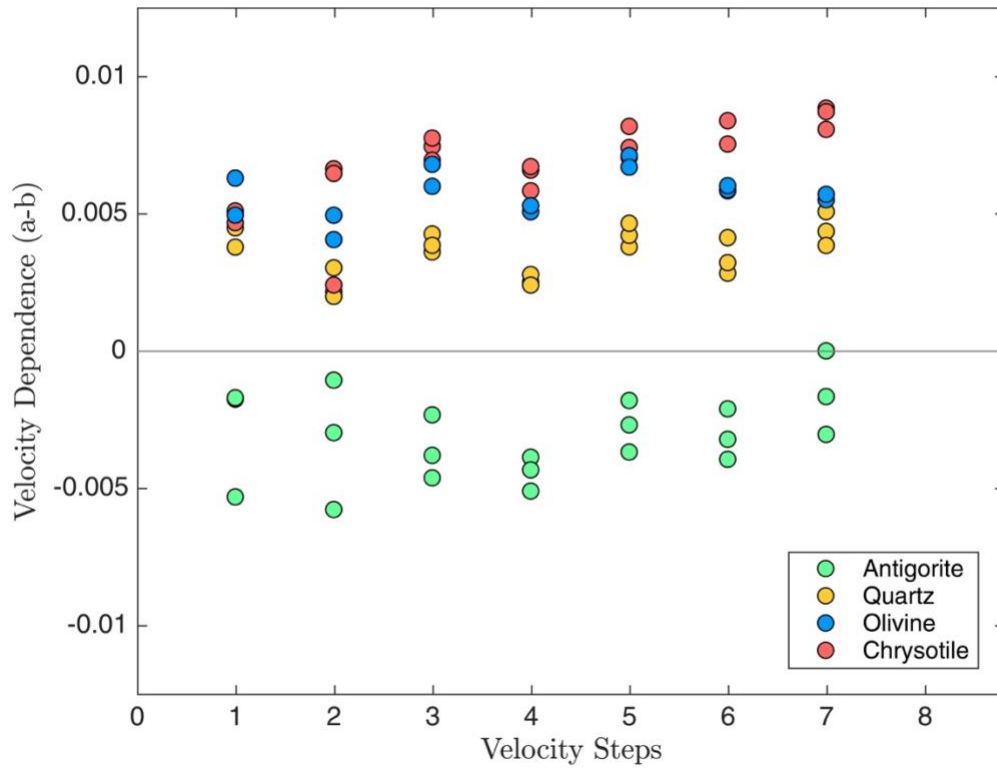


Figure 3.13: The velocity dependence factors (*a-b*) of all tested gouge materials deformed at 70 MPa effective pressure.

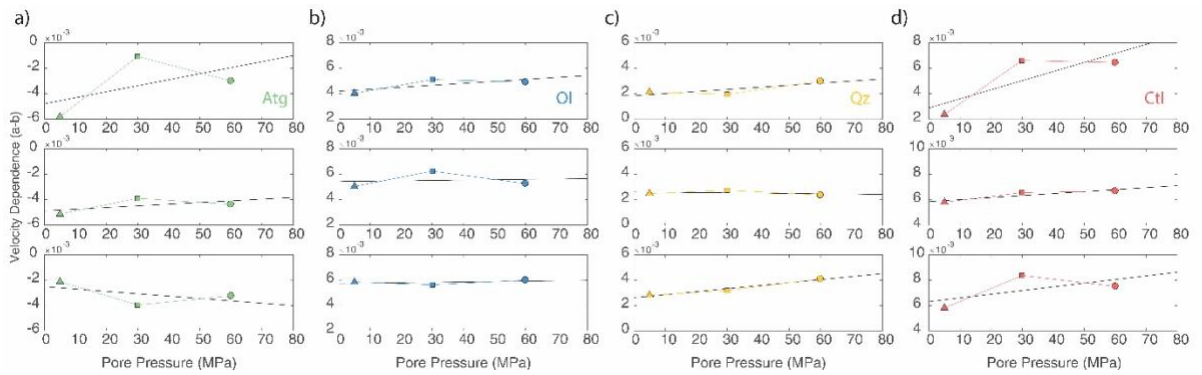


Figure 3.14: Effect of pore fluid pressure on the velocity dependence factor (*a-b*) of all tested gouges a) antigorite; b) olivine; c) quartz; d) chrysotile from all velocity decrease steps (1 to 0.1 $\mu\text{m/s}$).

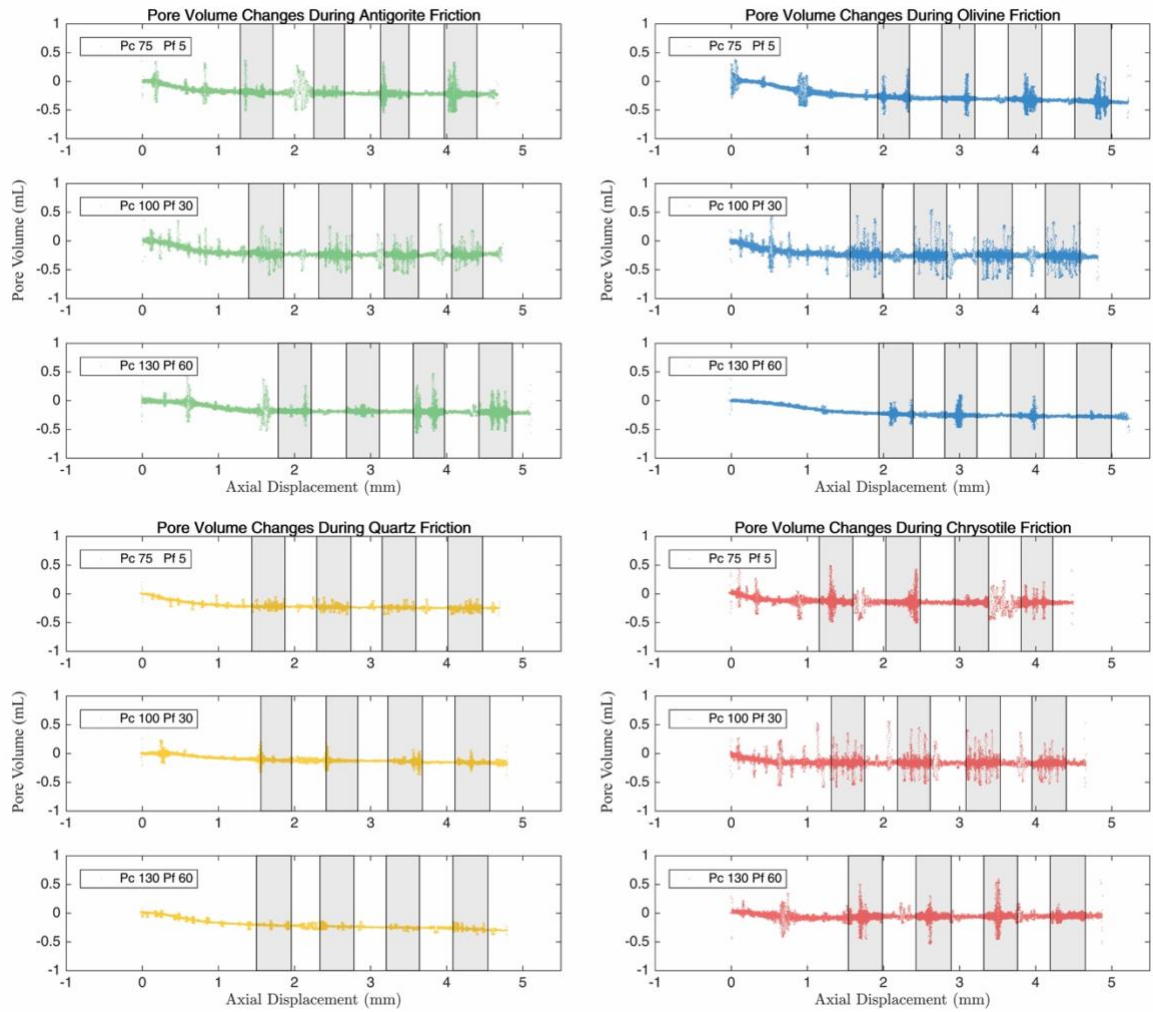


Figure 3.15: Pore volume fluctuation of antigorite (green), olivine (blue), quartz (yellow) and chrysotile (red) during deformation. The shaded area marks the friction where slip velocity is low ($0.1 \mu\text{m/s}$).

Chapter 4: Pressure Dials to Tune Slip Events between Slow and Fast

Abstract

We conducted deformation experiments to investigate how slip events along gouge-bearing faults change from slow to fast and back as pressure conditions change. A layer of fine-grained quartz gouge was placed between the saw-cut surfaces of porous sandstone samples that were subjected to conventional tri-axial loading. By changing the confinement and/or pore fluid pressure, our deformation experiments produced different slip events, from dynamic, audible stick-slip to slow, silent slip. Our data show that under the same pore fluid pressure, increasing effective pressure produces larger dynamic stick-slip events. However, there exists a threshold (~100 MPa for the fine-grained quartz gouge used in this study) beyond which stick-slip events are prohibited and creep takes place. In contrast, under the same effective confinement, increasing pore fluid pressure causes a transition from stick-slip to slow-slip in the same fault. Based on the experimental results, we propose a synoptic view of the slip instability as a function of depth and pore fluid pressure along subduction interfaces.

4.1 Introduction

Earthquakes are one of the most commonly occurring natural hazards. Reid (1911) proposed the elastic rebound theory which states that an earthquake cycle consists of two distinct phases, an interseismic strain accumulation phase when a portion of a tectonic fault is locked, and a coseismic release phase when a sudden strain release takes place by rupturing the locked portion of the fault. In this model, the deficit of slip

accumulated during the interseismic phase should be balanced by the seismic slip and aseismic creep.

Recent geophysical observations have revealed a new type of slip behavior, the slow slip. Slow slip events (SSEs) proceed at rates much slower than earthquakes (e.g., ~m/s) but faster than plate motions (e.g., mm to cm per year). SSEs can last from a few seconds to years and generally only low frequency elastic waves are radiated (Obara, 2002; Peng & Gomberg, 2010). SSEs are observed in many tectonic settings, from subduction zones to transform faults (Audet & Schaeffer, 2018; Hirose & Obara, 2010; Lowry, 2006; Vergnolle et al., 2010). Studies have been conducted searching for connections between the mechanism of slow slip and dynamic slip (Ikari et al., 2013; Peng & Gomberg, 2010; Wech & Creager, 2011). The results show that the slip modes span a continuum between slow earthquakes and the dynamic fault slip. They suggest that the SSEs could be an important part of the seismic cycle and represent the transition between the viscously creep and the dynamic, seismogenic slip (Peng & Gomberg, 2010). However, the governing mechanism of SSEs remains enigmatic.

In regions where SSEs are commonly observed, seismic studies have revealed the presence of high v_p/v_s ratio which is interpreted as evidence for near-lithostatic pore fluid pressure (e.g. Audet & Schaeffer, 2018; Kodaira et al., 2004; Shelly et al., 2006). Many studies have related the presence of high pore fluid pressure to the occurrence of SSEs and suggest that presence of high pore fluid pressure could modify the slip behavior and lead to transitions from dynamic slip to slow slips (Audet et al., 2009; Ito & Obara, 2006; Kitajima & Saffer, 2012; Scholz, 2002).

Brace & Byerlee (1966) postulated that stick-slip on pre-existing faults is the source of earthquakes above the seismogenic depths. Stick-slip can be described as a self-sustaining oscillatory motion occurs at the transition between stable and unstable frictions (Scholz, 1998; Scholz et al., 1972). Byerlee and Brace (1968) found that confining pressure exerts a primary control over motion on a nominally dry laboratory fault. For a given fault (i.e., same rock type and surface roughness), motion can take the form of stable sliding at low confining pressures and stick-slip at intermediate and high pressures. They observed that the amplitudes of stress drop of stick slip events increase with confinement.

When pore fluids are present, the frictional instability of a fault is governed by the effective pressure ($P_e = \text{confining pressure } P_c - \text{pore fluid pressure } P_f$) (Terzaghi, 1943). For example, recent experimental studies have shown that variations in effective pressure could lead to transitions from dynamic stick-slip to slow-slip and tremors (Leeman et al., 2016). Studies on fluid injection have demonstrated the effect of pore fluid pressure on stabilizing fault slip (Cappa et al., 2019). To date, the effects of pore fluid pressure are mostly studied in the context of changing effective pressure. Whether and how pore fluid pressure alone (i.e., under a constant effective pressure) can affect deformation and frictional instability is not well understood.

French and Zhu (2017) studied the fault localization and propagation in intact serpentinites under various pore fluid conditions. Their results demonstrated that at the same effective pressure, higher pore fluid pressure reduces the fault propagation rate and causes a transition of faulting style from dynamic to quasi-stable. This stabilizing effect of high pore fluid pressure has been explained by the dilatant hardening

mechanism where the growth of cracks during brittle deformation leads to an increase in pore space, causing the pore fluid pressure to drop and the local effective stress to rise, making it harder for cracks to grow. A similar effect from dilatant hardening has also been shown in gouge materials which cause the increase in rate-dependent friction parameters ($a-b$) and D_c , leading to stabilization of fault slip (Chapter 3). Segall et al. (2010) suggested that changes in the draining condition of the material during slip could cause the rise of SSEs. As slip accelerates, deformation becomes effectively undrained. In this case, dilatancy-induced pore fluid pressure reductions may quench the dynamic slip and cause the stabilization of fault slip.

Based on the existing experimental data, we hypothesize that when the pressure conditions are right, transitions between stick-slip and slow-slip can be achieved in any seismogenic fault. To test this hypothesis, we conduct experiments to investigate how increasing effective pressure enhances stick-slip, how increasing pore fluid pressure impedes stick-slip, and how the right combination of the pressure conditions could change slip behavior from fast to slow and in between. The stress drop, slip rate, elastic energy release, and moment magnitude-frequency characteristics of the observed slip events are analyzed. Our data provide new mechanical insights on the slow slip events that are commonly observed in subduction zones and other tectonic settings.

4.2 Sample Configuration and Experimental Procedures

The laboratory fault is a 30° saw-cut in a porous sandstone. The saw-cut surface is ground with a 120-grit diamond wheel to ensure a consistent surface property. Prior to the saw-cut, the cylindrical sandstone sample is 25.4 mm in diameter and 50.8 mm in height. The saw-cut was filled with fine-grained quartz powders from U.S. Silica. The

mean grain size of the quartz gouge was $3.4\ \mu\text{m}$. We added 3-4 drops of water to the dry quartz powder before spreading the damp gouge evenly along the saw-cut surfaces. The same amount of quartz powder (with a dry weight of $0.5\ \text{g}$) was used, to ensure a consistent gouge thickness of $\sim 0.18\ \text{mm}$ in each test. The porous sandstone was chosen as shearing block because of its high porosity ($\sim 20\%$) and permeability ($\sim 10^{-13}\ \text{m}^2$) which allows an easy access of pore fluid to the fault surfaces. The sample was jacketed using 2 layers of polyolefin tubes and joined with alumina spacers and steel end-caps (Figure 4.1).

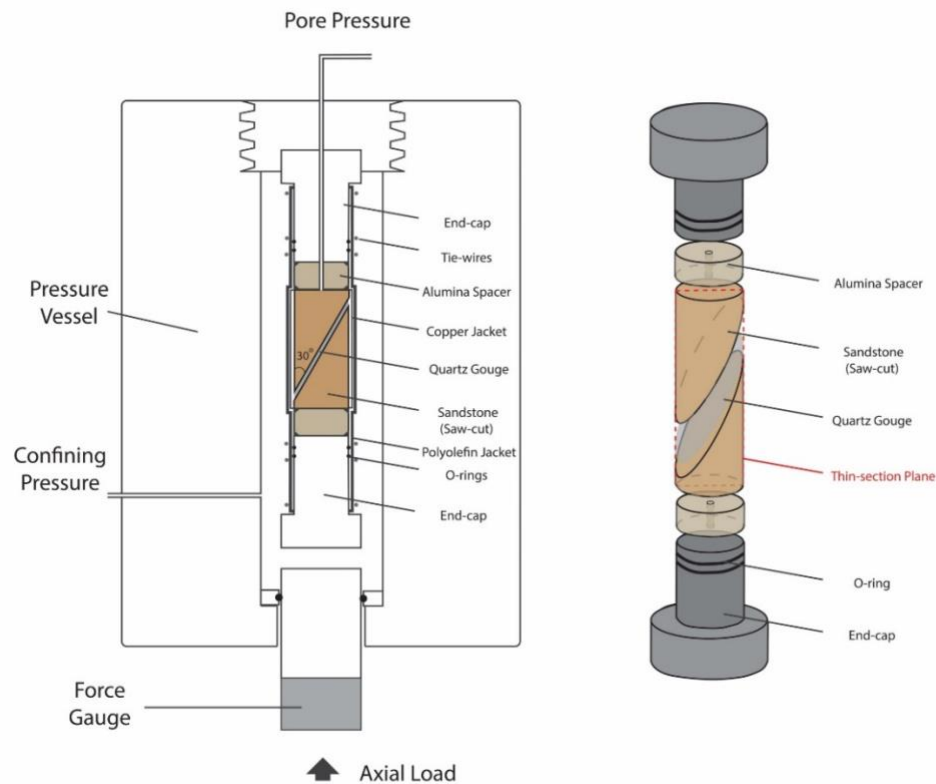


Figure 4.1: Experimental setup. Conventional tri-axial compression tests ($\sigma_1 > \sigma_2 = \sigma_3$) were conducted on porous rocks with a 30° saw-cut filled with fine-grained quartz gouge. Slip behaviors along the saw-cut surfaces combinations of confinements ($P_c = \sigma_2 = \sigma_3$) and pore fluid pressures (P_f) were recorded and analysed. The dashed red rectangle marks where the thin section of the deformed sample was taken.

Conventional tri-axial compression tests were conducted, where maximum principal stresses (σ_1) is greater than intermediate principal stress (σ_2) and minimum principle stress (σ_3). The σ_2 and σ_3 are controlled by the confinement pressure i.e. $\sigma_2 = \sigma_3 = P_c$. An external force gauge was mounted at the piston outside the vessel from which the axial load (σ_1) was measured, from which the differential stress ($\sigma = \sigma_1 - \sigma_3$) was determined. The axial displacement (d) on the sample was obtained using a linear variable differential transformer (LVDT) affixed to the axial piston (Figure 4.1). The shear displacement (s) was deduced using equation (4.1):

$$s = \frac{2\sqrt{3}}{3}d \quad (4.1)$$

Two series of experiments were conducted to investigate the respective effects of confining and pore fluid pressure on slip instabilities. We either keep the pore fluid pressure (P_f) constant at 5 MPa and vary the effective pressure P_e from 30 to 100 MPa, to examine the effective of normal stress on deformation (referred to as effective pressure series experiments, EPS), or keep the effective pressure at 70 MPa and vary the pore fluid pressure from 5 to 120 MPa, to examine the effective of pore fluid pressure on deformation (referred to as pore fluid pressure series experiments, PPS).

In each experiment, the saw-cut sample is loaded using an axial displacement rate of 0.5 $\mu\text{m/s}$ to the yield stress σ_{yield} (Table 4.1) beyond which slip along the saw-cut occurs. We then changed the axial displacement rate to 1 $\mu\text{m/s}$. For each experiment, a total shear displacement of ~ 6 mm is achieved, and the slip events were recorded. The correction that accounts for the differential stress change as the overlapping frictional

area reduces during accumulative slip is shown in Appendix B. The shear stress on the gouge material is calculated based on the differential stress (see Appendix B).

Sample	P_c	P_f	$P_e = P_c - P_f$	σ_{yield}
EPS 30-5	35	5	30	83.9
EPS 60-5	65	5	60	149.4
EPS 70-5*	75	5	70	154.7
EPS 80-5	85	5	80	175.6
EPS 100-5	105	5	100	203.6
PPS 70-30	100	30	70	156.2
PPS 70-60	130	60	70	158.8
PPS 70-90	160	90	70	153.7
PPS 70-120	190	120	70	155.0

Table 4.1: Pressure conditions and yield stress for each experiment. (*This test fits in both EPS and PPS series. EPS 70-5 can also be called PPS 70-5)

4.3 Results

4.3.1 Pressure Dependence of Slip Events

In our experiment, stress-strain curves show that the yield strength σ_{yield} of the samples correlates well with the effective pressure (see Figure 4.13). The yield strengths of samples deformed under the same effective pressure, but different pore fluid pressures are in very good agreement (i.e. <3% variation, see Table 1). This indicates that the mechanical strength of samples in this study obeys the effective pressure law.

Beyond σ_{yield} , initial sliding on the fault is stable (see Figure 4.2). Stick-slip events started to emerge after ~1 mm shear displacement after slip starts. These are represented by the periodic stress accumulations and releases as shearing continues. Given the initial gouge layer thickness of ~0.18 mm, this corresponds to a shear strain of >5 at the start of the stick-slips.

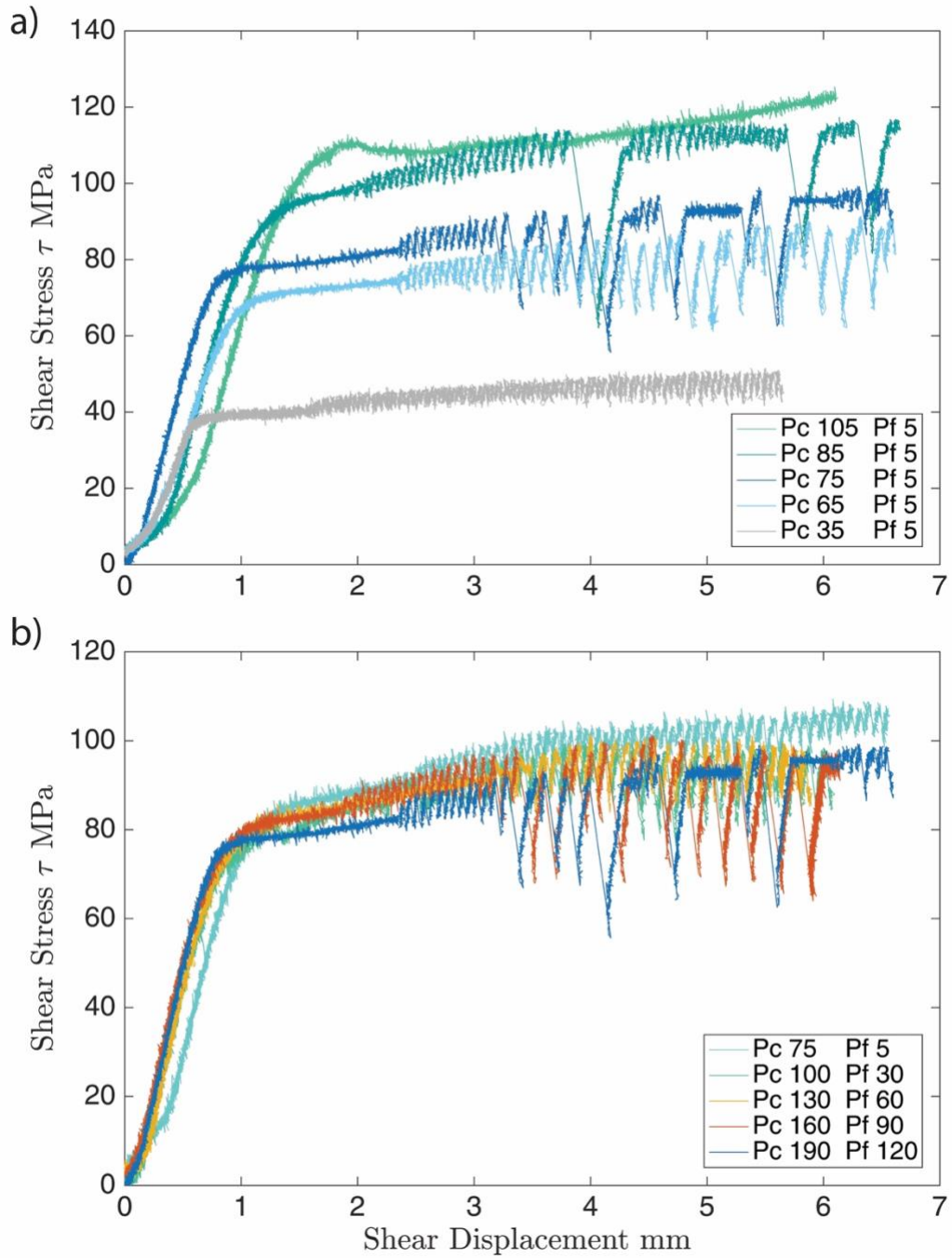


Figure 4.2: Stress-Strain curves of saw-cut samples deformed at various confinements and pore fluid pressure. Deformation and slip behaviors were investigated under a) various confinements and a constant pore fluid pressure, b) various pore fluid pressures and a constant effective confinement.

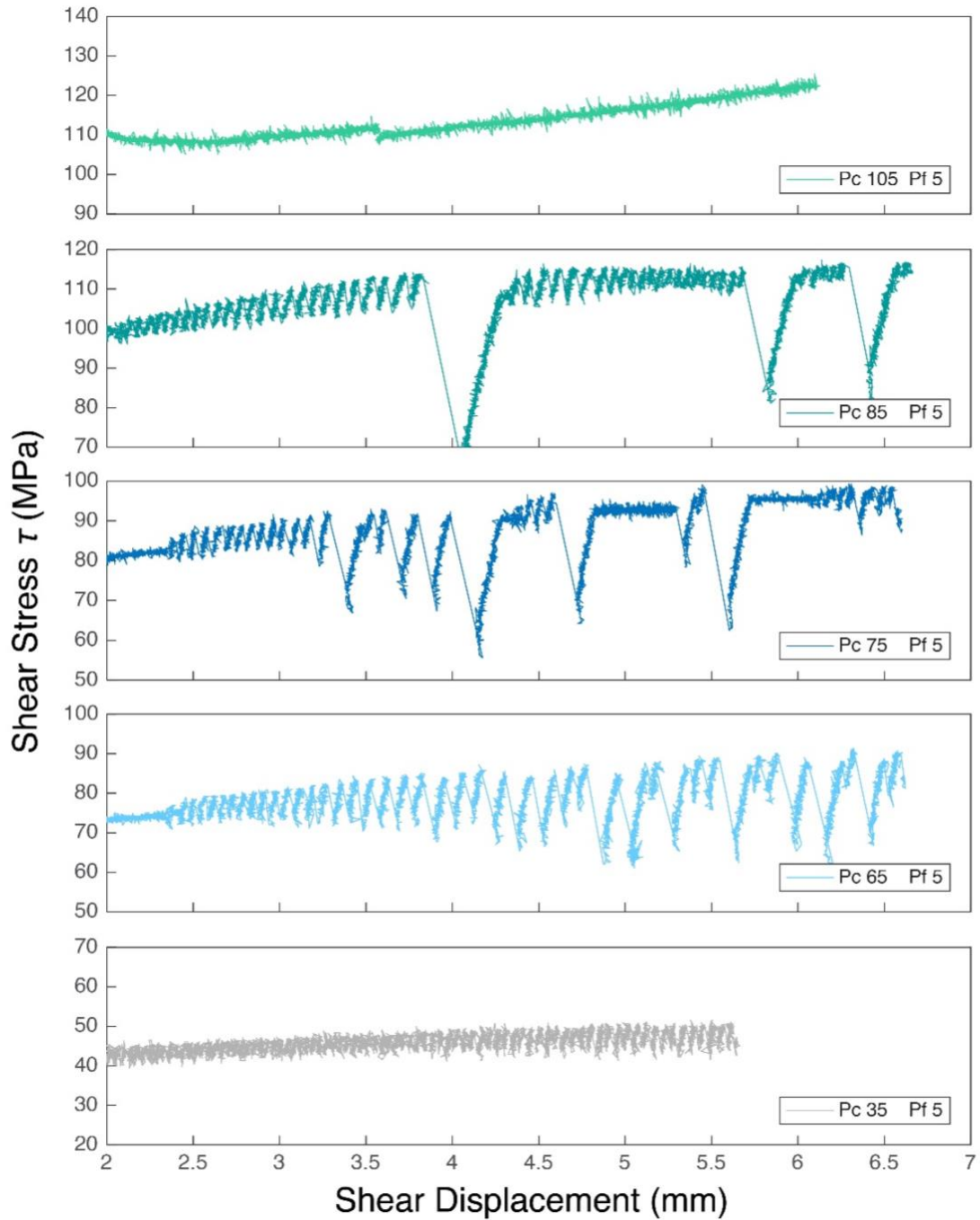


Figure 4.3: Effective pressure dependence of slip behavior. Amplitude of stress drops increases as effective pressure increases from 30 to 80 MPa. No slip is observed at 100 MPa effective pressure. All samples were deformed at a constant pore fluid pressure of 5 MPa.

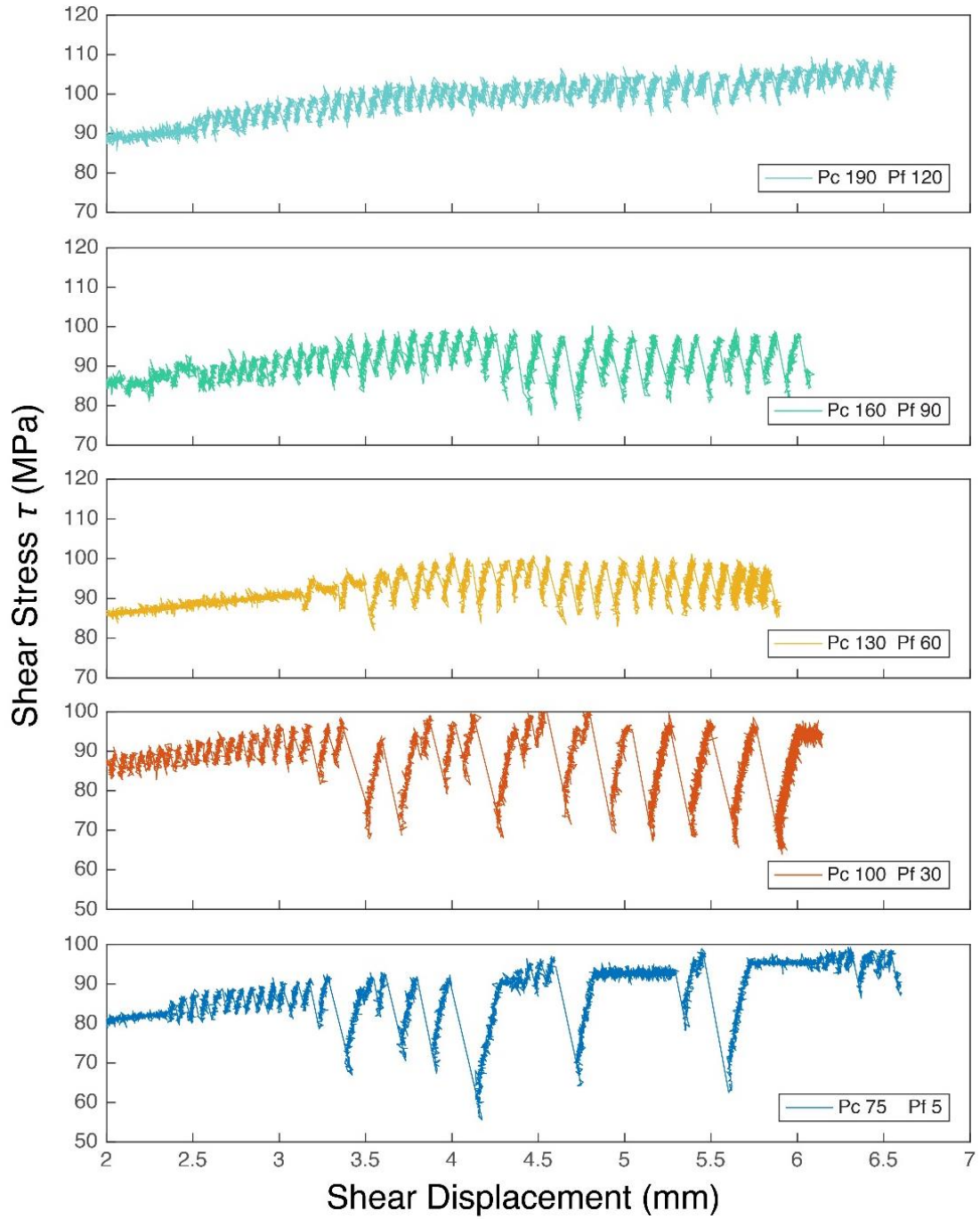


Figure 4.4: Pore fluid pressure dependence of stick-slip behavior. Amplitude of stress drops decreases as pore fluid pressure increases. All samples were deformed at a constant effective pressure of 70 MPa.

In our experiments, we have documented a spectrum of slip behaviors in associated with increasing effective pressure (Figure 4.3) and pore fluid pressure (Figure 4.4). Based on the amplitudes of stress perturbation, the slip events can be grouped into large amplitude events and small amplitude events.

At a low pore fluid pressure of 5 MPa, the EPS experiments show that amplitudes of stick-slip events correlated with effective pressure (Figure 4.3). At low effective pressure of 30 MPa, the slip events are all small amplitude events. The frequency of reoccurrence between similar amplitude slip events is relatively constant. As effective pressure increases, the slip events become irregular with various amplitudes of stress perturbations. Random large amplitude events are observed to occur between small amplitude events. At an effective pressure of 30 MPa, the slip events are quiet from the beginning and gradually become semi-audible as deformation continues. At 60 to 70 MPa effective pressure, the slip events are semi-audible to audible. As effective pressure increases to 80 MPa, the stick-slip events change to quiet and semi-audible again for all small slip events, while the large amplitude events are loud. At 100 MPa, no slip occurred on the saw-cut surface, and the experiment ended up with the creep deformation in the shearing blocks.

At an effective pressure of 70 MPa, the PPS experiments show that increasing pore fluid pressure impedes large amplitude events (Figure 4.4). At low pore fluid pressure (5 to 30 MPa) the slip events are irregular with various magnitudes of stress perturbations and random frequency of reoccurrence between similar amplitude events.

As pore fluid pressure increases, the stress drop evolves into relatively homogeneous, small amplitude events. The frequency of reoccurrence between similar amplitudes becomes constant. At pore fluid pressure of 5 MPa, the slip events are audible from the beginning. With increasing pore fluid pressure from 30 to 90 MPa, the slip events go through a transition from highly audible to less audible to silent. At high pore fluid pressure of 120 MPa, all slip events are semi-audible to silent.

4.3.2 Stress Drop and Stress Drop Durations

In each experiment, the shear stress drop ($\Delta\tau$) and stress drop duration (Δt) are measured for every observed stick-slip event and are summarized in Figure 4.5.

The EPS experiments show a trend of decreasing stress drop durations with increasing effective pressure. At low effective pressure, stress drops are small with long durations (Figure 4.5a). Increases in effective pressure lead to an increase in the amount of large stress drops with short durations. Indicating that the stress drops are becoming more abrupt as effective pressure increases. The observations also show that distributions of stress drop events widen as effective pressure increases. Large amplitude events with stress drops ranging from 25 to 55 MPa start to emerge as effective pressure increases. The largest stress drop observed is positively correlated with the effective pressure at constant pore fluid pressure conditions.

The PPS experiments show a trend where stress drop duration increases with increasing pore fluid pressure (Figure 4.5b). At low pore fluid pressure, stress drops are large with short durations. They evolve into small amplitude events with longer durations as pore fluid pressure increases. At low pore fluid pressure (5 to 30 MPa), the stick-slip events distribution expands in a wider range in terms of shear stress drop.

Observations show a cluster of slip events with stress drops ranges from 20 to 40 MPa. At high pore fluid pressure conditions, the stress drops are relatively homogeneous and are all centered around 10~15 MPa. The magnitude of the largest stress drop observed is negatively correlated with the pore fluid pressure at constant effective pressure conditions.

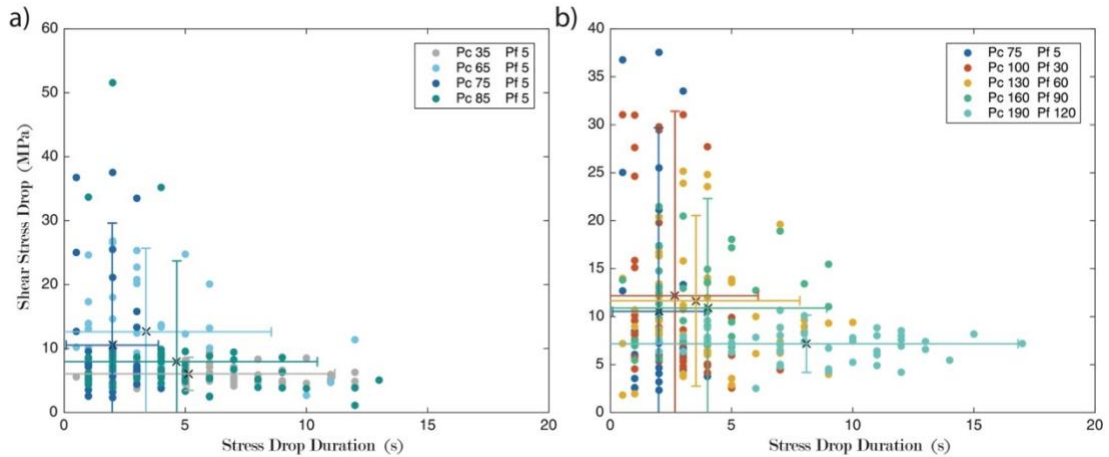


Figure 4.5: Magnitude vs. duration of shear stress drop for individual slip events a) under various confinements and a constant pore fluid pressure of 5MPa; b) under various pore fluid pressures and a constant effective confinement of 70MPa. The bars represent the $\pm 2\sigma$ standard deviation range of the distribution of stress drop (vertical) and stress drop duration (horizontal).

From the PPS experiments, period doubling is observed at pore fluid pressure of 60 to 90 MPa. During period doubling, small and large stress drops alternate, with larger events being semi-audible and smaller events being quiet (Scholz et al., 1972). The occurrence of period doubling has been interpreted to represent a transition towards stabilization in slip (Wong et al., 1992).

Measurement of the stress drop duration show that the large amplitude events are associated with abrupt large stress drops, while smaller amplitude events are slow and smaller stress drop events. This indicates that the small amplitude events may represent

the laboratory slow-slips while the large amplitude events could be the manifestation of dynamic slips.

4.3.3 Slip Distance and Elastic Energy

Measurements of stress drops and the amount of slip (Δs see Equation 4.1) during stick-slip events can help us calculate the elastic strain energy release (G) which describes the total amount of energy released during the stress drop (see Figure 4.6). The elastic energy release is a sum of the fracture energy (G_c) which describes the energy required for rupture and the radiated energy (G_r). We cannot decide the portion of fracture energy release during the slip event. Instead, the total energy release is calculated. The elastic energy release can be calculated using equation:

$$G = \frac{1}{2} \Delta \tau \cdot \Delta s \quad (4.2)$$

where $\Delta \tau$ is the shear stress drop during the slip events and Δs is the slip distance. The slip velocity v during each slip is defined as:

$$v = \frac{\Delta s}{\Delta t} \quad (4.3)$$

In this study, the shear displacement is calculated from the load-point displacement (d). During slip events, stress drop can lead to an axial relaxation of the system which is partly accommodated by the sample slip on the fault surface. Because we cannot decide the proportionality of the axial relaxation accommodated by the sample slip, the slip distance we discussed here is an apparent slip distance during dynamic slip events calculated based on the load-point displacement corrected with the elastic relaxation of the system during stress drops.

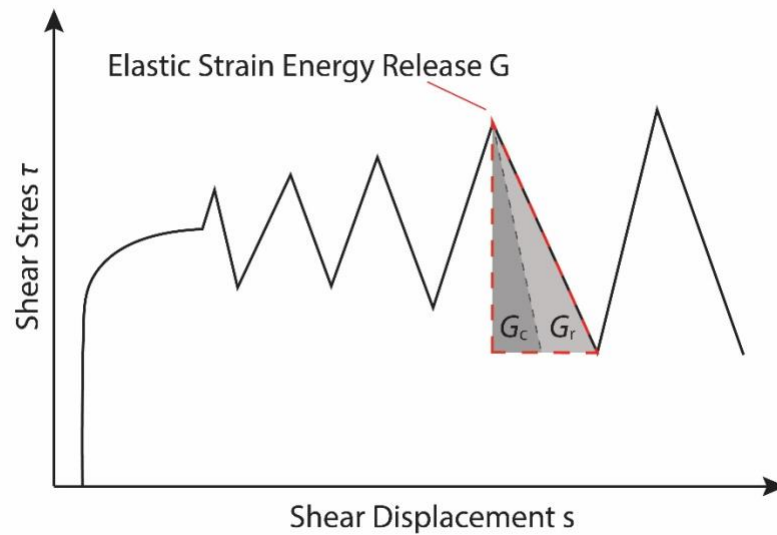


Figure 4.6: Elastic strain energy release calculation during individual slip events.

Elastic energy calculation for each individual stick-slip event is summarized in Figure 4.7. Analysis of the elastic energy shows that, at low effective pressure, the elastic energy release for each stick-slip event falls in a narrow range of distribution. The slip velocity also shows less variation. With increasing effective pressure, the elastic energy release significantly increases with a broader range of distribution. The slip also becomes faster during stress drops. The elastic energy release and slip velocity are also affected by the pore fluid pressure. At lower pore fluid pressure conditions, the elastic energy release varies and tend to have a larger range. The slip velocity also tends to be higher when the elastic energy release is high. When the pore fluid pressure is high, the elastic energy release significantly decreases. The events become smaller with slower slip velocity.

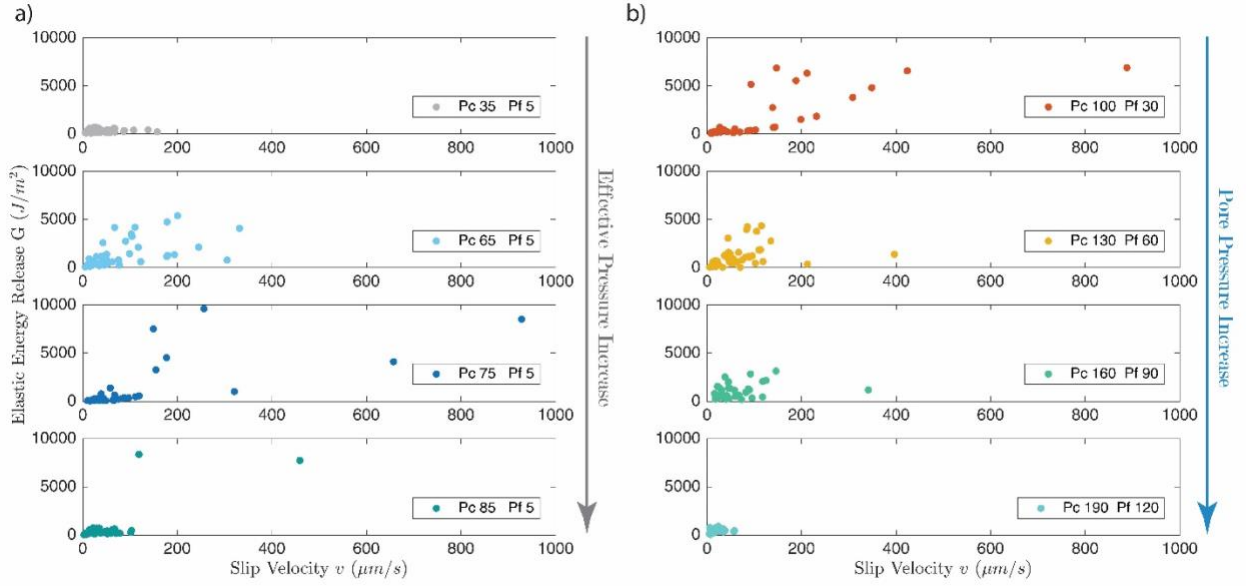


Figure 4.7: Elastic energy release vs. slip velocity for individual slip events. a) under various confinements and a constant pore fluid pressure of 5 MPa; b) under various pore fluid pressures and a constant effective confinement of 70 MPa. In general, increasing effective confinement broadens the range of elastic energy release and slip velocity, whereas increasing pore fluid pressure has an opposite effect.

4.3.4 Moment Magnitude

To better characterize the stick-slip behavior, estimations of earthquake magnitude are made using calculations of seismic moment (Aki, 1966) and moment magnitude (Hanks & Kanamori, 1979). The seismic moment (M_0) can be calculated using the followed equation:

$$M_0 = \mu A \cdot \Delta s \quad (4.4)$$

where μ is the shear moduli of the material; A is the area of fault that ruptures during the earthquake; and Δs is the slip distance on fault. In this study, the shear moduli of quartz has been used for the calculation of seismic moment (Pabst & Gregorová, 2013). The area of rupture is estimated using the saw-cut surface which is an ellipse with a major radius of 25.4 mm and minor radius of 12.7 mm. The off-set of overlapping area

due to accumulative shear has been estimated to lead to ~1% of variation in the results of the magnitude estimation. This is considered to have an insignificant effect on our analysis and is therefore ignored in our calculation. The slip distance is the shear displacement during stress drops calculated from the axial displacement. Corrections on the elastic relaxation are made to correct for the true slip distance during stress drops (see Appendix B).

The moment magnitude M_w can then be calculated based on the seismic moment:

$$M_w = \frac{2}{3} \log M_o - 6.06 \quad (4.5)$$

The distribution of the estimated magnitudes of all observed events are plotted in Figure 4.8. In this experiment, the largest theoretically possible slip is 25.4 mm which yields a moment magnitude of -2.13. The estimated magnitudes for all observed slip events are well below this threshold. The β -value term has been used to describe the Gutenberg-Richter frequency-magnitude relations for earthquakes (Gutenberg & Richter, 1956). The β -value is defined by equation:

$$\log N/N_0 = \alpha - \beta M_w \quad (4.6)$$

where N is the number of earthquakes with magnitude larger than a certain magnitude, N_0 is the total number of events observed, and α , β are constants.

Calculation of the Gutenberg-Richter β -value shows dependence on both effective pressure and pore fluid pressure (Figure 4.9). Calculation of β -value from EPS experiments also show that the β -value increases from ~1.5 to ~6.7 as effective pressure (P_e) decreases, indicating that the decrease in effective pressure stabilizes the stick-slip events and favors smaller magnitude events. In the PPS experiment, as pore fluid pressure (P_f) increases, the β -value increases from 1.3 to 11.2. The β -value evolution

shows that the slip events observed at high pore fluid pressure conditions are dominated by smaller magnitude events. Previous studies have related the high β -value with SSEs (Ito et al., 2009; Nakamura & Sunagawa, 2015). Calculation of the β -value from this study indicates that the events from low P_e experiments in EPS and high P_f experiments in PPS are the manifestation of laboratory SSEs. The changes of β -values are also consistent with our interpretation that the low P_e and high P_f could stabilize fault movement and lead to slow-slips.

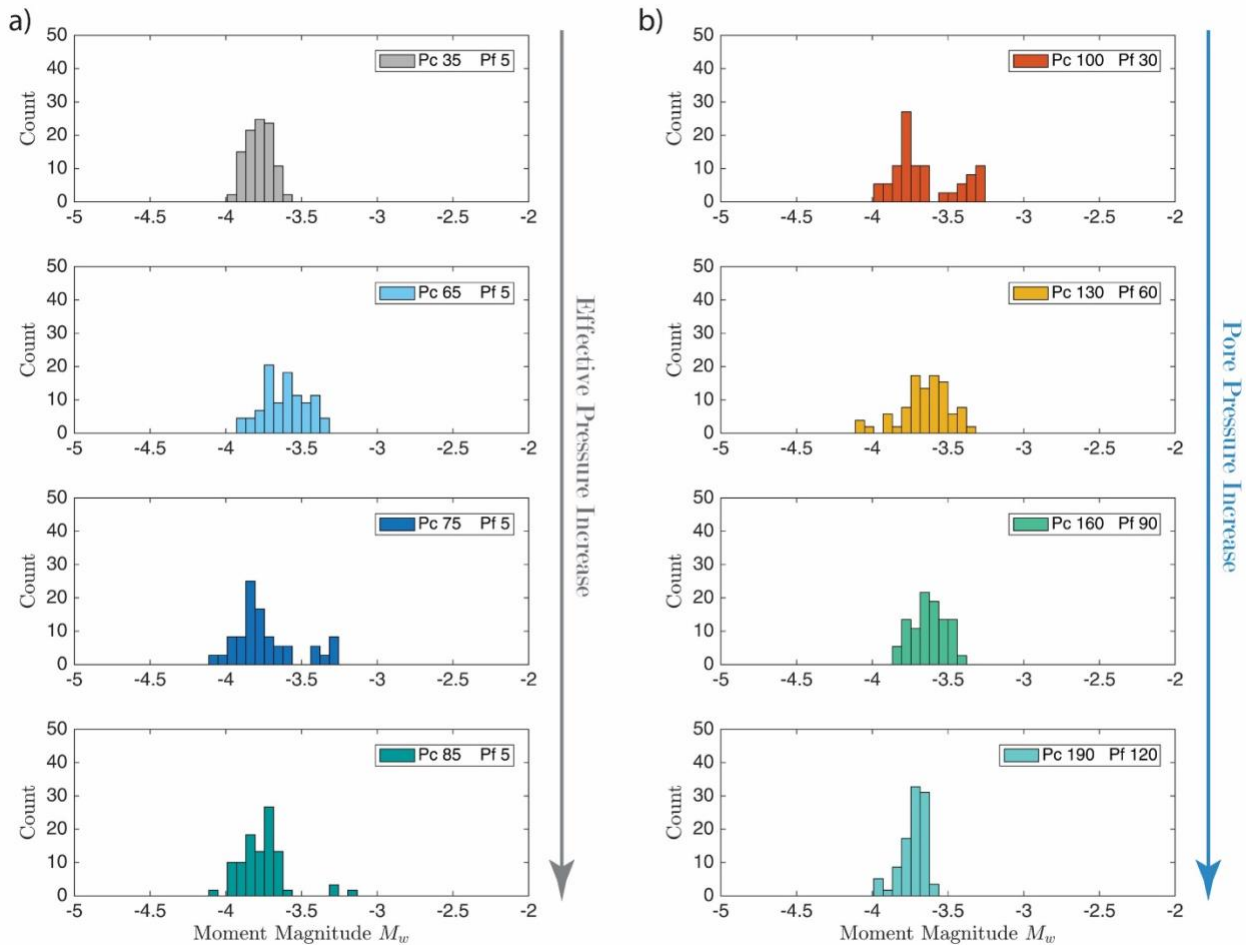


Figure 4.8: Histogram of moment magnitude distribution for individual slip events a) under various confinements and a constant pore fluid pressure of 5 MPa; b) under various pore fluid pressures and a constant effective confinement of 70 MPa. In general, increasing effective confinement or decreasing pore fluid pressure leads to a wider moment magnitude distribution.

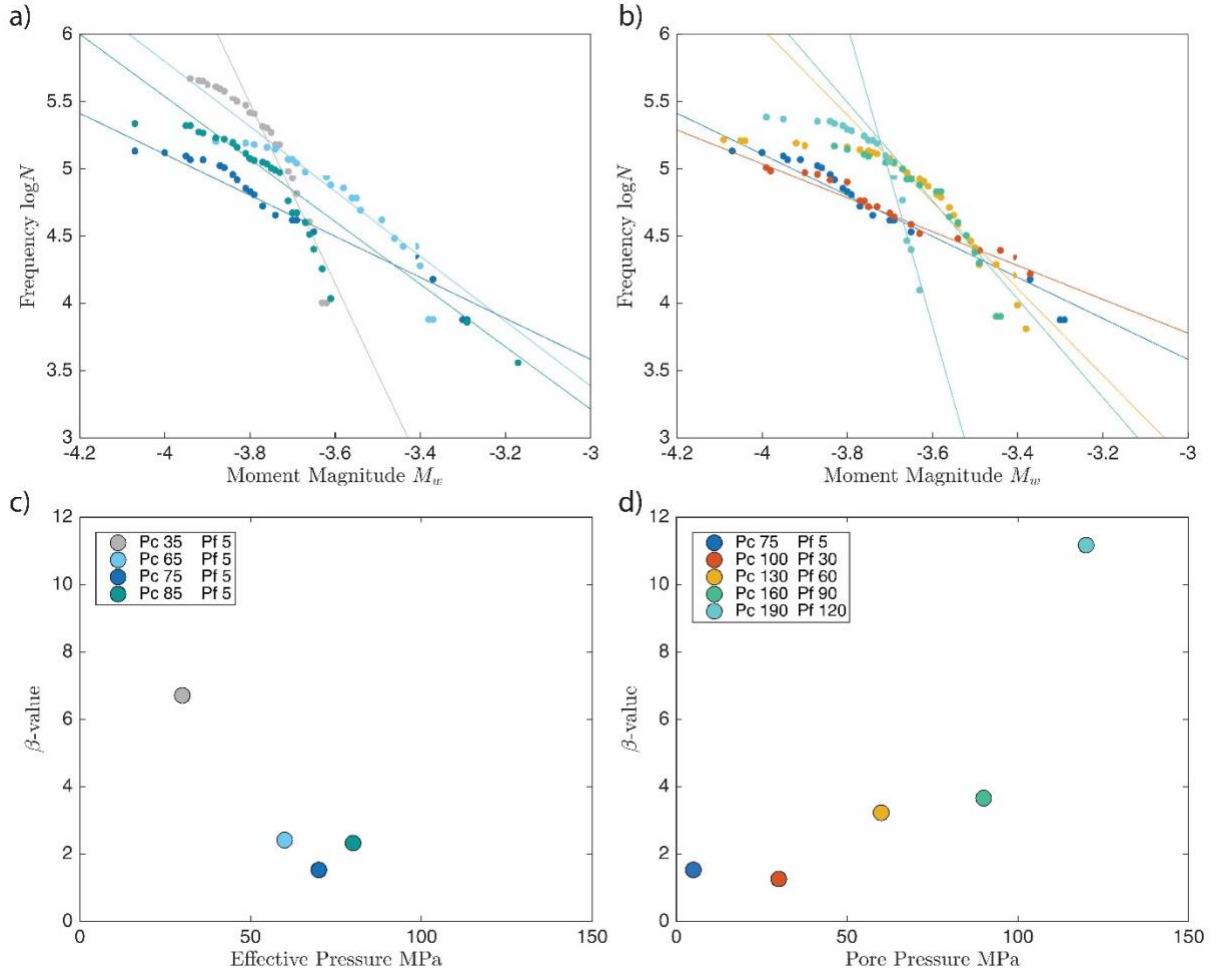


Figure 4.9: Frequency of moment magnitude for individual slip events a) under various confinements and a constant pore fluid pressure of 5 MPa; b) under various pore fluid pressures and a constant effective confinement of 70 MPa. Gutenberg-Richter β -values calculated from the slope of the fitted lines as a function of c) effective confinement; d) pore fluid pressure.

4.3.5 Effect of Slip Velocity on Slip Events

The stick-slip events also show a dependence on the slip velocity. At a pore fluid pressure of 5 MPa, the stick-slip events are not observed at axial displacement velocities lower than 0.5 $\mu\text{m/s}$. At 30 MPa pore fluid pressure, the stick-slip events are not observed at axial displacement velocities lower than 0.1 $\mu\text{m/s}$. At pore fluid pressure above 60 MPa, stick-slip events are observed at all tested displacement

velocities. A similar effect of loading conditions on the stick-slip behavior was observed in other studies (McClaskey & Yamashita, 2017). Our results may suggest that the velocity range for which stick-slip events occur can be affected by the pressure conditions. However, a systematic study using a wider range of slip velocity is required to better reveal the correlation between slip velocity and the occurrence of stick-slip.

4.4 Discussion

4.4.1 Pressure Dependence of Stick-slip Events

The results from our laboratory experiments demonstrate that variations in pressure conditions, including effective pressure and pore fluid pressure, could cause a spectrum of slip behaviors from more unstable seismic slip to slow-slip.

Increasing effective pressure results in a destabilization of fault slip. From the EPS experiments, it is observed that the stress drops are smaller with regular reoccurrence at low effective pressure. At high effective pressure, large dynamic events with irregular recurrence are observed. Analysis on the Gutenberg-Richter β -value shows that the dynamic slip represents the seismogenic slip while the smaller events are characterized as slow-slip. A similar effect of destabilization with increasing effective pressure is also observed in other experimental and numerical studies (e.g. Leeman et al., 2016; Reinen et al., 1991; Segall et al., 2010).

A trend of stabilizing fault slip is observed with increasing pore fluid pressure. From the PPS experiment, the stress drops are observed to be large and dynamic with irregular reoccurrence at low pore fluid pressure and small regular stress drops occurring at high pore fluid pressure.

A study of Wech and Creager (2011) has shown that with increasing depth, slip behavior exhibits a transition from large, less frequent to small, frequent slip activities. This is consistent with our experimental observations that the slip behavior changes from abrupt and irregular to slow and regular stress drops as pressure condition changes.

The pressure dependence of slip events is summarized in a conceptual model (Figure 4.10). Slow-slip is favored by low effective pressure or high pore fluid pressure. As effective pressure increases, stick-slip becomes more unstable and dynamic. With a further increase in effective pressure, stick-slip becomes prohibited and stabilizes again.

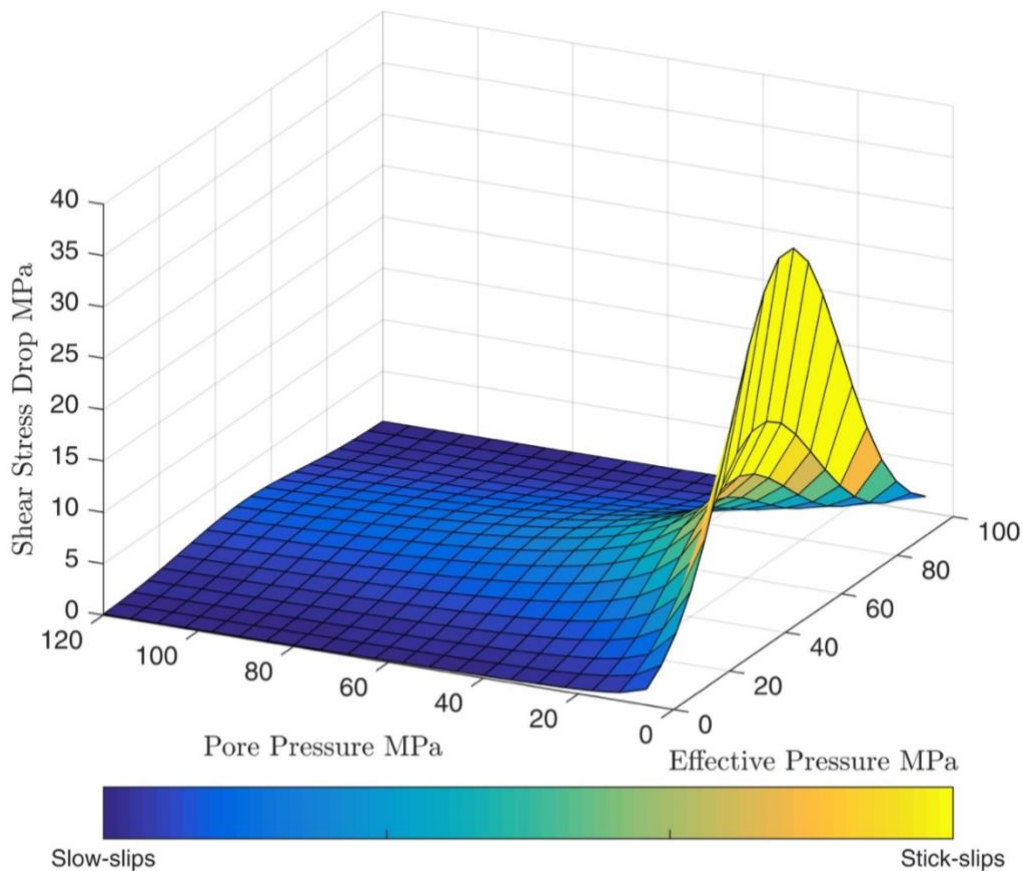


Figure 4.10: Magnitude of shear stress drop during slip events controlled by both effective confinement and pore fluid pressure.

4.4.2 Elastic Energy and Energy Release Rate

Calculation of the elastic energy release during stick-slip events shows that at low pore fluid pressure, the energy release during stick-slip events is fast with large energy release. At higher pore fluid pressure, both the magnitude of stress-drops and the energy release rate decrease significantly. The stress drop durations are also significantly increased with decreasing effective pressure.

The audibility of stress drops can also be a manifestation of the energy release. Large stress drops are associated with large elastic energy release and, therefore, louder sound effect. This is consistent with our observations that the low effective pressure experiments and high pore fluid pressure experiments are calculated to have low elastic energy release and tend to produce quiet to semi-audible SSEs. Observations on the audibility of stick-slip events are consistent with previous studies (Leeman et al., 2016), where audible events are associated with high slip velocity and large stress drops.

The audible events with large stress-drops represent dynamic instability. They can be interpreted as the laboratory observations of fast earthquakes (Brace & Byerlee, 1966). This demonstrated that decreasing effective pressure and increase in pore fluid pressure are both stabilizing the fault slip, causing smaller fault slip and slower energy release.

4.4.3 Slip Velocity during Slip Events

The slip velocity during slip events ranges from 10^{-6} to 10^{-3} m/s (Figure 4.11). The peak slip velocity of fast events may be higher due to a limitation of the instruments in this study. In general, the slip velocity measurements from this experiment are consistent with other reported laboratory studies (Passelègue et al., 2016; Tinti et al.,

2016). The velocity range from this study shows a transition between seismic events and SSEs.

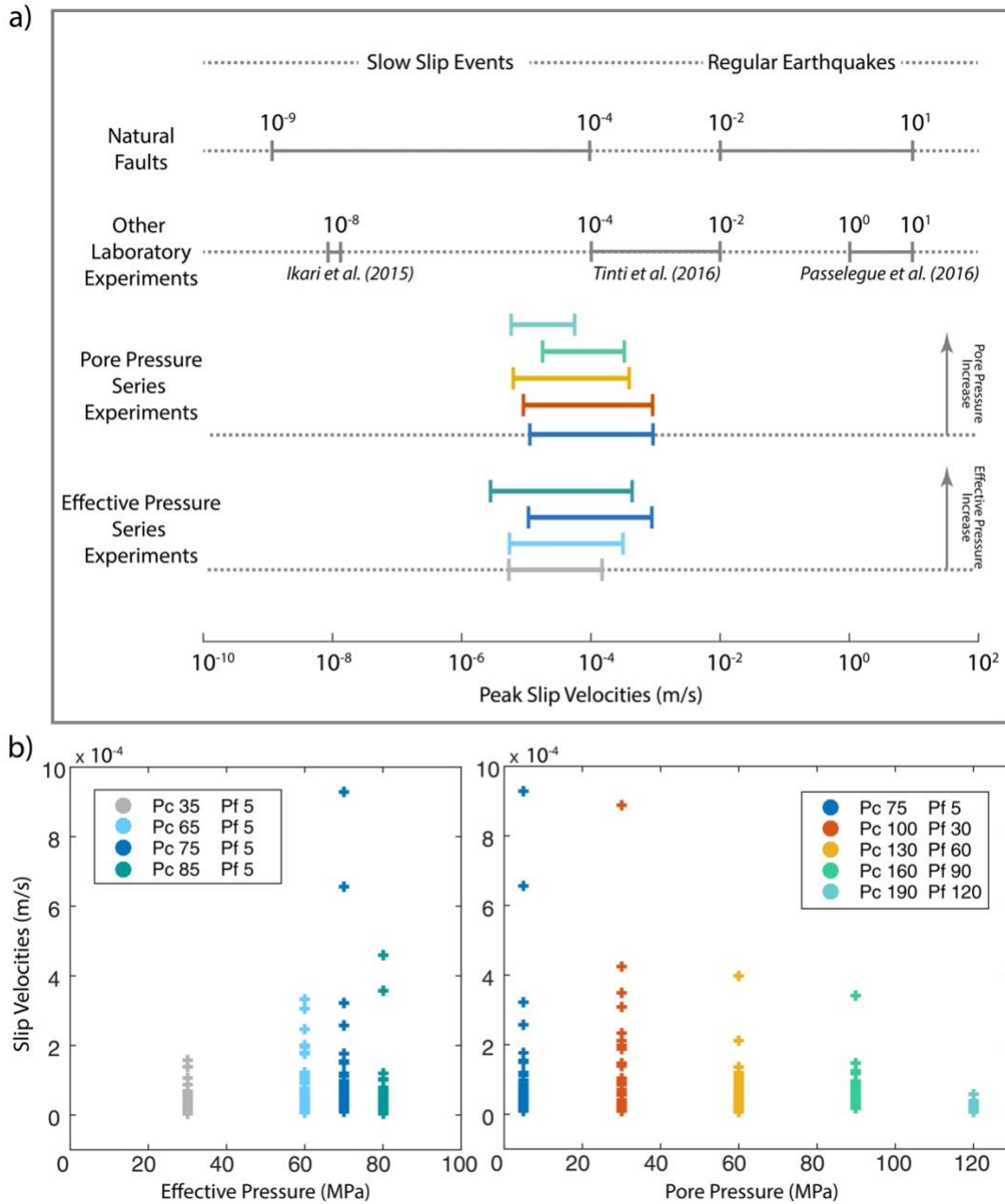


Figure 4.11: a) Slip velocity measurement of individual slip events with comparison to other laboratory studies. b) Pressure dependence of slip velocity.

The small amplitude events observed in this study show velocities that are consistent with slow-slips (Peng & Gomberg, 2010) while the fast, large amplitude events are manifestation of dynamic, seismic events.

The slip velocities also show pressure dependence as decreasing effective pressure and increasing pore fluid pressure tend to reduce the dynamic events and favor small amplitude events. This implies that low effective pressure and high pore fluid pressure would favor the occurrence of SSEs.

4.4.4 Spectrum of Fault Slip Behavior

Ruina (1983) has described change in fault slip behavior as a result of the change in the critical stiffness (k_c) of the material comparing to the stiffness of the surroundings (k) using the following equation:

$$k_c = \frac{-(a-b)\sigma_n}{D_c} \quad (4.7)$$

where both $(a-b)$ and D_c are frictional parameters (Dieterich, 1979; Gu et al., 1984; Marone, 1998; Ruina, 1983), and σ_n is the effective normal stress applied on the surface. When $k_c > k$, the stress drops tend to be irregular, while the stress drops are regular when k_c becomes close to k (Gu et al., 1984; Rice & Ruina, 1983). The stiffness model ascribes the changes in slip behaviors to the changes in friction parameters $(a-b)$, characteristic displacement D_c and the effective normal stress σ_n .

The results from this study support the idea that fault slip behavior can be affected by the variation in pressure conditions which also affect the friction parameters. These variations can result in a spectrum of fault slip behavior (Ikari et al., 2013; Kitajima & Saffer, 2012; Leeman et al., 2016). By increasing pore fluid pressure or decreasing

effective pressure, the fault slip behavior can change from unstable seismic slip with larger irregular stress drops to transitional slow slip with small regular stress drops. This transition represents a decrease in the critical stiffness.

The effect of pressure on the rate-and-state friction parameters has been investigated in several studies (e.g. Niemeijer & Collettini, 2013; Scuderi & Collettini, 2016). Previous friction experiments have found that high pore fluid pressure could lead to an increase in friction parameters ($a-b$) and the characteristic displacement (D_c) due to the dilatant hardening mechanism (Chapter 3). This could result in a reduction in the critical stiffness and therefore favor stabilization of fault slip. This is supported by the observation from our studies where high pore fluid pressure stabilizes fault slip. The effective pressure would cause an increase in both σ_n and ($a-b$), and therefore increases the critical stiffness and destabilizes fault slip. As effective pressure increases further, ($a-b$) becomes positive and only aseismic slip can occur (Dieterich, 1979; Ruina, 1983).

Figure 4.12 shows a conceptual fault slip model of the subduction zone combining previous geophysical observations with the experimental results from this study. At shallow depth, the pore fluid pressure is relatively low and remains mostly hydrostatic. The effective pressure is the dominant control on slip behavior at these depths. An increase in effective pressure causes unstable slip to emerge with increasing depth. Local variations in pore fluid pressure due to impermeable layers could cause transitional slip behavior to occur at shallow depth. At deeper depth, fluids are released by dehydration reactions, decrease in the permeability due to chemical precipitation and inelastic deformation could preclude fluid migration and cause the pore fluid

pressure to increase to near-lithostatic level (e.g. Walder & Nur, 1984; Zoback & Townend, 2001). At this depth, pore fluid pressure becomes the primary controlling factor on the slip behavior. An increase in the pore fluid pressure stabilizes fault slip and causes the transition from unstable slip to slow-slips. At even deeper depth, both effective pressure and pore fluid pressure increase to a high level. Only aseismic stable slip can occur at such conditions.

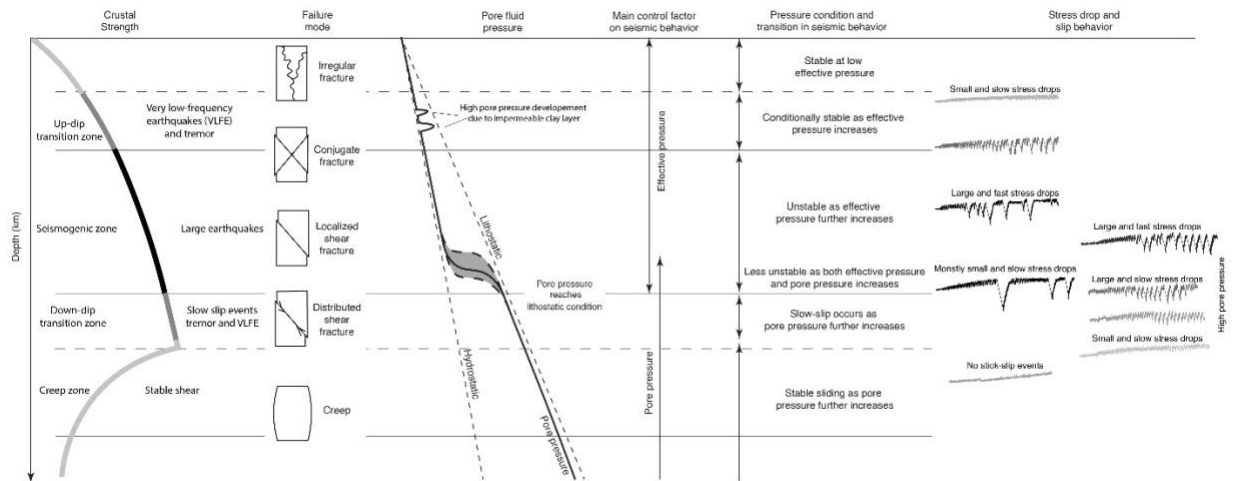


Figure 4.12: Synoptic fault slip model of a subduction zone. The observed spectrum of slip behaviors is the result of an interplay between effective pressure and pore fluid pressure.

4.5 Conclusion

The results from our study have demonstrated that:

- Variations in pore fluid pressure (P_f) and effective pressure (P_e) can lead to a transition in stick-slip behavior from unstable seismic slip to slow-slip and aseismic slip;
- The spectrum of stick-slip behaviors observed in this study is a result of the effect of pressure conditions on the critical stiffness of the deforming material;

- An increase in effective pressure tends to increase the critical stiffness and enhance stick-slip until a threshold is met where stick-slip events are prohibited, and creep takes place;
- Higher pore fluid pressure tends to decrease the critical stiffness and leads to slow slips and transitional slip behaviors.

Our experimental results support the hypothesis that the transition between stick-slip and slow-slip can be achieved on a seismogenic fault by varying the pressure conditions. The pore fluid pressure (P_f) and effective pressure (P_e) are functioning as two pressure dials that can tune the slip events. Specifically, a decrease in effective pressure or an increase in pore fluid pressure could both cause a transition of slip behavior from unstable, seismogenic stick-slip to relatively stable slow-slips. Our observations further support the idea that unstable earthquakes and slow-slip events could arise from the same mechanism. The results imply that the pore fluid pressure build-up could cause the stick-slip event to change from earthquake-generating unstable slip to slow slip. Our study illuminates the correlation between the occurrence of SSEs and presence of high pore fluid pressure and provide insights to the dynamics of subduction zones.

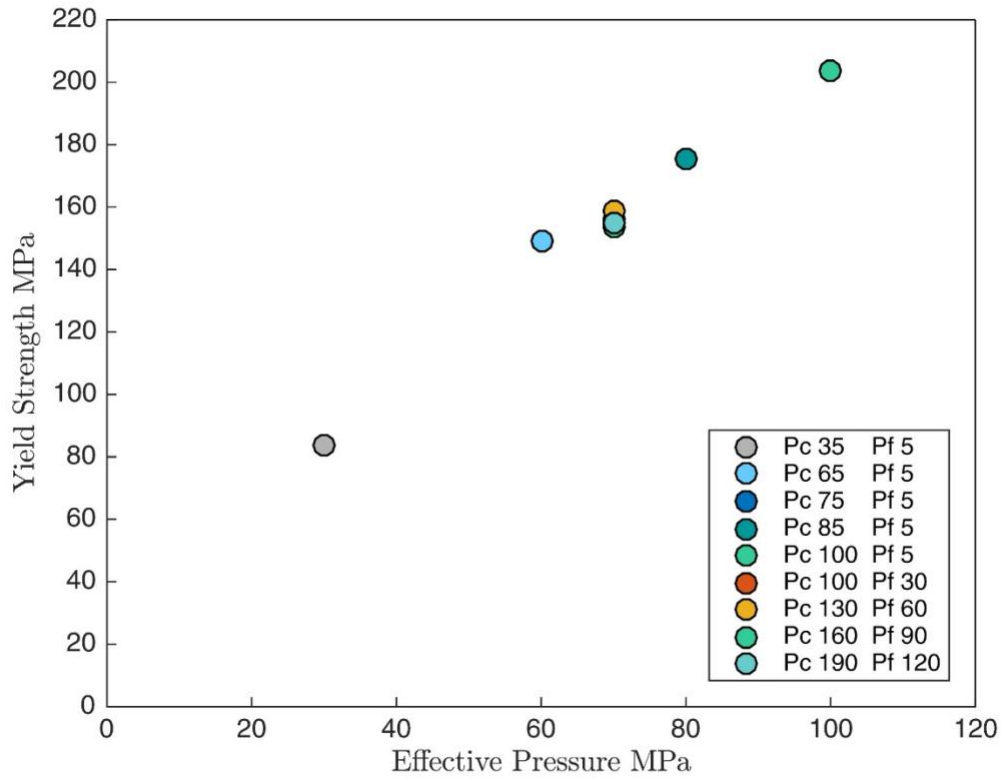


Figure 4.13: Yield strength of samples as a function of effective confinement ($P_e = P_c - P_f$)

Chapter 5: Role of Pore Fluid Pressure on Faulting Stability in Various Crystalline Rocks

Abstract

Interstitial fluid pressure exerts an important control on rock deformation throughout the lithosphere. Experiments in Chapter 3 show that the frictional slip along a gouge-bearing fault can change from velocity weakening to velocity strengthening as pore fluid pressures increase, and the strengthening effect varies with different mineral compositions. This raises the question whether the strengthening effect of high pore fluid pressure on fault propagation differ in different types of rocks. In this study, we conducted tri-axial deformation experiments on low permeability intact dunite, harzburgite and granite to investigate the effect of high pore fluid pressure on fault propagation in different rock types. Our results show that high pore fluid pressure impedes fault propagation in all rocks tested. The style of stabilization varies in different types of rocks. In granite samples, the stabilization mainly manifests in increasing the duration of fault nucleation, whereas the rates and magnitudes of the main faulting events remain similar. In contrast, ultramafic rocks (dunite and harzburgite) deformed at high pore fluid pressures not only have much longer durations of fault propagation, the magnitudes and rates of stress drop are also significantly reduced. Microstructural observations show that the microcracks in post-failure granite samples are predominantly mode-I, whereas few mode-I cracks are observed in deformed ultramafic rocks. This is in good agreement with the amount of dilation recorded during deformation. The strengthening effect can be explained by the dilatant

hardening model. The results shed light on the effect of pore fluid pressure in stabilizing fault slip in different rock types and provides insights into the occurrence of transitional fault slip behavior in a variety of crustal regions.

5.1 Introduction

Knowledge of the brittle deformation of rocks is important for understanding the geological process active in the lithosphere. The mechanical strength and deformation behavior of rocks also exerts critical controls over the seismicity along plate boundaries (Audet & Schaeffer, 2018; Kodaira et al., 2004; Shelly, 2010). The structure and composition of the lithosphere is also very complex. Oceanic plates are largely composed of peridotite, including dunite, harzburgite, etc. In a simple model, the oceanic lithosphere can be regarded as basaltic rocks overlying depleted mantle peridotite (Druiventak et al., 2011). The continental crust is largely composed of felsic rocks including granite (Rudnick & Gao, 2013). Within the crust, the interstitial fluid is also commonly present and interacts with rock, having a significant effect on rock deformation processes (Makhnenko & Labuz, 2015; Rice & Cleary, 1976; Rutter, 1972, 1974). Therefore, to obtain a comprehensive view of lithospheric deformation, experimental studies on the effect of pore fluid on the deformation of various rock types are required.

The mechanical effect of pore fluid pressure on the brittle failure of a rock is commonly discussed in the framework of the effective pressure law (Terzaghi, 1943):

$$P_e = P_c - P_f \quad (5.1)$$

where P_c is the confining pressure and P_f is the pore fluid pressure. An increase in pore fluid pressure leads to a reduction of effective pressure (P_e) and consequently lowers

the stress required for the brittle failure (Sibson, 1973). The effect of pore fluid pressure on deformation behavior by changing effective pressure has been investigated in many numerical and experimental studies (Helmons et al., 2016; Hubbert & Rubey, 1959; Ougier-Simonin & Zhu, 2015; Rutter & Hackston, 2017).

Recent studies show that the deformation behavior can also be affected by the absolute level of pore fluid pressure under the same effective pressure conditions. French and Zhu (2017) found that, under constant effective pressure, the duration of failure in intact serpentinites increases monotonically with increasing pore fluid pressure. The faulting changes from rapid and audible at low pore fluid pressure to slow and quiet at high pore fluid pressure. Studies related this slow faulting associated with increasing pore fluid pressure to the dilatant hardening mechanism (French & Zhu, 2017; Rice, 1975). Microcracks during brittle deformation cause dilation of the pore space which leads to a transient decrease in the pore fluid pressure and increases the local effective pressure, therefore, strengthening the faulting (Brace & Bombolakis, 1963; Rudnicki, 1984).

A similar stabilization effect associated with dilatant hardening on frictional sliding has also been discovered (Rudnicki & Chen, 1988; Samuelson et al., 2009). The Chapter 3 showed that, although strengthening effects on frictional deformation have been observed with increasing pore fluid pressure, different extents of strengthening have also been found with larger effects observed in serpentine and olivine comparing to quartz. This suggests that the high pore fluid pressure strengthening is composition dependent. However, it is still unclear what is responsible for the mechanism that causes the effect of strengthening to be composition dependent. Whether the dilatant

hardening would affect just the fault propagation or if it also affects deformation prior to faulting (i.e., fault nucleation) also remains to be tested through experimental studies.

Although earthquakes have been assumed to occur on pre-existing faults in theoretical modeling (Scholz, 1998), it is not well known to what percentage the earthquakes occur on faults or whether fracture would occur on locked regions with strength near that of the intact rocks (Lockner & Beeler, 2002). Therefore, experiments on intact rock fracturing can help further understand earthquake mechanisms. A study of the effect of brittle faulting at high pore fluid pressure conditions may also help illuminate the existence of transitional slip behaviors including slow-slips and tremors (Ito & Obara, 2006; Obara, 2002; Shelly, 2010).

In this study, we conducted tri-axial deformation experiments on intact dunite, harzburgite and granite, which cover a range of rock types occurring in the continental and oceanic lithosphere. The purpose of this study is to investigate the effect of fluid pressure on the deformation of peridotite and granite to better understand crustal deformation. The goal is to investigate whether the fault propagation in different types of rocks responds differently to high pore fluid pressures, and if so, what are the mechanisms responsible. Results from this study can help further understand the dynamics of fault propagation. They can also provide insights into the observed links between high pore fluid pressures and slow slips in various crustal regions.

5.2 Sample Configuration and Experimental Procedures

Samples used in this study include dunite and harzburgite from the Samail ophiolite, Oman, obtained by International Continental Scientific Drilling Program, Oman Drilling Project. For comparison, samples of Twin Sisters dunite from Washington,

and Westerly granite from Rhode Island are also studied. The Oman dunite and harzburgite are highly serpentinized. The Twin Sisters dunite is relatively unaltered with a high component of olivine. The Westerly granite is composed of quartz, feldspar and minor biotite. All samples are 18.4 mm in diameter. Sample length is 38.1 mm for granite and 43.8 mm for all other rock types. The sample is jacketed using copper foil with thickness of ~0.05 mm and joined with spacers and steel end-caps using 2 layers of polyolefin tubes. The top spacer and end-cap have a concentric hole which allows fluid access throughout the experiment (see Figure 5.1).

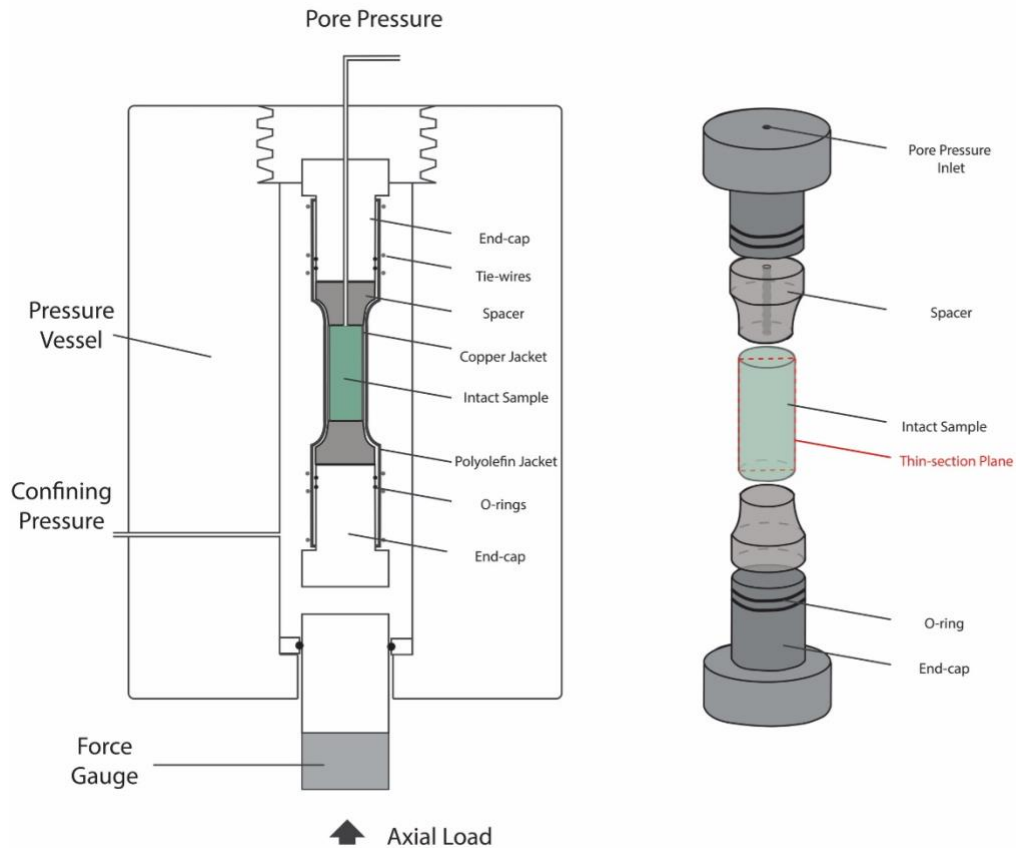


Figure 5.1: Experimental setup. The confinement (P_c), axial load (σ_1) and pore fluid pressure (P_f) are controlled independently using external intensifiers.

All experiments are conducted at 10 MPa effective pressure ($P_e = P_c - P_f$) with pore fluid pressures ranging from 10 MPa to 120 MPa. Detailed experimental conditions are

listed in Table 5.1. The samples are deformed under tri-axial stress conditions, where the maximum principal stresses (σ_1) is along the axial direction and the intermediate principal stress (σ_2) and minimum principle stress (σ_3) are along the radial directions of the sample. The σ_2 and σ_3 are controlled by the confinement pressure i.e. $\sigma_2 = \sigma_3 = P_c$. An external force gauge is mounted on the piston outside the vessel from which the axial load (σ_1) is measured. The differential stress ($\Delta\sigma = \sigma_1 - \sigma_3$) is calculated from the force gauge reading. Axial displacement on the sample is calculated using a linear variable differential transformer (LVDT) affixed to the axial piston. Strain on the sample, including axial strain (ϵ_a) and radial strain (ϵ_r) are measured using strain gauges affixed to the copper jacket around the sample. The volumetric strain (ϵ_v) is calculated from the axial and radial strain measurements ($\epsilon_v = \epsilon_a + 2\epsilon_r$).

Samples are saturated in deionized water under vacuum for 2 days and then under atmospheric pressure for a month prior to the experiment. Before starting the deformation, the sample is brought to 20 MPa confining pressure and 10 MPa pore fluid pressure to purge out bubbles in the pore system. Then both confining pressure and pore fluid pressure are increased at a rate of 2 MPa/min while keeping the effective pressure ~ 10 MPa until the experimental condition is reached. Then the sample is left at the condition for 6 hours to allow pore fluid pressure to equilibrate after which the deformation is conducted. Deformation is conducted at a displacement rate of 0.1 $\mu\text{m/s}$ which correspond to a strain rate of $\sim 2.6 \times 10^{-6} \text{ s}^{-1}$ for granite samples and $\sim 2.3 \times 10^{-6} \text{ s}^{-1}$ for dunite and harzburgite samples.

After the deformation, samples are impregnated with epoxy and are cut perpendicular to the fracture plane and parallel to the maximum principle stress

direction (see Figure 5.1). Thin sections are made along the cut surface and are used for microstructure analysis.

Sample	Length (mm)	P_c	P_t	$P_c - P_t$	Young's Modulus (GPa)	Poisson's Ratio	Peak Stress (MPa)	Residual Strength (MPa)	Total Fault Propagation Duration (s)	Fault Nucleation Duration (s)	Fault Angle
OD_120	43.8	130	120	10	18.6		190	140	1706	1154	20
OD_60	43.8	70	60	10	16.0	0.32	134	60	1307	578	30
OD_20	43.8	30	20	10	17.5	0.19	160	100	532	277	25
OD_10	43.8	20	10	10	11.7	0.19	100	30	288	31	40
OH_120	43.8	130	120	10	18.9		150	70	2225	816	25
OH_60	43.8	70	60	10	20.4	0.43	202	93	575	89	15
OH_10	43.8	20	10	10	19.0		189	93	278	46	20
TSD_120	43.8	130	120	10	35.0		398	328	1637	836	30
TSD_60	43.8	70	60	10	21.5		111	89	1008	364	30
TSD_10	43.8	20	10	10	29.9		231	159	166	74	25
WG_120	38.1	130	120	10	29.0	0.36	322	47	1826	1297	24
WG_10	38.1	20	10	10	29.5	0.34	319	52	218	149	21

Table 5.1: Experimental conditions of all tests (OD: Oman dunite; OH: Oman harzburgite; TSD: Twin Sisters dunite; WG: Westerly granite).

5.3 Results

5.3.1 Mechanical Strength

The mechanical data of all deformation tests are presented in Figure 5.2. Here, the axial strain is calculated from the axial displacement. All stress-strain curves show non-linear trend for the first 0.5% axial strain, indicating the initial crack closure. This is then followed by a linear portion which indicates linear elastic deformation of the sample until the onset of dilatancy.

The two types of dunite and the harzburgite show large variations in peak stress in tests. Experiments on Westerly granite show consistent peak stress and show ~1% variation. The peak stress variation does not show correlation with increasing confining pressure and are likely resulted from natural sample variations. The Young's modulus calculation on samples of the same rock type are consistent. Where strain data is available, the Poisson's ratio (ν) is calculated using the following equation:

$$\nu = -\frac{\Delta\epsilon_r}{\Delta\epsilon_a} \quad (5.2)$$

Calculation of the Poisson's ratio also show consistency among similar samples. The Oman harzburgite shows the highest Poisson's ratio compared to dunite and granite. The Poisson's ratio obtained from this study is consistent with previous measurement from similar rock types (e.g., Rao & Raman, 1974).

Available strain gauge data show that the stress-strain relationship is also consistent for the same rock type (Figure 5.3, 5.8 and 5.9). Compressive stresses and compactive strains are positive, following the geological convention. Strain gauges may be compromised by the localized fracture at the end of the experiment. Therefore, the

strain after the point of failure does not necessarily indicate dilation or compaction. In the Westerly granite, on-set of dilatancy is observed starting from 62% of the peak stress. However, the Oman dunite sample shows a lack of dilatancy prior to faulting from the strain gauge data.

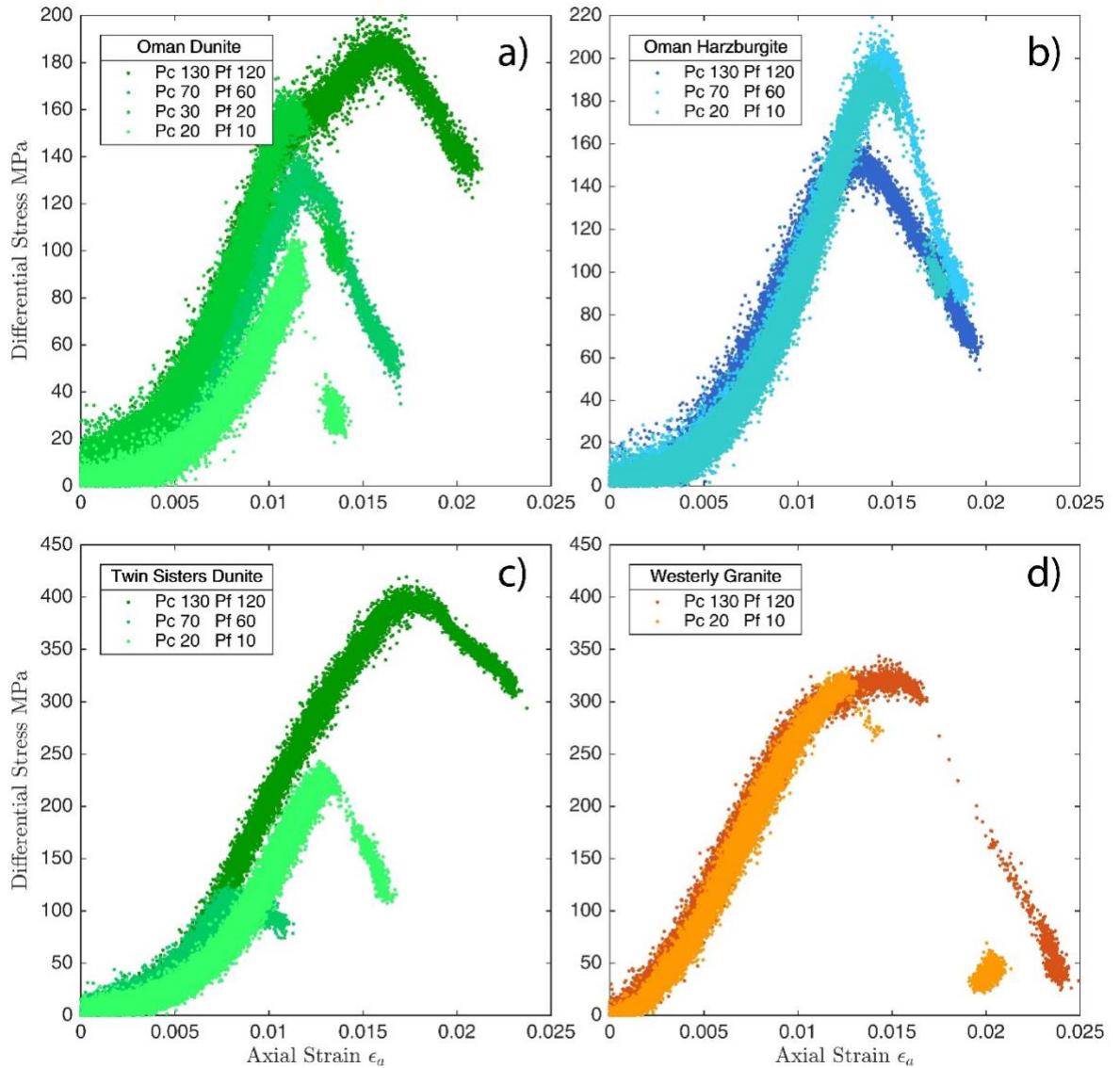


Figure 5.2: Plot of differential stress against axial strain. Mechanical data of a) Oman dunite; b) Oman harzburgite; c) Twin Sisters dunite; d) Westerly granite deformed at constant effective pressure of 10 MPa and pore fluid pressures ranging from 10 to 120 MPa.

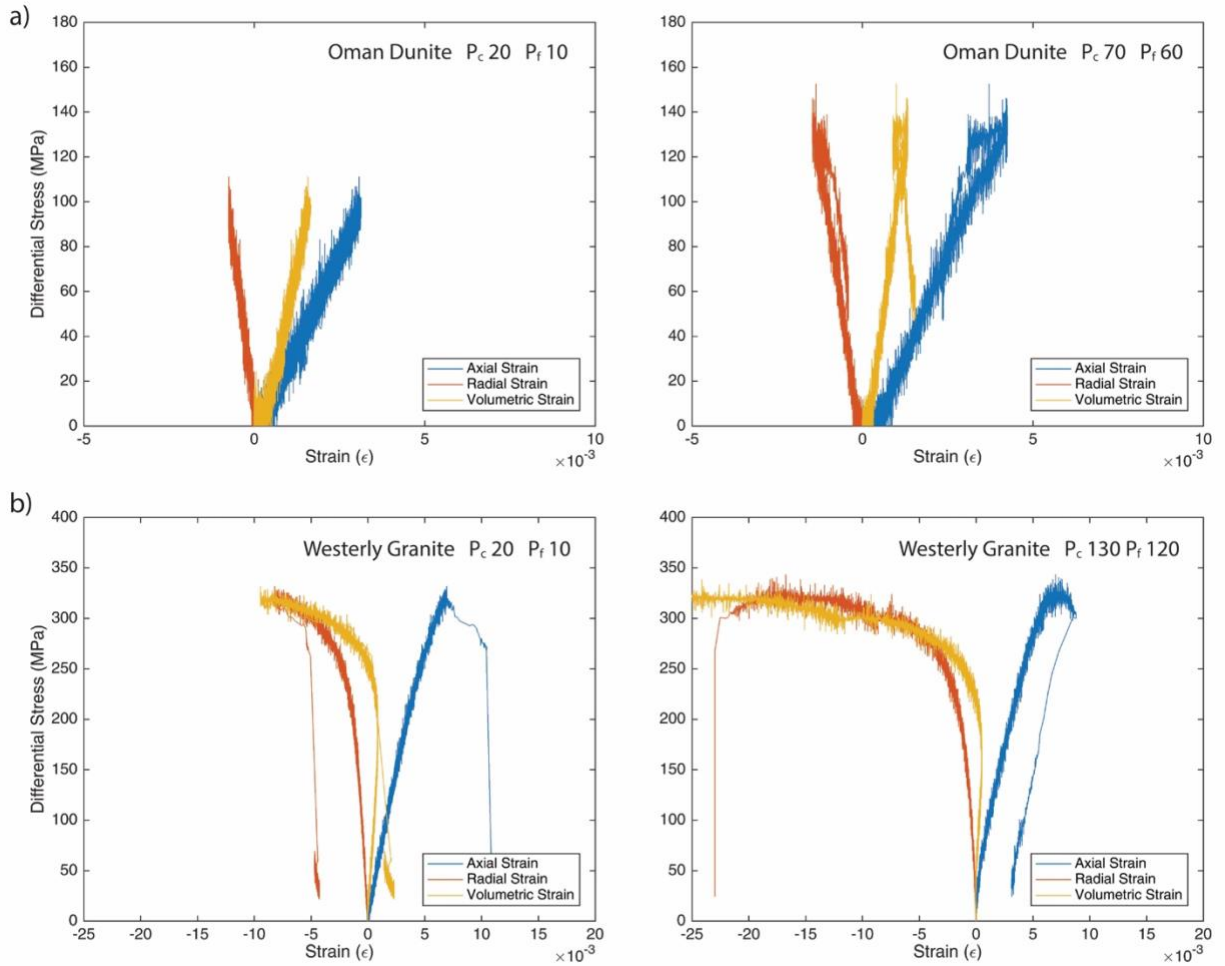


Figure 5.3: Strain data of a) Oman dunite and b) Westerly granite samples deformed at an effective pressure of 10 MPa. Pore fluid pressure conditions vary from 10 to 120 MPa.

5.3.2 Fault Nucleation and Propagation

Figure 5.4 shows the post peak deformation of all tested samples. The peak stresses are offset to 0 for a comparison of different samples. The peak stress of sample shows large variation. Magnitudes of stress drops are generally consistent.

Immediately after the peak stress, all samples show strain softening before a sudden stress drop, i.e., fault propagation (Figure 5.4). The nucleation and propagation process was illuminated by (Lockner et al., 1992). At low pore pressures, the period after the peak stress but before the sudden stress drop lasts a few 10s of seconds in all samples.

At high pore fluid pressures, this period reaches a typical 1,000-2,000 seconds, a two orders of magnitude increase (Figure 5.4).

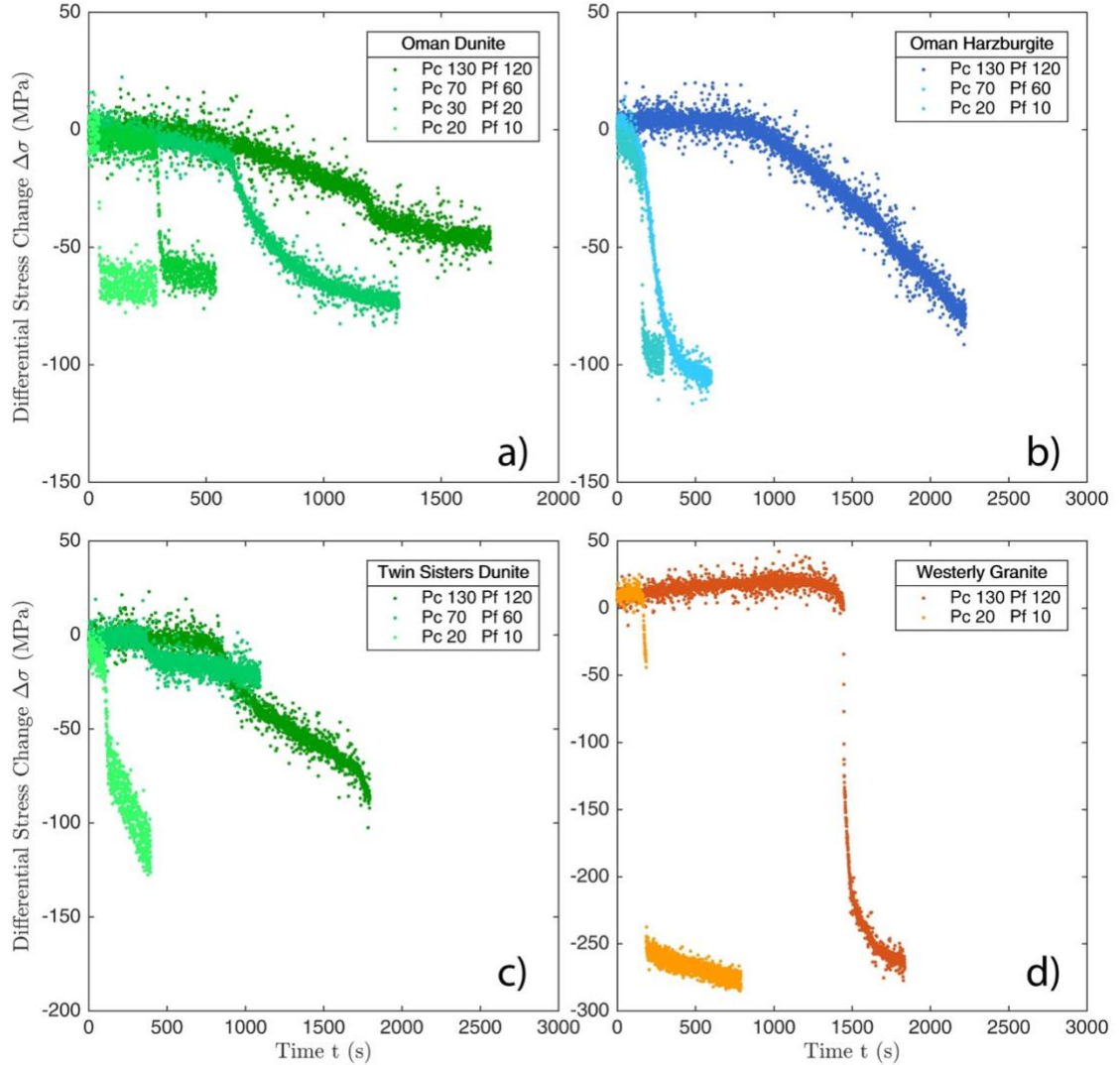


Figure 5.4: Stress drop during fracture propagation for a) Oman dunite; b) Oman harzburgite; c) Twin Sisters dunite; d) Westerly granite deformed at an effective pressure of 10MPa and various pore fluid pressures.

The duration of fault nucleation and propagation is measured as the time lapse from when peak stress is achieved until stress drop is complete (see Table 5.1 and Figure

5.5). We observed that the duration of fault nucleation and propagation is positively correlated with the pore fluid pressure when the effective pressure is kept constant.

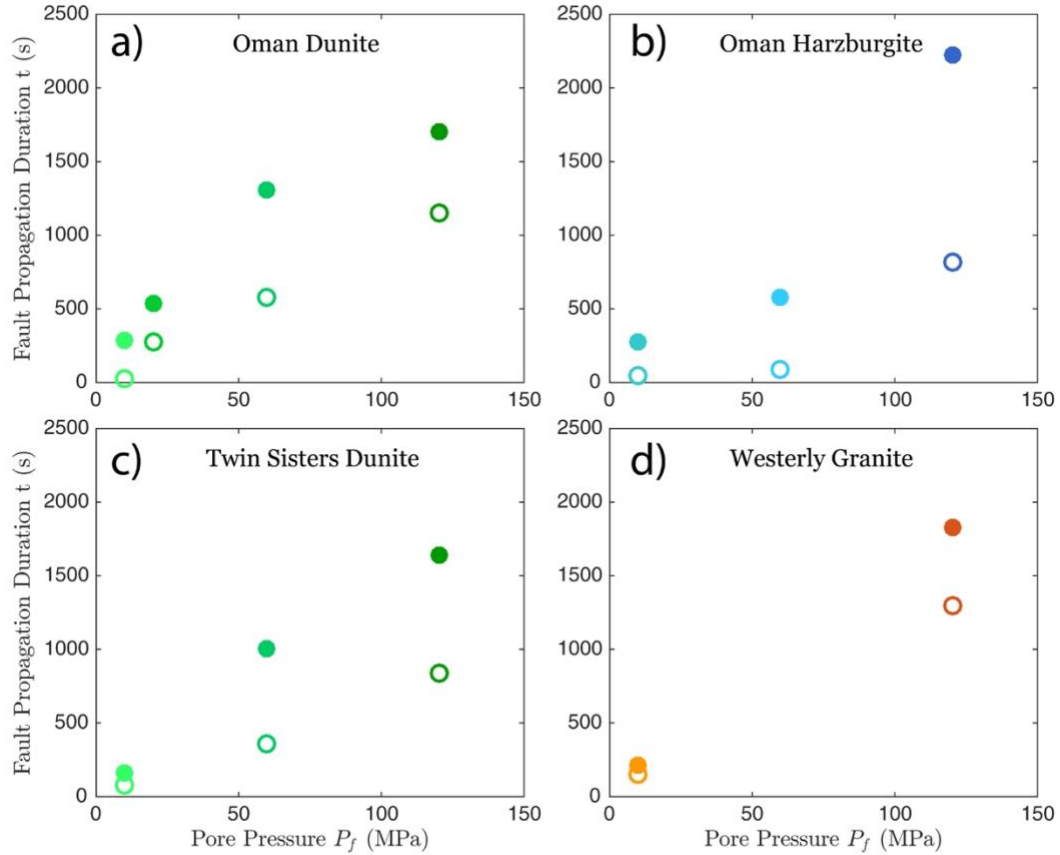


Figure 5.5: Fault propagation duration of a) Oman dunite; b) Oman harzburgite; c) Twin Sisters dunite and d) Westerly granite at different pore fluid pressures from 10 to 120 MPa. Solid circles represent the total fault propagation duration and open circles represent the fault nucleation duration.

Effect of pore fluid pressure on stress drops varies in different types of rocks (Figure 5.4). In Oman dunite and harzburgite (Figure 5.4a, b), at low pore fluid pressures of 10~20 MPa, the stress drop is abrupt, represented by the nearly vertical slope on the stress-time plot. As pore fluid pressure increases, the faulting event slows down with a shallower slope on the stress-time plot. At 120 MPa the stress drop becomes a long, extended process that takes ~30 minutes. Twin Sisters dunites exhibit very similar

faulting behaviors. However, there are large natural sample-to-sample variations in this suite (Figure 5.4c). In Westerly granite, the stress drops are sudden at all pore fluid pressure conditions.

At low pore pressure of 10 MPa, the stress drop is accompanied by audible sounds. At high pore pressure of 120 MPa, the stress drop is no longer audible. Similar effects have been observed in fracturing experiment (French & Zhu, 2017) and friction experiment (Leeman et al., 2016) where dynamic events are associated with loud acoustic emissions. The contrast in audibility of fracturing in granite between low (10 MPa) and high (120 MPa) pore fluid pressure indicates a transition from dynamic to quasi-stable faulting. In the dunite and harzburgite experiments, no sound was detected in association with the faulting events at all tested conditions. This may suggest a different fracturing mechanism of olivine dominated rock compared to granite which is quartz and feldspar dominated.

5.3.3 Micro-structure

Microstructure analysis of sample post deformation show different behaviors at different pore fluid pressures under the same effective pressure (Figure 5.6, 5.10, 5.11, 5.12, 5.13). At low pore fluid pressure, the fault geometry does not show any complexity. The fault plane is relatively localized with a single fault plane at an angle of 20~40° to the σ direction. As pore fluid pressure increases, the fault becomes more dispersed with more complex fault structure with an average fault angle of 20~30° to the σ direction. Minor faults are observed branching out from the main fault plane at high angles (30~40°). Development of shear bands is also observed within the fault.

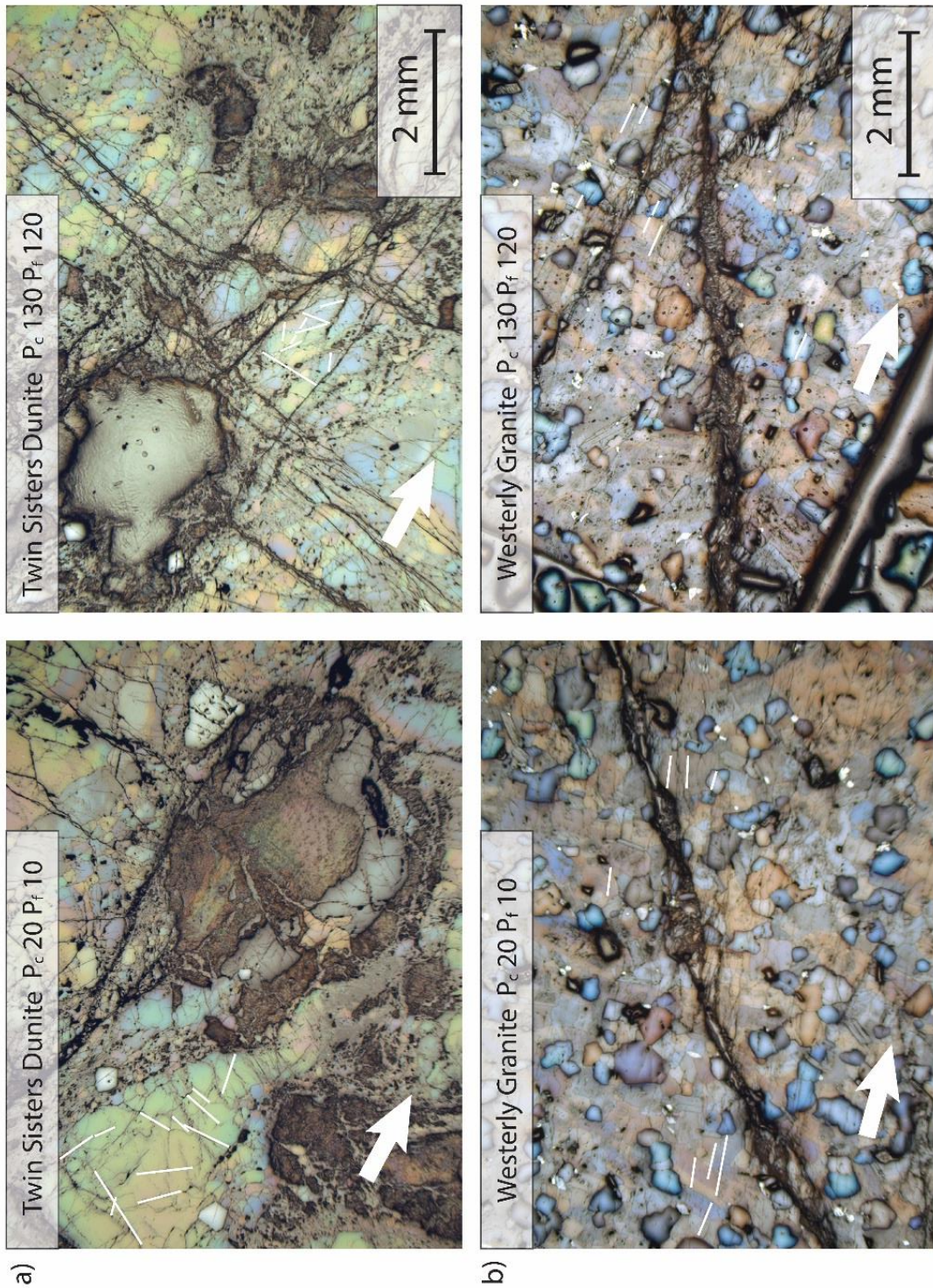


Figure 5.6: Reflected light image of the microstructures of the fractured a) Twin Sisters Dunitic and b) Westerly granite deformed at an effective pressure of 10 MPa and under low (10MPa) and high (120MPa) pore fluid pressure conditions. The white arrow head marks the direction of maximum principal stress (σ_1). The white line marks some of the intra-granular micro-cracks.

The microstructures are also affected by the composition of the samples. The olivine grains from Twin Sisters dunite sample are more heavily fractured (Figure 5.6a) compared to the quartz and feldspar in granite (Figure 5.6b). Trans-granular fractures coalesce and form a complicated fracture system in the dunite samples while the granite is observed with a through-going shear fracture that intersects the sample.

Intra-granular cracks are observed in both Twin Sisters dunite and Westerly granite samples. In granite, the intra-granular cracks are mostly mode-I tensile cracks parallel/sub-parallel to the σ_1 direction. This is less common in the dunite where orientations of intra-granular cracks appear to be random. The Oman dunite and harzburgite are heavily serpentinized and does not shown significant intragranular fractures.

5.4 Discussion

5.4.1 Stability of Fault Rupture

According to Rice & Rudnicki (1979), a dynamic fault instability occurs when strain weakening takes place at a faster rate than the elastic unloading of the surroundings (Figure 5.7a). Results from this study on the slip weakening distance show that the slip weakening distance is short at low pore fluid pressure of 10~20 MPa compared to a longer weakening distance at pore fluid pressure of 60 MPa or higher. The increase in the slip weakening distance also leads to a shallower slope of the slip weakening curve (Figure 5.7b and 5.14) which represents a stabilization of faulting. This indicates that an increase in pore fluid pressure stabilizes the fault rupture through increasing the slip weakening distance.

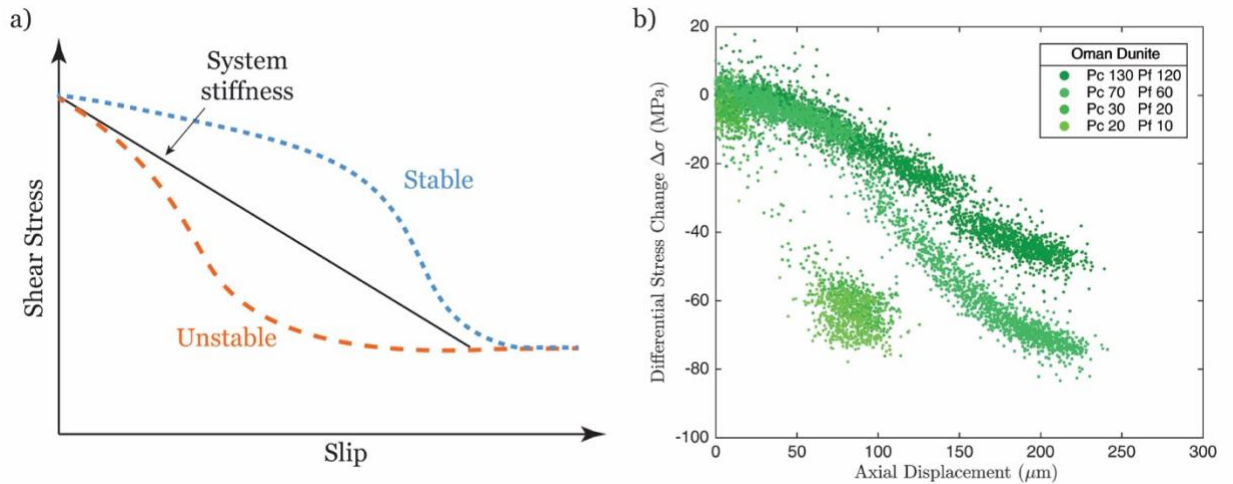


Figure 5.7: a) Schematics of slip weakening slope and fault stabilities modified from Rice & Rudnicki, (1979). b) Slip weakening slope of Oman dunite sample tested at pore fluid pressure ranges from 10 to 120 MPa.

The microstructure shows that the fault is localized at low pore fluid pressure and changes to distributed fault network at high pore fluid pressure. The localization strain can be considered as an instability in rock deformation (Rudnicki & Rice, 1975). The presence of the distributed fault at high pore fluid pressure condition indicates stabilized faulting.

5.4.2 Mechanism of Fault Stabilization

Result from this study has revealed that under the same effective pressure, higher pore fluid pressure can lead to stabilized faulting. Previous studies have related this to the dilatant hardening (French & Zhu, 2017; Rice, 1975; Rudnicki, 1984). A similar effect can take place in our experiments. This effect is more prominent at high pore fluid pressure conditions, as fault propagation could lead to larger pore fluid pressure reduction at the crack tip and, therefore, a larger local increase of effective pressure and a more significant effect of strengthening.

The distributed fault structure observed at high pore fluid pressure could be a manifestation of larger effect from dilatant hardening. The rock is considered as a generally uniform body with defects such as microcracks as the potential fracture nucleation sites. At high pore fluid pressure, the larger effects from dilatant hardening would strengthen the propagation of fault until slip is inhibited. Then new fractures would develop from the pre-existing defects until the rock is strengthened again, and new fractures would be generated. This process due to strengthening from dilatant hardening would result in a distributed shear fracturing network. At low pore fluid pressure, a localized fracture plane is preferred as the dilatant hardening is not so prominent. The more heavily fractured grains and more complex fracture network from dunite samples compared to granite may also indicate a larger effect from dilatant hardening.

The observations on the faulting events also indicate that dilatant hardening not only affects the fault propagation, but also extend the duration of fault nucleation by strengthening the development of micro-cracks. However, to further quantify this effect on fault nucleation, a systematic study on the brittle creep behavior at different pore fluid pressure conditions is required.

The permeability of the sample may also contribute to the strengthening. Samples tested in this study are considered as low permeability samples. Previous studies have shown that samples deformed at strain rate comparable to this study can be considered as partially drained (Brace & Martin, 1968). This may lead to a variation in the pore fluid pressure during deformation. However, no significant pore volume change has been observed before and after fault development from this study. This reflected a

minor amount of volume change of the rock which limited the variation of imposed pore fluid pressure due to low permeability. In addition, the deformation rate during fault propagation could become orders of magnitude faster than the imposed rate and promote draining. Studies have also demonstrated that the effect of dilatant hardening also leads to a slow-down of failure in porous sandstones (French et al., 2012), which has permeability orders of magnitude higher than samples tested in this study. Based on these, we think that variations in pore fluid pressure associated with the permeability may promote dilatant hardening at high pore fluid pressure but should not act as the primary control on the deformation in our experiment. The main control on the fault stabilization should still come from dilatant hardening.

5.4.3 Micro-cracks Development

Microstructure analysis on the Twin Sisters dunite and Westerly granite shows a network of trans-granular fractures in the dunite compared to the relatively localized fault in granite (Figure 5.6). This results in a more distributed fracture network in dunite samples comparing to granite which may also be the reason why fracturing in the dunite is inaudible compared to the loud rupture in granite. The micro-fractures are also denser in the dunite comparing to granite which may be a manifestation of larger effect of strengthening.

Analysis on the intra-granular cracks shows that the granite is dominated by the cracks parallel/sub-parallel to the σ_1 direction which is uncommon in the dunite. This is consistent with previous studies that Westerly granite fails by the interaction of mode-I tensile cracks (French & Zhu, 2017; Reches & Lockner, 1994). The Twin Sisters dunite seem to be similar to the serpentinite which show highly isotropic micro-

cracks orientations (Brace et al., 1966; Escartín et al., 1997b; French & Zhu, 2017). The fracturing of dunite could be a result of the mode-II cracks. The Oman dunite and harzburgite are highly serpentinized. The deformation could be mostly accommodated by the sliding along grain boundaries. This may also explain the observation that the intergranular cracks are not well developed in Oman dunite and harzburgite. This also explains that the dunite shows no dilatancy from the strain-gauge measurements compared to the granite prior to the fracturing as the serpentine has been found to be non-dilatant during deformation (Escartín et al., 1997b, 2001). However, quantitative characterizations of on the micro-structures of the deformed samples are required before a solid conclusion can be drawn.

5.4.4 Stabilization Effect of Different Sample Composition

Four different samples were tested in this study. The strengthening effect appears to show dependence on the composition. In granite samples, the stabilization mainly manifests in increasing the duration of faulting, whereas the rates and magnitudes of the main faulting events remain similar. In contrast, ultramafic rocks (dunite and harzburgite) deformed at high pore fluid pressures not only have much longer durations of fault propagation, the magnitudes and rates of stress drop are also significantly reduced (Figure 5.4 and 5.14). This is consistent with our results that serpentine and olivine dominated samples show larger strengthening in frictional slip comparing to the quartz and clay dominated samples (see Chapter 3).

We speculate that the different modes of microcracks in olivine and quartz are responsible for the different styles of strengthening. In granite, dilatancy caused by mode-I cracks takes place mostly during fault nucleation. This is supported by the large

amount of dilatancy observed before the stress drop. Dilatant hardening can explain the observed strengthening in granite during fault nucleation. Because the granite fracture is mainly caused by the interaction of mode-I micro-fractures (Moore & Lockner, 1995; Reches & Lockner, 1994). Although the magnitude of the stress drop in granite samples does not vary significantly at different pore pressures, a transition from dynamic to quasi-static faulting at high pore pressures can be inferred from the disappearance of the audible sounds associated with faulting. In contrast, in dunite and harzburgite samples, because non-mode-I cracks (e.g. Escartín et al., 1997; French & Zhu, 2017) do not produce large dilation, the dilatant hardening effect is less prominent, which can explain the strain softening observed during fault nucleation in the ultramafic samples. Mix mode trans-granular cracks are observed mostly during fault propagation, consistent with results from French & Zhu (2017).

5.4.5 Faulting Stability with the Presence of High Pore Fluid Pressure

There are many similarities between the mechanism of fracture and friction on faults. Both of them involves grain breakage and rotation, crack propagation and even plastic deformation (Lockner & Beeler, 2002). Previous studies on rock friction have found effect of stabilization associated with high pore fluid pressure (Leeman et al., 2016; Chapter 3), which may lead to the transition of frictional behavior from dynamic seismogenic slip to transitional slow slips. The alteration of the mechanical behavior of the fault due to presence of pore fluid may also occur in intact rock.

Observations from this study show that the high pore fluid pressure stabilizes brittle faulting and slows down fracture propagation similar to those observed from friction studies. The processes of crack development and coalescence studied here may also

present in gouge materials during friction and affect the frictional behavior. The quasi-stable faulting observed from this study may be an analogy of transitional slip behavior of slow slips in the context of rock friction and could have wider implications on the earthquake mechanisms in the transition zone where occurrence of slow-slips and tremors are often associated with high pore fluid pressure (Obara, 2002; Okazaki et al., 2013).

5.5 Conclusion

The results of our study have demonstrated that:

- Under constant effective pressure, increase in pore fluid pressure lead to the stabilization of fault propagation; both duration fault nucleation and propagation has been extended with increasing pore fluid pressure;
- Observation of similar effects among different rock types demonstrate that the high pore fluid pressure stabilization is not limited to one lithology;
- The strengthening effect of the pore fluid pressure on the post-failure behavior is sensitive to lithology;
- Different modes of micro-cracks may contribute to the dependence of pore fluid pressure strengthening effect on rock types.

The discovery from this study demonstrated the universality of the high pore fluid pressure strengthening effect fault nucleation and propagation. It provides insights into the fault stabilization in association with the presence of high pore fluid pressure. In the meantime, it indicates that rocks with various compositions may response differently to the strengthening due to different modes of cracking. The study also

provides insights on the occurrence of transitional fault slip behaviors in a variety of crustal regions.

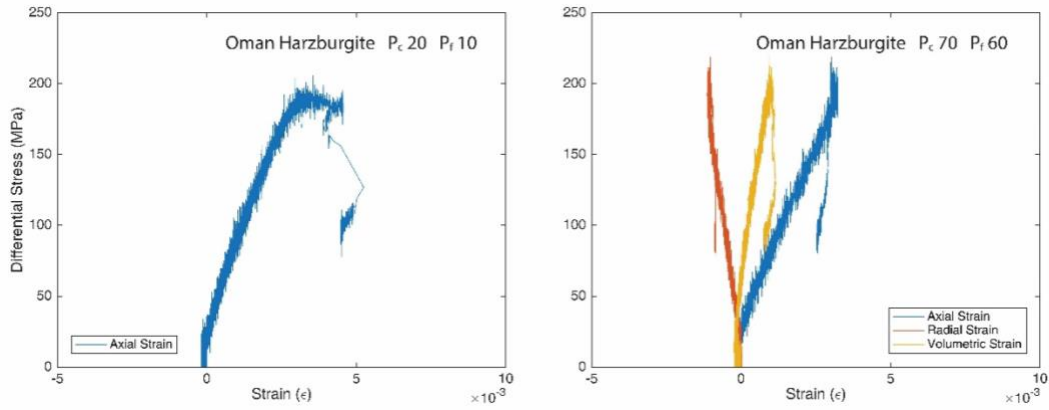


Figure 5.8: Strain gauge data of Oman Harzburgite samples deformed. Some strain data are missing due to strain gauge malfunctions.

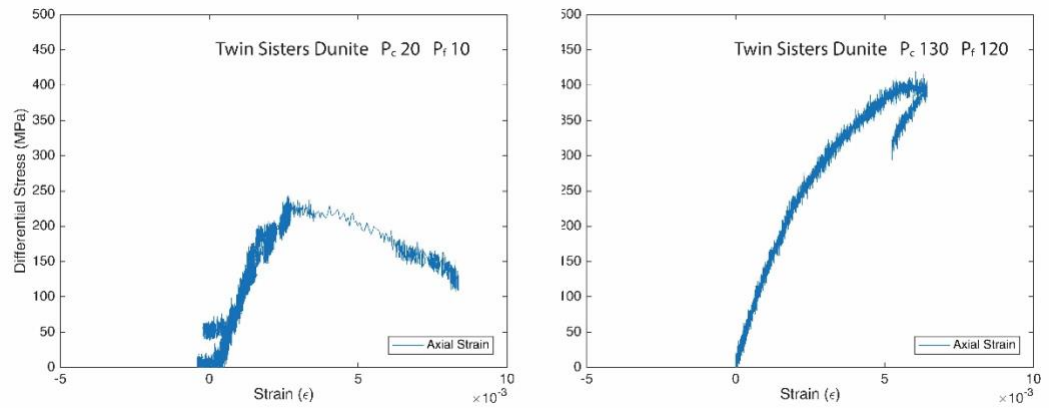


Figure 5.9: Strain gauge data of Oman Harzburgite samples deformed. Some strain data are missing due to strain gauge malfunctions.



Figure 5.10: Reflected light image of microstructures of fractured Oman Dunite deformed at an effective pressure of 10 MPa and under low (10 MPa) and high (120 MPa) pore fluid pressures.

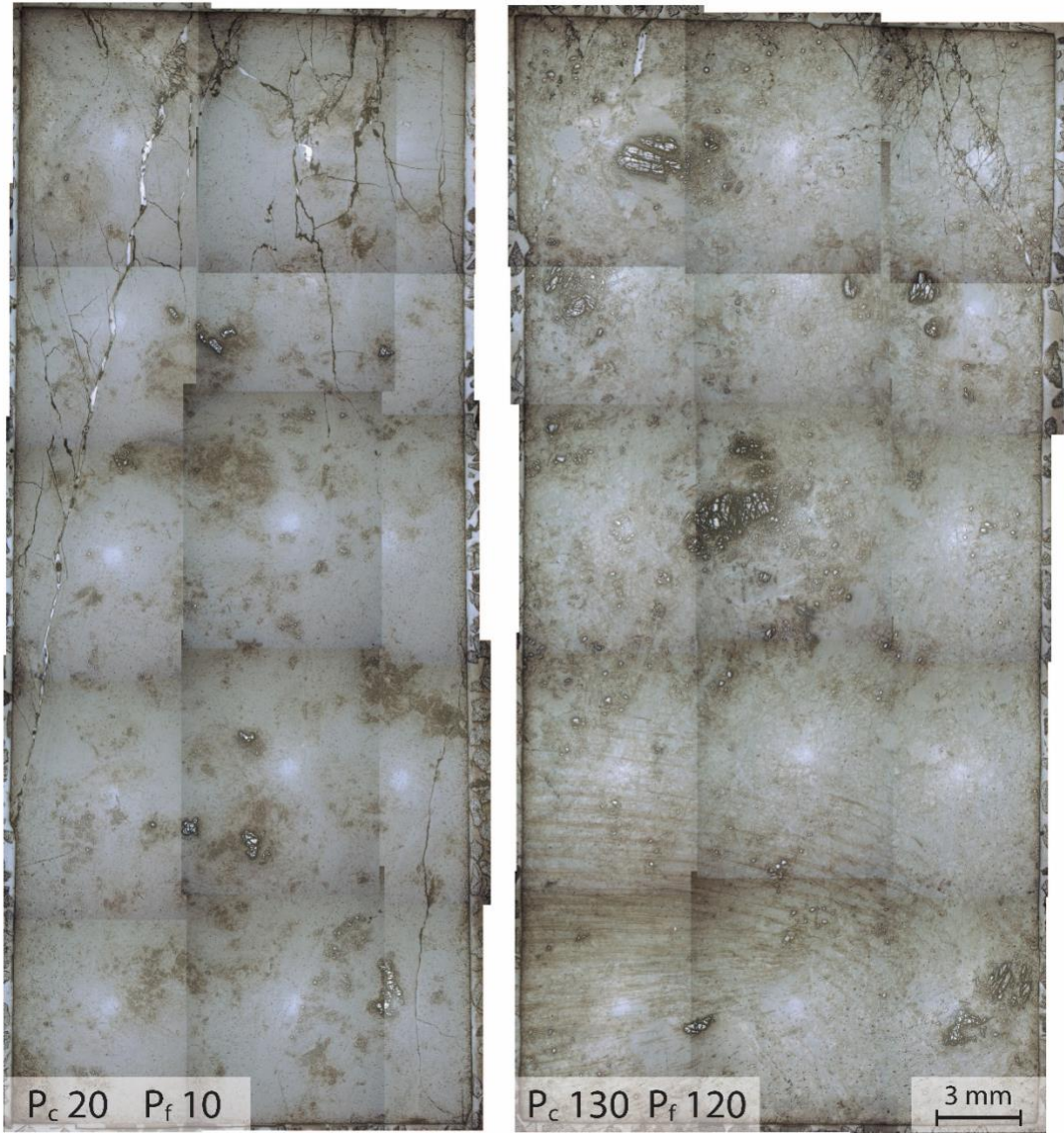


Figure 5.11: Reflected light image of microstructures of fractured Oman Harzburgite deformed at an effective pressure of 10 MPa and under low (10 MPa) and high (120 MPa) pore fluid pressures.

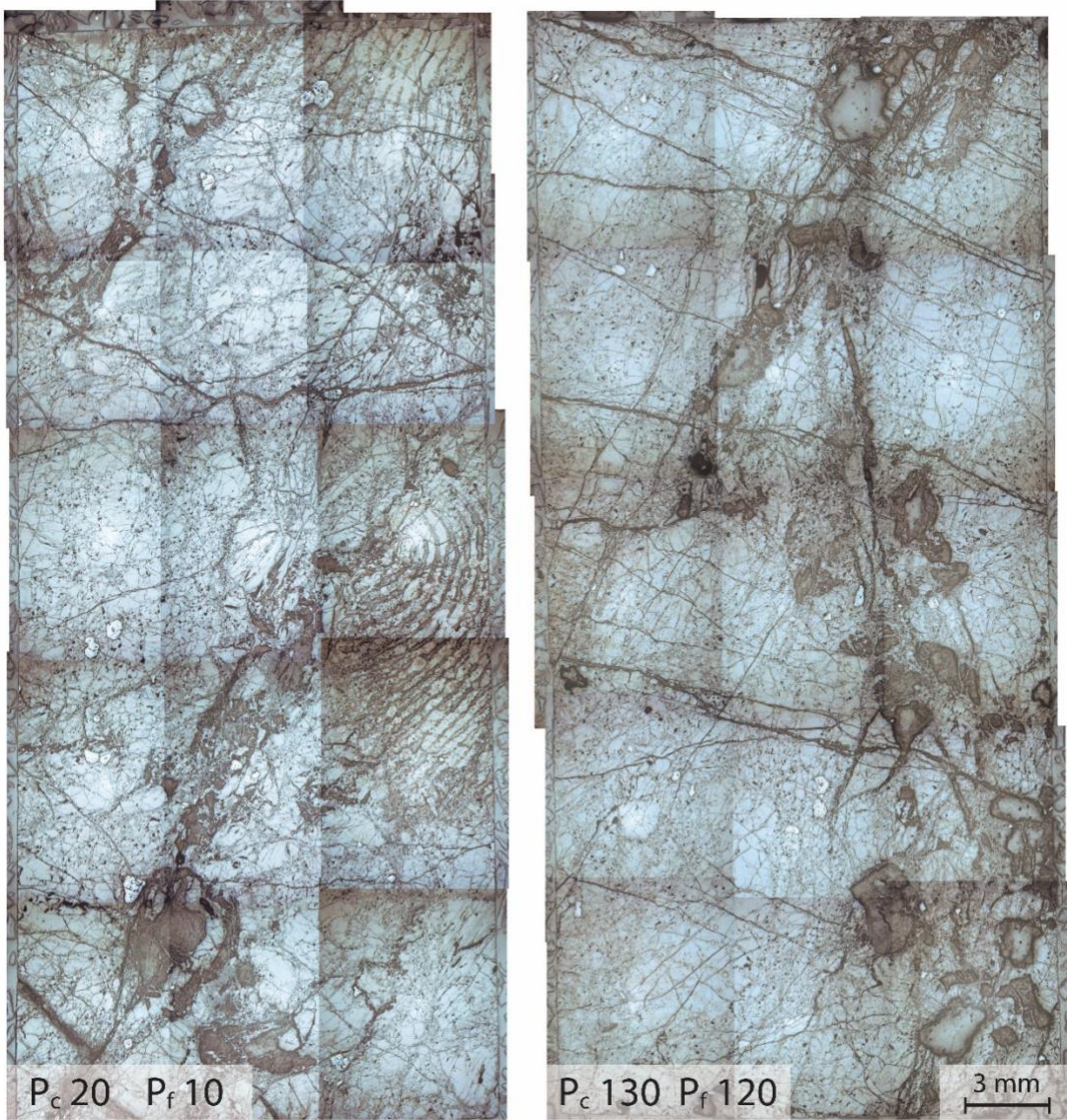


Figure 5.12: Reflected light image of microstructures of fractured Twin Sisters Dunite deformed at an effective pressure of 10 MPa and under low (10 MPa) and high (120 MPa) pore fluid pressures.

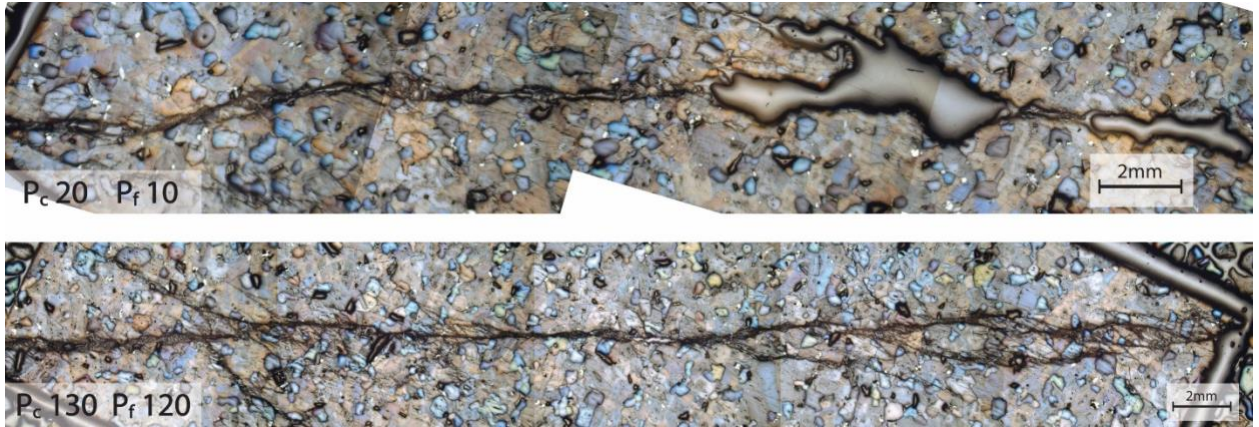


Figure 5.13: Reflected light image of microstructures of fractured Westerly granite deformed at an effective pressure of 10 MPa and under a) low (10 MPa) and b) high (120 MPa) pore fluid pressures.

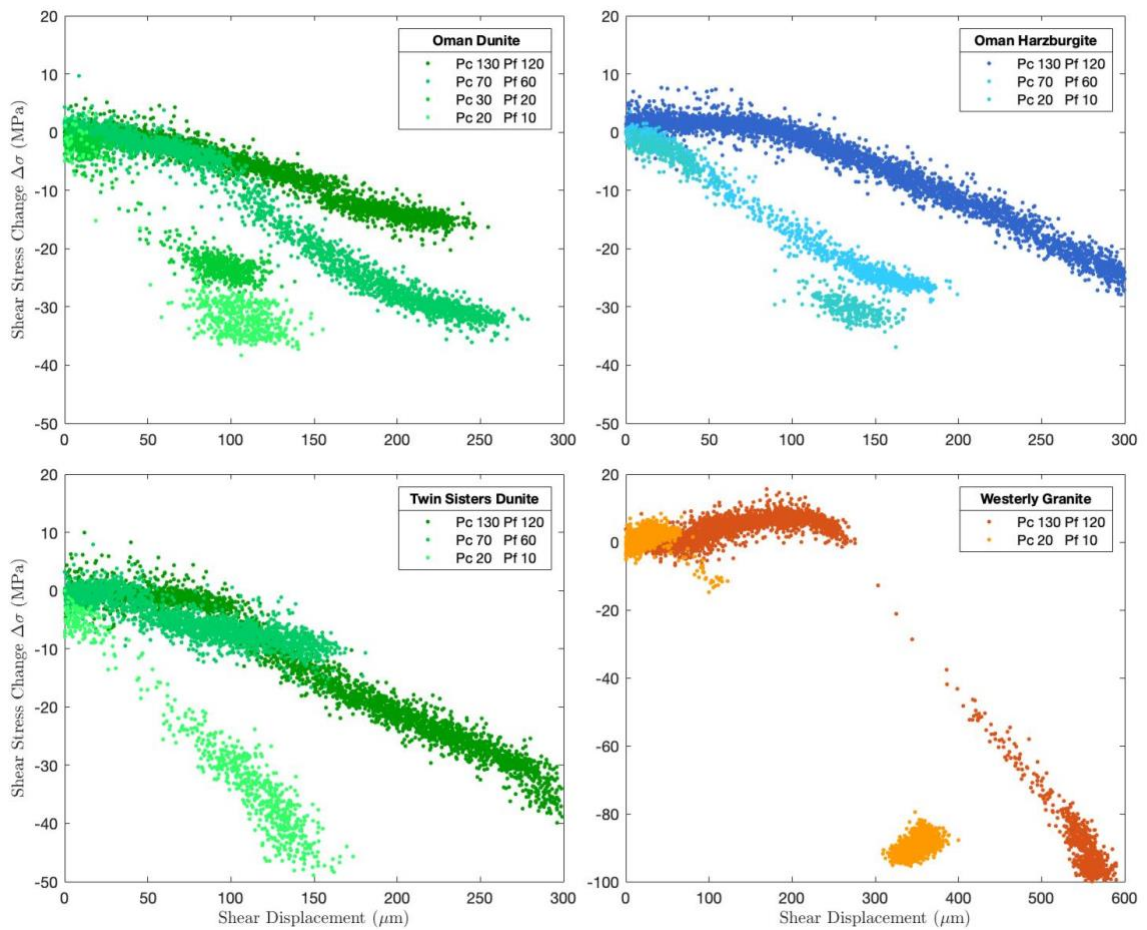


Figure 5.14: Slip weakening of all tested samples at pore fluid pressure ranges from 10 to 120 MPa.

Appendix A. List of Symbols

Symbol	Physical meaning
τ	Shear stress
σ_n	Normal stress
μ	Friction coefficient
c	Cohesion
D_c	Characteristic displacement
k	Stiffness of the system
k_c	Critical stiffness of the material
P_e	Effective pressure
P_c	Confining pressure
P_f	Pore fluid pressure
Q	Discharge of fluid flow through material
κ	Permeability of the sample
η	Viscosity of fluid
σ	Differential stress
σ_{cor}	Differential stress corrected for the area lost due to slip on saw-cut
σ_{yield}	Yield stress of material
σ_1	Maximum principal stress
σ_2	Intermediate principal stress
σ_3	Minimum principal stress
v	Velocity
v_p	P-wave velocity
v_s	S-wave velocity
d	Axial displacement
s	Shear displacement
t	Time
G	Elastic strain energy release
G_c	Fracture energy
G_r	Radiated energy
M_o	Seismic moment
M_w	Moment Magnitude

ϵ_a	Axial strain
ϵ_r	Radial strain
ϵ_v	Volumetric strain
ν	Poisson's Ratio
r	Radius of the sample
ϕ	Angle of the saw-cut to the axial load
θ	Angle subtended by the point of intersection of two overlapping circles
A_0	Original cross-sectional area of the sample
A	Cross-sectional area of the sample after offset correction
a	Rate and state friction parameter
b	Rate and state friction parameter
β	Gutenberg-Ritcher b -value

Appendix B. Friction Data Processing

Friction Parameters Calculation

Following a change in slip velocity (v_1 to v_2), the friction coefficient evolves from one steady state (μ_1) to the next steady state (μ_2). The D_c describes the displacement required for the friction coefficient to evolve (see Figure 1.1).

The velocity dependence factor is calculated based on the equation:

$$a - b = \frac{\mu_2 - \mu_1}{\ln(v_2/v_1)} \quad (B.1)$$

This is derived from equation which describes the dependence of the dynamic friction coefficient on sliding velocity and other variables (Dieterich, 1979; Ruina, 1983):

$$\mu_s = \mu_1 + a \ln\left(\frac{v_2}{v_1}\right) + b \ln\left(\frac{v_1 \theta}{D_c}\right) \quad (B.2)$$

$$\frac{d\theta}{dt} = 1 - \frac{\theta v}{D_c} \quad (B.3)$$

$$\mu_s = \mu_1 + (a - b) \ln\left(\frac{v_2}{v_1}\right) \quad (B.4)$$

where μ_1 is the steady-state friction coefficients and μ_s is the dynamic friction coefficients at slip velocity of v_1 and v_2 respectively, a and b are material properties, D_c is the displacement over which friction evolves with slip, and θ is the state variable.

D_c describes the displacement over which friction evolves into $1/e$ of the change in steady state friction, i.e. when μ change to level of b/e . In this study, the D_c is estimated as $(1-1/e)$ of the displacement for friction coefficient to evolve from one steady state to the next steady state where b value is high and cannot be ignored. In cases of olivine, quartz and chrysotile friction, the b value is small. Therefore, b/e is close to zero. The

D_c is then calculated as the displacement for friction coefficient to evolve from one steady state to the next steady state.

Shear Stress Calculation

In this experiment, the shear stress (τ) on the gouge material is calculated using the following equation:

$$\tau = \frac{1}{2} \sigma * \sin(2\phi) \quad (B.5)$$

where σ is the differential stress and ϕ is the angle of the saw-cut surface.

Appendix C. Data Corrections

Seal Friction Correction

The axial load (differential stress) applied to the sample is measured using a load cell. When the load cell is located outside the vessel, some of the measured force is resisted by the friction between the advancing piston and confining pressure seal assembly. Therefore, it is necessary to correct the differential stress by subtracting seal friction.

Seal friction can be determined by first advancing the piston at a constant rate (i.e., 10 $\mu\text{m/s}$) until it makes contact with the sample. Then the piston is retracted with a rate one order of magnitude lower than the advancing rate (i.e., 1 $\mu\text{m/s}$) until the differential stress is fully released and becomes constant again. The seal friction is the difference between the two constant stresses at each stable state.

Because the piston is only moving in one direction during the deformation, the true differential stress reading should be Axial load $- P_c -$ Seal Friction.

Contact Offset Correction for Friction Experiment

As the experiments are conducted on saw-cut samples, increasing slip on the surfaces would cause a decrease in the overlapping area. This would make the true differential stress values higher than the measurements read from the force gauge. Following the calculation of Tembe et al. (2010), the area correction would result in 23% stress adjustment by 8 mm of axial shortening. Therefore, a geometric factor A/A_0 is used for this correction (Scott et al., 1994):

$$\frac{A}{A_0} = \frac{\theta - \sin\theta}{\pi} \quad (C.1)$$

$$\theta = \pi - 2\sin^{-1}\left(\frac{d}{2r}\tan\left(\frac{\phi\pi}{180}\right)\right) \quad (C.2)$$

where A_0 and A are the original and corrected cross-sectional area of the sample, respectively, θ is the angle subtended by the point of intersection of two overlapping circles, at the centers of the circles, d is the axial displacement measured by the LVDTs, and r is the radius of the sample. The corrected differential stress (σ_{cor}) is:

$$\sigma_{cor} = \sigma \frac{A_0}{A} \quad (C.3)$$

Elastic Relaxation Correction for Unstable Friction Experiment

During the stick-slip events, stress drops as the slip instability occurs. This leads to an axial relaxation of sample in associated with the slip. Because the slip distance is measured by the axial displacement of the main ram LVDT, this axial relaxation during stress drops would result in an underestimation of actual slip distance. This is corrected using the following equation:

$$\Delta s_{cor} = \Delta s + \frac{2}{\sqrt{3}} \frac{\Delta\sigma}{E} \cdot L \quad (C.4)$$

where Δs is the measured slip distance, $\Delta\sigma$ is the drop in differential stress during the slip, E is the elastic moduli of the sample and L is the length of the sample. In this experiment, the L/E is measured from the slope of elastic loading of the sample, which described the elastic shortening of sample per unit of applied axial stress.

Appendix D. Image Data Processing Code (MATLAB)

2D Porosity Distribution Profile Plot Script

```
function PorosityDistribution2D(varargin)
%%%%%%%%%%%%%%%%%%%%%%%%%%%%%%%%%%%%%%%%%%%%%%%%%%%%%%%%%%%%%%%%%%%%%%%%
% Function "PorosityDistribution2D"
% written by Tiange Xing
%
% The "PorosityDistribution2D" function is used for calculating a 2D
% Porosity profile from the imported binary image(format.tif).
%
% Inputs:
% varargin -- the file names of the binary images in .tiff format
% Output:
% a figure of 2D porosity profiles from a slice of the 3D binary
% image.
% This function requires function "PorosityProfiler2D" to work.
%%%%%%%%%%%%%%%%%%%%%%%%%%%%%%%%%%%%%%%%%%%%%%%%%%%%%%%%%%%%%%%%%%%%%%%%

filenum=length(varargin); % number of input tiff files
cm =colormap(cool(filenum));% make a colormap for later plotting

hdl=figure(1); clf; hold on;
set(hdl,'position',[90 50 795 950]);
set(gca,'fontsize',18);
windowlength = 0;
for i=1:filenum
    PorosityProfiler2D(varargin{i},cm(i,:),windowlength);
end
box on; grid on;
ylabel('Porosity (%)','fontsize',18);
xlabel('Distance (\mum)','fontsize',18);

h=legend(varargin);
set(h,'fontsize',18);
```

```

function PorosityProfiler2D(varagin,cm>windowlength)
%%%%%%%%%%%%%%%%%%%%%%%%%%%%%%%%%%%%%%%%%%%%%%%%%%%%%%%%%%%%%%%%%%%%%%%%
% Function "PorosityProfiler2D"
% written by Kevin J. Miller, adapted by Tiange Xing.
%
% The "PorosityProfiler2D" function is used for calculating a 2D
Porosity
% profile from the imported binary image(format.tif).
%
% varagin is the name of the .tif file to be imported.
% cm is the color scheme for the plot.
% This function requires function "Tif3DReader" to work.
%%%%%%%%%%%%%%%%%%%%%%%%%%%%%%%%%%%%%%%%%%%%%%%%%%%%%%%%%%%%%%%%%%%%%%%%

drName=[pwd,'\'];
I = logical(Tif3DReader(drName, varagin));
width = size(I, 1);
height = size(I, 2);
nSlice = size(I, 3);% number of total slices

phi=zeros(width,1);
if 2*windowlength+1>nSlice
disp(...
'ERROR: Moving average window is too large! Please choose a smaller
one!');
else
for i=1>windowlength
phi(i) = sum(sum(sum(I(1:2*i-1,.,:))))/(nSlice*height*(2*i-1));
end
for i=windowlength+1:width-windowlength
phi(i) = sum(sum(sum(I(i-windowlength:i+windowlength,...
:,:))))/(height*nSlice*(2*windowlength+1));
end
for i=width-windowlength+1:width
phi(i) = sum(sum(sum(I(2*i-width:width,...
:,:))))/(height*nSlice*(2*width-2*i+1));
end
end

yPlot=0.65.*[1:width];
plot(yPlot,100*phi,'-', 'color',cm, 'LineWidth',3);
axis([0.65, 0.65*nSlice,0,18]);
totalporosity=sum(sum(sum(I)))/numel(I);
fprintf('The total porosity of data %s is: %2.5f%% \n',...
varagin,100*totalporosity);

```

3D Porosity Distribution Plot Script

```
function [Porosity]=PorosityDistribution3D(xdim,ydim,zdim,varargin)
%%%%%%%%%%%%%%%%%%%%%%%%%%%%%%%%%%%%%%%%%%%%%%%%%%%%%%%%%%%%%%%%%%%%%%%%
% Function "PorosityDistribution3D"
% written by Tiange Xing
%
% The "PorosityDistribution3D" function is used to examine the 3D
porosity
% change in the segmented microtomography data.
%
% Inputs:
% varargin -- the file names of the binary images in .tif format
% Output:
% Porosity -- vector which contains all the subvolume's mean
porosity.
% a 3D view of porosity profiles of the input binary images.
% This function requires function "PorosityProfiler3D" to work.
%%%%%%%%%%%%%%%%%%%%%%%%%%%%%%%%%%%%%%%%%%%%%%%%%%%%%%%%%%%%%%%%%%%%%%%%
filenum=length(varargin); % number of input tiff files
hdl=figure(1); clf; hold on;

% Set colormap
cm = colormap(cool(300));

% Plot the porosity of each subvolume as a circle in a 3D space
Porosity = zeros(xdim*ydim*zdim,filenum);
for i=1:filenum
    fig = figure(i);
    [RePoro,xin,yin,zin] =
PorosityProfiler3D(xdim,ydim,zdim,varargin{i});
    Porosity(:,i) = RePoro;

    for z=1:zdim;
        for x =1:xdim;
            for y = 1:ydim;
                coordinates = y + ydim*(x-1) + ydim*xdim*(z-1);
                sizeP = Porosity(coordinates,i)*450;
                h = scatter3((x-0.5)*xin*0.65,(y-0.5)*yin*0.65,(z-
0.5)...
                            *zin*0.65,sizeP+1,...

cm(ceil(Porosity(coordinates,i)*100)+1), 'filled');
                h.MarkerEdgeColor = 'k';
            end
        end
    end
end
xlabel('Width  $\mu$  m','fontsize',15,'interpreter','LaTeX');
ylabel('Length  $\mu$  m','fontsize',15,'interpreter','LaTeX');
zlabel('Height  $\mu$  m','fontsize',15,'interpreter','LaTeX');
set(gca,'Xdir','reverse');
set(gca,'Ydir','reverse');
set(gca,'Zdir','reverse','fontsize',15);
axis equal
```

```

    FigHandle = figure(i);
    set(FigHandle, 'Position', [100, 100, 900, 800]);

end
box on; grid on;
h=legend(varargin);
set(h, 'fontsize', 15);
axis([0 xdim*xin*0.65 0 ydim*yin*0.65 0 zdim*zin*0.65]);
view(-142,34)

%-----%
% Optional
% Make a movie of the object rotating

% fps = 60; sec = 10;
%
% vidObj = VideoWriter('Porosity Rotation','MPEG-4');
% vidObj.Quality = 100;
% vidObj.FrameRate = fps;
%
% open(vidObj);
% for i=1:fps*sec
%     camorbit(0.5,-0.01,'data',[0 0 1]);
%     writeVideo(vidObj,getframe(gcf));
% end
% close(vidObj);

```

```

function [RePorosity, xin, yin, zin] =
PorosityProfiler3D(xdim, ydim, zdim, fName)
%%%%%%%%%%%%%%%%%%%%%%%%%%%%%%%%%%%%%%%%%%%%%%%%%%%%%%%%%%%%%%%%%%%%%%%%
% Function "PorosityProfiler3D"
% written by Tiange Xing.
% The PorosityProfiler function is used for calculating a 3D
Porosity
% profile from the segmented microtomography data.
%
% Inputs:
% fName -- the file names of the binary images in .tiff format
% Output:
% The average porosity of the input sample and porosity of all the
% subvolumes' mean porosity.
% This function requires function "Tif3DReader" to work
%%%%%%%%%%%%%%%%%%%%%%%%%%%%%%%%%%%%%%%%%%%%%%%%%%%%%%%%%%%%%%%%%%%%%%%%
drName=[pwd, '\'];
I = logical(Tif3DReader(drName, fName));
i = linspace(1, size(I, 1), size(I, 1)); % dimension 1 -- height
j = linspace(1, size(I, 2), size(I, 2)); % dimension 2 -- width
k = linspace(1, size(I, 3), size(I, 3)); % dimension 3 -- slice#
p = randn(xdim, ydim, zdim);
xin = size(I, 1)/xdim;
yin = size(I, 2)/ydim;
zin = size(I, 3)/zdim;
% Divide the input data matrix into smaller subvolumes, and
calculate
% porosity at each subvolume
for z=1:zdim % loop for dimension 3 -- slices
    c = find(zin*(z-1)<k & k<=zin*z, zin);
    for y=1:ydim % loop for dimension 2 -- width
        b = find(yin*(y-1)<j & j<=yin*y, yin);
        for x=1:xdim % loop for dimension 1 -- height
            a = find(xin*(x-1)<i & i<=xin*x, xin);
            AVG = I(a, b, c);
            % porosity of subvolume(x, y, z)
            p(x, y, z) = sum(AVG(:))/(xin*yin*zin);
        end
    end
end

totalporosity=sum(p(:))/numel(p);
RePorosity = reshape(p, 1, (xdim*ydim*zdim));
fprintf('The total porosity of data %s is: %2.5f%% \n', fName, ...
100*totalporosity);

```

```

function FinalImage = Tif3DReader(Dir, FileTif, varargin)

if ~isempty(varargin)
    if strcmp(varargin{1}, 'Plot')
        islice = varargin{2};
        if ischar(islice) && strcmp(varargin{2}, 'All')
            else
                islice = varargin{2};
            end
        end
    end
end

InfoImage=imfinfo([Dir, FileTif]);
mImage=InfoImage(1).Width;
nImage=InfoImage(1).Height;
NumberImages=length(InfoImage);
FinalImage=zeros(nImage,mImage,NumberImages,'uint16');

TifLink = Tiff([Dir, FileTif], 'r');
for i=1:NumberImages
    TifLink.setDirectory(i);
    FinalImage(:,:,i)=TifLink.read();
end
TifLink.close();
end

```

Bibliography

- Aki, K. (1966). Generation and propagation of G waves from the Niigata Earthquake of June 16, 1964. Part 2. Estimation of earthquake movement, released energy, and stress-strain drop from the G wave spectrum. *Bulletin of the Earthquake Research Institute*, 44, 73–88. Retrieved from http://www.eri.u-tokyo.ac.jp/en/?page_id=169
- Andreani, M., Luquot, L., Gouze, P., Godard, M., Hoise, E., & Gibert, B. (2009). Experimental Study of Carbon Sequestration Reactions Controlled by the Percolation of CO₂-Rich Brine through Peridotites. *Environmental Science & Technology*, 43(4), 1226–1231. <https://doi.org/10.1021/es8018429>
- Atkinson, B. K. (1984). Subcritical crack growth in geological materials. *Journal of Geophysical Research: Solid Earth*. <https://doi.org/10.1029/JB089iB06p04077>
- Atkinson, B. K., & Meredith, P. G. (1987). Fracture mechanics of rock- The Theory of Subcritical Crack Growth with Applications to Minerals and Rocks. In *Academic Press Geology Series*. <https://doi.org/10.1007/978-94-007-2595-9>
- Audet, P., Bostock, M. G., Christensen, N. I., & Peacock, S. M. (2009). Seismic evidence for overpressured subducted oceanic crust and megathrust fault sealing. *Nature*. <https://doi.org/10.1038/nature07650>
- Audet, P., & Schaeffer, A. J. (2018). Fluid pressure and shear zone development over the locked to slow slip region in Cascadia. *Science Advances*. <https://doi.org/10.1126/sciadv.aar2982>
- Bangs, N. L. B., Moore, G. F., Gulick, S. P. S., Pangborn, E. M., Tobin, H. J., Kuramoto, S., & Taira, A. (2009). Broad, weak regions of the Nankai Megathrust and implications for shallow coseismic slip. *Earth and Planetary Science Letters*. <https://doi.org/10.1016/j.epsl.2009.04.026>
- Bedford, J., Fusses, F., Leclère, H., Wheeler, J., & Faulkner, D. (2017). A 4D view on the evolution of metamorphic dehydration reactions. *Scientific Reports*, 7(1). <https://doi.org/10.1038/s41598-017-07160-5>
- Beeler, N. M. (2007). Laboratory-observed faulting in Intrinsically and Apparently Weak Materials. *The Seismogenic Zone of Subduction Thrust Faults*, 370–449.
- Beeler, N. M., Tullis, T. E., & Weeks, J. D. (1994). The roles of time and displacement in the evolution effect in rock friction. *Geophysical Research Letters*. <https://doi.org/10.1029/94GL01599>
- Beinlich, A., & Austrheim, H. (2012). In situ sequestration of atmospheric CO₂ at low temperature and surface cracking of serpentinized peridotite in mine shafts.

- Chemical Geology*, 332–333, 32–44.
<https://doi.org/10.1016/j.chemgeo.2012.09.015>
- Beinlich, A., Plümper, O., Hövelmann, J., Austrheim, H., & Jamtveit, B. (2012). Massive serpentinite carbonation at Linnajavri, N-Norway. *Terra Nova*, 24(6), 446–455. <https://doi.org/10.1111/j.1365-3121.2012.01083.x>
- Bilek, S. L., & Lay, T. (2002). Tsunami earthquakes possibly widespread manifestations of frictional conditional stability. *Geophysical Research Letters*, 29(14), 1–4. <https://doi.org/10.1029/2002GL015215>
- Blackwelder, E. (1925). Exfoliation as a Phase of Rock Weathering, 33(8), 793–806.
- Blanpied, M. L., Lockner, D. A., & Byerlee, J. D. (1995). Frictional slip of granite at hydrothermal conditions. *Journal of Geophysical Research: Solid Earth*. <https://doi.org/10.1029/95JB00862>
- Blanpied, M. L., Marone, C., Lockner, D. A., Byerlee, J. D., & King, D. P. (1998). Quantitative measure of the variation in fault rheology due to fluid-rock interactions. *Journal of Geophysical Research: Solid Earth*, 103(B5), 9691–9712. <https://doi.org/10.1029/98JB00162>
- Brace, W. F., & Bombolakis, E. G. (1963). A note on brittle crack growth in compression. *Journal of Geophysical Research*. <https://doi.org/10.1029/JZ068i012p03709>
- Brace, W. F., & Byerlee, J. D. (1966). Stick-slip as a mechanism for earthquakes. *Science*. <https://doi.org/10.1126/science.153.3739.990>
- Brace, W. F., & Martin, R. J. (1968). A test of the law of effective stress for crystalline rocks of low porosity. *International Journal of Rock Mechanics and Mining Sciences And*. [https://doi.org/10.1016/0148-9062\(68\)90045-4](https://doi.org/10.1016/0148-9062(68)90045-4)
- Brace, W. F., Paulding, B. W., & Scholz, C. (1966). Dilatancy in the fracture of crystalline rocks. *Journal of Geophysical Research*. <https://doi.org/10.1029/jz071i016p03939>
- Brantut, N., Heap, M. J., Meredith, P. G., & Baud, P. (2013). Time-dependent cracking and brittle creep in crustal rocks: A review. *Journal of Structural Geology*. <https://doi.org/10.1016/j.jsg.2013.03.007>
- Bredehoeft, J. D., Djevanshir, R. D., & Belitz, K. R. (1988). Lateral fluid flow in a compacting sand-shale sequence: South Caspian basin. *American Association of Petroleum Geologists Bulletin*.
- Byerlee, J. D. (1978). Friction of rocks. *Pure and Applied Geophysics PAGEOPH*, 116(4–5), 615–626. <https://doi.org/10.1007/BF00876528>

- Byerlee, J. D., & Brace, W. F. (1968). Stick slip, stable sliding, and earthquakes—Effect of rock type, pressure, strain rate, and stiffness. *Journal of Geophysical Research*. <https://doi.org/10.1029/jb073i018p06031>
- Cappa, F., Scuderi, M. M., Collettini, C., Guglielmi, Y., & Avouac, J.-P. (2019). Stabilization of fault slip by fluid injection in the laboratory and in situ. *Science Advances*, 5(3), eaau4065. <https://doi.org/10.1126/sciadv.aau4065>
- Carpenter, B. M., Collettini, C., Viti, C., & Cavallo, A. (2016). The influence of normal stress and sliding velocity on the frictional behaviour of calcite at room temperature: insights from laboratory experiments and microstructural observations. *Geophysical Journal International*, 205(1), 548–561. <https://doi.org/10.1093/gji/ggw038>
- Chernak, L. J., & Hirth, G. (2010). Deformation of antigorite serpentinite at high temperature and pressure. *Earth and Planetary Science Letters*, 296(1–2), 23–33. <https://doi.org/10.1016/j.epsl.2010.04.035>
- Chester, F. M. (1994). Effects of temperature on friction: constitutive equations and experiments with quartz gouge. *Journal of Geophysical Research*, 99(B4), 7247–7261. <https://doi.org/10.1029/93JB03110>
- Chester, F. M., & Higgs, N. G. (1992). Multimechanism friction constitutive model for ultrafine quartz gouge at hypocentral conditions. *Journal of Geophysical Research*. <https://doi.org/10.1029/91JB02349>
- Christensen, N. I. (1966). Elasticity of ultrabasic rocks. *Journal of Geophysical Research*, 71(24), 5921–5931. <https://doi.org/10.1029/JZ071i024p05921>
- Cloetens, P., Barrett, R., Baruchel, J., Guigay, J. P., & Schlenker, M. (1996). Phase objects in synchrotron radiation hard x-ray imaging. *Journal of Physics D: Applied Physics*, 29(1), 133–146. <https://doi.org/10.1088/0022-3727/29/1/023>
- Coble, C. G., French, M. E., Chester, F. M., Chester, J. S., & Kitajima, H. (2014). In situ frictional properties of San Andreas Fault gouge at SAFOD. *Geophysical Journal International*. <https://doi.org/10.1093/gji/ggu306>
- Darcy, H. (1856). Les fontaines publiques de la ville de Dijon. *Recherche*, 647. Retrieved from <http://scholar.google.com/scholar?hl=en&btnG=Search&q=intitle:Les+fontaines+publiques+de+la+ville+de+dijon#0>
- Davis, E. E., & Villinger, H. W. (2006). Transient formation fluid pressures and temperatures in the Costa Rica forearc prism and subducting oceanic basement: CORK monitoring at ODP Sites 1253 and 1255. *Earth and Planetary Science Letters*. <https://doi.org/10.1016/j.epsl.2006.02.042>

- Dean, S. M., McNeill, L. C., Henstock, T. J., Bull, J. M., Gulick, S. P. S., Austin, J. A., ... Permana, H. (2010). Contrasting décollement and prism properties over the sumatra 2004-2005 earthquake rupture boundary. *Science*.
<https://doi.org/10.1126/science.1189373>
- Deschamps, F., Godard, M., Guillot, S., & Hattori, K. (2013). Geochemistry of subduction zone serpentinites: A review. *Lithos*, 178, 96–127.
<https://doi.org/10.1016/j.lithos.2013.05.019>
- Dieterich, J. H. (1972). Time-dependent friction in rocks. *Journal of Geophysical Research*, 77(20), 3690. <https://doi.org/10.1029/JB077i020p03690>
- Dieterich, J. H. (1979). Modeling of rock friction: 1. Experimental results and constitutive equations. *Journal of Geophysical Research*, 84(B5), 2161.
<https://doi.org/10.1029/JB084iB05p02161>
- Dieterich, J. H., & Conrad, G. (1984). Effect of humidity on time- and velocity-dependent friction in rocks. *Journal of Geophysical Research: Solid Earth*, 89(B6), 4196–4202. <https://doi.org/10.1029/JB089iB06p04196>
- Druiventak, A., Trepmann, C. A., Renner, J., & Hanke, K. (2011). Low-temperature plasticity of olivine during high stress deformation of peridotite at lithospheric conditions - An experimental study. *Earth and Planetary Science Letters*, 311(3–4), 199–211. <https://doi.org/10.1016/j.epsl.2011.09.022>
- Dunkel, K. G., Austrheim, H., Renard, F., Cordonnier, B., & Jamtveit, B. (2017). Localized slip controlled by dehydration embrittlement of partly serpentinitized dunites, Leka Ophiolite Complex, Norway. *Earth and Planetary Science Letters*, 463, 277–285. <https://doi.org/10.1016/j.epsl.2017.01.047>
- Dunning, J. D., & Miller, M. E. (1985). Effects of pore fluid chemistry on stable sliding of Berea sandstone. *Pure and Applied Geophysics PAGEOPH*, 122(2–4), 447–462. <https://doi.org/10.1007/BF00874611>
- Eberhardt, E., Stimpson, B., & Stead, D. (1999). Effects of Grain Size on the Initiation and Propagation Thresholds of Stress-induced Brittle Fractures. *Rock Mechanics and Rock Engineering*, 32(2), 81–99.
<https://doi.org/10.1007/s006030050026>
- Edelman, N. (1973). Tension cracks parallel with the axial plane.
- Emmanuel, S., & Berkowitz, B. (2006). Suppression and stimulation of seafloor hydrothermal convection by exothermic mineral hydration. *Earth and Planetary Science Letters*, 243(3–4), 657–668. <https://doi.org/10.1016/j.epsl.2006.01.028>
- Escartín, J., Hirth, G., & Evans, B. (1997a). Effects of serpentinitization on the lithospheric strength and the style of normal faulting at slow-spreading ridges.

- Earth and Planetary Science Letters*, 151(3–4), 181–189.
[https://doi.org/10.1016/S0012-821X\(97\)81847-X](https://doi.org/10.1016/S0012-821X(97)81847-X)
- Escartín, J., Hirth, G., & Evans, B. (1997b). Nondilatant brittle deformation of serpentinites: Implications for Mohr-Coulomb theory and the strength of faults. *Journal of Geophysical Research: Solid Earth*, 102(B2), 2897–2913.
<https://doi.org/10.1029/96JB02792>
- Escartín, J., Hirth, G., & Evans, B. (2001). Strength of slightly serpentinized peridotites: Implications for the tectonics of oceanic lithosphere. *Geology*, 29(11), 1023–1026. [https://doi.org/10.1130/0091-7613\(2001\)029<1023:SOSSPI>2.0.CO](https://doi.org/10.1130/0091-7613(2001)029<1023:SOSSPI>2.0.CO)
- Evans, B. W. (1977). Metamorphism of alpine peridotite and serpentinite. *Annual Reviews in Earth and Planetary Sciences*, 5, 397–447.
<https://doi.org/10.1146/annurev.ea.05.050177.002145>
- Fagereng, A., & Ellis, S. (2009). On factors controlling the depth of interseismic coupling on the Hikurangi subduction interface, New Zealand. *Earth and Planetary Science Letters*. <https://doi.org/10.1016/j.epsl.2008.11.033>
- Falk, E. S., & Kelemen, P. B. (2015). Geochemistry and petrology of listvenite in the Samail ophiolite, Sultanate of Oman: Complete carbonation of peridotite during ophiolite emplacement. *Geochimica et Cosmochimica Acta*, 160, 70–90.
<https://doi.org/10.1016/j.gca.2015.03.014>
- Faulkner, D., Sanchez-Roa, C., Boulton, C., & den Hartog, S. A. M. (2018). Pore Fluid Pressure Development in Compacting Fault Gouge in Theory, Experiments, and Nature. *Journal of Geophysical Research: Solid Earth*, 123(1), 226–241. <https://doi.org/10.1002/2017JB015130>
- Faulkner, D., & Rutter, E. H. (1998). The gas permeability of clay-bearing fault gouge at 20°C. *Geological Society, London, Special Publications*.
<https://doi.org/10.1144/GSL.SP.1998.147.01.10>
- Fine, R. A., & Millero, F. J. (1973). Compressibility of water as a function of temperature and pressure. *The Journal of Chemical Physics*, 59(10), 5529–5536.
<https://doi.org/10.1063/1.1679903>
- Frank, F. C. (1965). On dilatancy in relation to seismic sources. *Reviews of Geophysics*. <https://doi.org/10.1029/RG003i004p00485>
- French, M. E., Zhu, W., & Banker, J. (2016). Fault slip controlled by stress path and fluid pressurization rate. *Geophysical Research Letters*, 43(9), 4330–4339.
<https://doi.org/10.1002/2016GL068893>
- French, M. E., Boutt, D. F., & Goodwin, L. B. (2012). Sample dilation and fracture in

- response to high pore fluid pressure and strain rate in quartz-rich sandstone and siltstone. *Journal of Geophysical Research: Solid Earth*.
<https://doi.org/10.1029/2011JB008707>
- French, M. E., & Zhu, W. (2017). Slow fault propagation in serpentinite under conditions of high pore fluid pressure. *Earth and Planetary Science Letters*, 473, 131–140. <https://doi.org/10.1016/j.epsl.2017.06.009>
- Fryer, P., Mottl, M. J., Johnson, L., Haggerty, J., Phipps, S., & Maekawa, H. (1995). Serpentine bodies in the forearcs of western pacific convergent margins: Origin and associated fluids. In *Geophysical Monograph Series* (Vol. 88, pp. 259–279). <https://doi.org/10.1029/GM088p0259>
- Fussey, F., Xiao, X., Schrank, C., & De Carlo, F. (2014). A brief guide to synchrotron radiation-based microtomography in (structural) geology and rock mechanics. *Journal of Structural Geology*.
<https://doi.org/10.1016/j.jsg.2014.02.005>
- Fussey, F., Steeb, H., Xiao, X., Zhu, W., Butler, I. B., Elphick, S., & Mäder, U. (2014). A low-cost X-ray-transparent experimental cell for synchrotron-based X-ray microtomography studies under geological reservoir conditions. *Journal of Synchrotron Radiation*, 21(1), 251–253.
<https://doi.org/10.1107/S1600577513026969>
- Fussey, F., Schrank, C., Liu, J., Karrech, A., Llana-Fúnez, S., Xiao, X., & Regenauer-Lieb, K. (2012). Pore formation during dehydration of a polycrystalline gypsum sample observed and quantified in a time-series synchrotron X-ray micro-tomography experiment. *Solid Earth*, 3(1), 71–86.
<https://doi.org/10.5194/se-3-71-2012>
- García, N. A., Register, R. A., Vega, D. A., & Gómez, L. R. (2013). Crystallization dynamics on curved surfaces. *Physical Review E - Statistical, Nonlinear, and Soft Matter Physics*, 88(1). <https://doi.org/10.1103/PhysRevE.88.012306>
- Gislason, S. R., Wolff-Boenisch, D., Stefansson, A., Oelkers, E. H., Gunnlaugsson, E., Sigurdardottir, H., ... Stute, M. (2010). Mineral sequestration of carbon dioxide in basalt: A pre-injection overview of the CarbFix project. *International Journal of Greenhouse Gas Control*, 4(3), 537–545.
<https://doi.org/10.1016/j.ijggc.2009.11.013>
- Goff, F., & Lackner, K. S. (1998). Carbon dioxide sequestering using ultramafic rocks. *Environmental Geosciences*, 5(3), 89 LP – 101.
<https://doi.org/10.1046/j.1526-0984.1998.0a8014.x>
- Goldsby, D. L., & Tullis, T. E. (2002). Low frictional strength of quartz rocks at subseismic slip rates. *Geophysical Research Letters*, 29(17), 1844.
<https://doi.org/10.1029/2002GL015240>

- Grandstaff, D. E. (1978). Changes in surface area and morphology and the mechanism of forsterite dissolution. *Geochimica et Cosmochimica Acta*, 42(12), 1899–1901. [https://doi.org/10.1016/0016-7037\(78\)90245-4](https://doi.org/10.1016/0016-7037(78)90245-4)
- Grove, T. L., Till, C. B., Lev, E., Chatterjee, N., & Médard, E. (2009). Kinematic variables and water transport control the formation and location of arc volcanoes. *Nature*. <https://doi.org/10.1038/nature08044>
- Gu, J.-C., Rice, J. R., Ruina, A. L., & Tse, S. T. (1984). Slip motion and stability of a single degree of freedom elastic system with rate and state dependent friction. *Journal of the Mechanics and Physics of Solids*, 32(3), 167–196. [https://doi.org/10.1016/0022-5096\(84\)90007-3](https://doi.org/10.1016/0022-5096(84)90007-3)
- Gürsoy, D., De Carlo, F., Xiao, X., & Jacobsen, C. (2014). TomoPy: A framework for the analysis of synchrotron tomographic data. *Journal of Synchrotron Radiation*, 21(5), 1188–1193. <https://doi.org/10.1107/S1600577514013939>
- Gutenberg, B., & Richter, C. F. (1956). Magnitude and energy of earthquakes. *Annals of Geophysics*, 9(1), 1–15.
- Handin, J., Hager, R., Friedman, M., & Feather, J. N. (1963). Experimental Deformation of Sedimentary Rocks Under Confining Pressure: Pore Pressure Tests. *AAPG Bulletin*, 47. <https://doi.org/10.1306/BC743A87-16BE-11D7-8645000102C1865D>
- Hanks, T. C., & Kanamori, H. (1979). A moment magnitude scale. In *Journal of Geophysical Research B: Solid Earth*. <https://doi.org/10.1029/JB084iB05p02348>
- Hansen, L. D., Dipple, G. M., Gordon, T. M., & Kellett, D. A. (2005). Carbonated serpentinite (listwanite) at Atlin, British Columbia: A geological analogue to carbon dioxide sequestration. *Canadian Mineralogist*, 43(1), 225–239. <https://doi.org/10.2113/gscanmin.43.1.225>
- den Hartog, S. A. M., Saffer, D. M., & Spiers, C. J. (2014). The roles of quartz and water in controlling unstable slip in phyllosilicate-rich megathrust fault gouges. *Earth, Planets and Space*, 66(78), 1–9. <https://doi.org/10.1186/1880-5981-66-78>
- He, H., Jin, X., Jing, F., & Ahrens, T. J. (1996). Characteristic of dynamic tensile fracture in augite-peridotite. In *AIP Conference Proceedings* (Vol. 370, pp. 593–596). AIP. <https://doi.org/10.1063/1.50630>
- Heard, H. C. (1960). Chapter 7: Transition from Brittle Fracture to Ductile Flow in Solenhofen Limestone as a Function of Temperature, Confining Pressure, and Interstitial Fluid Pressure. *Geological Society of America Memoirs*. <https://doi.org/10.1130/MEM79-p193>
- Heilbronner, R., & Barrett, S. (2014). *Image Analysis in Earth Sciences. Image*

Analysis in Earth Sciences: Microstructures and Textures of Earth Materials. Berlin, Heidelberg: Springer Berlin Heidelberg. <https://doi.org/10.1007/978-3-642-10343-8>

- Heise, W., Caldwell, T. G., Bannister, S., Bertrand, E. A., Ogawa, Y., Bennie, S. L., & Ichihara, H. (2017). Mapping subduction interface coupling using magnetotellurics: Hikurangi margin, New Zealand. *Geophysical Research Letters*, 1–6. <https://doi.org/10.1002/2017GL074641>
- Heise, W., Caldwell, T. G., Bertrand, E. A., Hill, G. J., Bennie, S. L., & Ogawa, Y. (2013). Changes in electrical resistivity track changes in tectonic plate coupling. *Geophysical Research Letters*. <https://doi.org/10.1002/grl.50959>
- Helmons, R. L. J., Miedema, S. A., & van Rhee, C. (2016). Simulating hydro mechanical effects in rock deformation by combination of the discrete element method and the smoothed particle method. *International Journal of Rock Mechanics and Mining Sciences*. <https://doi.org/10.1016/j.ijrmms.2016.04.018>
- Hirauchi, K., den Hartog, S. A. M., & Spiers, C. J. (2013). Weakening of the slab-mantle wedge interface induced by metasomatic growth of talc. *Geology*, 41(1), 75–78. <https://doi.org/10.1130/G33552.1>
- Hirose, H., & Obara, K. (2010). Recurrence behavior of short-term slow slip and correlated nonvolcanic tremor episodes in western Shikoku, southwest Japan. *Journal of Geophysical Research: Solid Earth*. <https://doi.org/10.1029/2008JB006050>
- Hooper, E. C. D. (1991). Fluid migration along growth faults in compacting sediments. *Journal of Petroleum Geology*. <https://doi.org/10.1111/j.1747-5457.1991.tb00360.x>
- Hövelmann, J., Austrheim, H., & Jamtveit, B. (2012). Microstructure and porosity evolution during experimental carbonation of a natural peridotite. *Chemical Geology*, 334, 254–265. <https://doi.org/10.1016/j.chemgeo.2012.10.025>
- Hubbert, M. K., & Rubey, W. W. (1959). Role of fluid pressure in mechanics of overthrust faulting: I. Mechanics of fluid-filled porous solids and its application to overthrust faulting. *Bulletin of the Geological Society of America*. [https://doi.org/10.1130/0016-7606\(1959\)70\[115:ROFPIM\]2.0.CO;2](https://doi.org/10.1130/0016-7606(1959)70[115:ROFPIM]2.0.CO;2)
- Ikari, M. J., Marone, C., Saffer, D. M., & Kopf, A. J. (2013). Slip weakening as a mechanism for slow earthquakes. *Nature Geoscience*. <https://doi.org/10.1038/ngeo1818>
- Ikari, M. J., Saffer, D. M., & Marone, C. (2009). Frictional and hydrologic properties of clay-rich fault gouge. *Journal of Geophysical Research: Solid Earth*, 114(5), 1–18. <https://doi.org/10.1029/2008JB006089>

- Ikari, M. J., Marone, C., & Saffer, D. M. (2011). On the relation between fault strength and frictional stability. *Geology*, 39(1), 83–86. <https://doi.org/10.1130/G31416.1>
- Ito, Y., Obara, K., Matsuzawa, T., & Maeda, T. (2009). Very low frequency earthquakes related to small asperities on the plate boundary interface at the locked to aseismic transition. *Journal of Geophysical Research: Solid Earth*. <https://doi.org/10.1029/2008JB006036>
- Ito, Y., & Obara, K. (2006). Dynamic deformation of the accretionary prism excites very low frequency earthquakes. *Geophysical Research Letters*. <https://doi.org/10.1029/2005GL025270>
- Iyer, K., Jamtveit, B., Mathiesen, J., Malthe-Sørenssen, A., & Feder, J. (2008). Reaction-assisted hierarchical fracturing during serpentinization. *Earth and Planetary Science Letters*, 267(3–4), 503–516. <https://doi.org/10.1016/j.epsl.2007.11.060>
- Jaeger, J. C. (1969). *Elasticity, Fracture and Flow : with Engineering and Geological Applications*. Springer Netherlands.
- Jamtveit, B., Putnis, C. V., & Malthe-Sørenssen, A. (2009). Reaction induced fracturing during replacement processes. *Contributions to Mineralogy and Petrology*, 157(1), 127–133. <https://doi.org/10.1007/s00410-008-0324-y>
- Jamtveit, B., Kobchenko, M., Austrheim, H., Malthe-Sørenssen, A., Røyne, A., & Svensen, H. (2011). Porosity evolution and crystallization-driven fragmentation during weathering of andesite. *Journal of Geophysical Research: Solid Earth*, 116(12), 1–12. <https://doi.org/10.1029/2011JB008649>
- Johannes, W. (1969). An experimental investigation of the system MgO-SiO₂-H₂O-CO₂. *American Journal of Science*, 267(9), 1083–1104. <https://doi.org/10.2475/ajs.267.9.1083>
- Kaestner, A., Lehmann, E., & Stampanoni, M. (2008). Imaging and image processing in porous media research. *Advances in Water Resources*, 31(9), 1174–1187. <https://doi.org/10.1016/j.advwatres.2008.01.022>
- Kanakiya, S., Adam, L., Esteban, L., Rowe, M. C., & Shane, P. (2017). Dissolution and secondary mineral precipitation in basalts due to reactions with carbonic acid. *Journal of Geophysical Research: Solid Earth*, 122(6), 4312–4327. <https://doi.org/10.1002/2017JB014019>
- Kato, A., Iidaka, T., Ikuta, R., Yoshida, Y., Katsumata, K., Iwasaki, T., ... Hirata, N. (2010). Variations of fluid pressure within the subducting oceanic crust and slow earthquakes. *Geophysical Research Letters*. <https://doi.org/10.1029/2010GL043723>

- Kelemen, P. B., Matter, J. M., Streit, E. E., Rudge, J. F., Curry, W. B., & Blusztajn, J. (2011). Rates and Mechanisms of Mineral Carbonation in Peridotite: Natural Processes and Recipes for Enhanced, in situ CO₂ Capture and Storage. *Annual Review of Earth and Planetary Sciences*, 39(1), 545–576. <https://doi.org/10.1146/annurev-earth-092010-152509>
- Kelemen, P. B., & Hirth, G. (2012). Reaction-driven cracking during retrograde metamorphism: Olivine hydration and carbonation. *Earth and Planetary Science Letters*, 345–348, 81–89. <https://doi.org/10.1016/j.epsl.2012.06.018>
- Kelemen, P. B., Savage, H., & Hirth, G. (2013). Reaction-Driven Cracking During Mineral Hydration, Carbonation and Oxidation. In *Poromechanics V* (Vol. c, pp. 823–826). Reston, VA: American Society of Civil Engineers. <https://doi.org/10.1061/9780784412992.099>
- Kelemen, P. B., & Matter, J. M. (2008). In situ carbonation of peridotite for CO₂ storage. *Proceedings of the National Academy of Sciences*, 105(45), 17295–17300. <https://doi.org/10.1073/pnas.0805794105>
- Kilgore, B. D., Blanpied, M. L., & Dieterich, J. H. (1993). Velocity dependent friction of granite over a wide range of conditions. *Geophysical Research Letters*. <https://doi.org/10.1029/93GL00368>
- King, H. E., Plümper, O., & Putnis, A. (2010). Effect of Secondary Phase Formation on the Carbonation of Olivine. *Environmental Science & Technology*, 44(16), 6503–6509. <https://doi.org/10.1021/es9038193>
- Kirby, S. H. (1983). Rheology of the lithosphere. *Reviews of Geophysics*. <https://doi.org/10.1029/RG021i006p01458>
- Kirby, S. H., & Kronenberg, A. K. (1987). Rheology of the lithosphere: Selected topics. *Reviews of Geophysics*. <https://doi.org/10.1029/RG025i006p01219>
- Kitajima, H., & Saffer, D. M. (2012). Elevated pore pressure and anomalously low stress in regions of low frequency earthquakes along the Nankai Trough subduction megathrust. *Geophysical Research Letters*. <https://doi.org/10.1029/2012GL053793>
- Kodaira, S., Iidaka, T., Kato, A., Park, J. O., Iwasaki, T., & Kaneda, Y. (2004). High pore fluid pressure may cause silent slip in the Nankai Trough. *Science*. <https://doi.org/10.1126/science.1096535>
- Kranz, R. L., Harris, W. J., & Carter, N. L. (1982). Static fatigue of granite at 200°C. *Geophysical Research Letters*. <https://doi.org/10.1029/GL009i001p00001>
- Kronenberg, A. K., Kirby, S. H., & Pinkston, J. (1990). Basal slip and mechanical anisotropy of biotite. *Journal of Geophysical Research*.

<https://doi.org/10.1029/jb095ib12p19257>

- Leeman, J. R., Saffer, D. M., Scuderi, M. M., & Marone, C. (2016). Laboratory observations of slow earthquakes and the spectrum of tectonic fault slip modes. *Nature Communications*, 7, 11104. <https://doi.org/10.1038/ncomms11104>
- Lisabeth, H. P., Zhu, W., Xing, T., & De Andrade, V. (2017). Dissolution-Assisted Pattern Formation During Olivine Carbonation. *Geophysical Research Letters*, 44(19), 9622–9631. <https://doi.org/10.1002/2017GL074393>
- Lisabeth, H. P., Zhu, W., Kelemen, P. B., & Ilgen, A. G. (2017). Experimental evidence for chemo-mechanical coupling during carbon mineralization in ultramafic rocks. *Earth and Planetary Science Letters*, 474, 355–367. <https://doi.org/10.1016/j.epsl.2017.06.045>
- Lisabeth, H. P., & Zhu, W. (2015). Effect of temperature and pore fluid on the strength of porous limestone. *Journal of Geophysical Research B: Solid Earth*, 120(9), 6191–6208. <https://doi.org/10.1002/2015JB012152>
- Liu, Y., & Rice, J. R. (2007). Spontaneous and triggered aseismic deformation transients in a subduction fault model. *Journal of Geophysical Research: Solid Earth*. <https://doi.org/10.1029/2007JB004930>
- Lockner, D. A. (1993). The role of acoustic emission in the study of rock fracture. *International Journal of Rock Mechanics and Mining Sciences And*. [https://doi.org/10.1016/0148-9062\(93\)90041-B](https://doi.org/10.1016/0148-9062(93)90041-B)
- Lockner, D. A., & Beeler, N. M. (2002). 32 Rock failure and earthquakes. In *International Geophysics*. [https://doi.org/10.1016/S0074-6142\(02\)80235-2](https://doi.org/10.1016/S0074-6142(02)80235-2)
- Lockner, D. A., Summers, R., & Byerlee, J. D. (1986). Effects of temperature and sliding rate on frictional strength of granite. *Pure and Applied Geophysics PAGEOPH*. <https://doi.org/10.1007/BF00877211>
- Lockner, D. A., Byerlee, J. D., Kuksenko, V., Ponomarev, A., & Sidorin, A. (1992). Observations of Quasistatic Fault Growth from Acoustic Emissions. *International Geophysics*. [https://doi.org/10.1016/S0074-6142\(08\)62813-2](https://doi.org/10.1016/S0074-6142(08)62813-2)
- Lowry, A. R. (2006). Resonant slow fault slip in subduction zones forced by climatic load stress. *Nature*. <https://doi.org/10.1038/nature05055>
- Macdonald, A. H., & Fyfe, W. S. (1985). Rate of serpentinization in seafloor environments. *Tectonophysics*, 116(1–2), 123–135. [https://doi.org/10.1016/0040-1951\(85\)90225-2](https://doi.org/10.1016/0040-1951(85)90225-2)
- Makhnenko, R. Y., & Labuz, J. F. (2015). Dilatant hardening of fluid-saturated sandstone. *Journal of Geophysical Research: Solid Earth*, 120(2), 909–922. <https://doi.org/10.1002/2014JB011287>

- Mani, D., Nirmal Charan, S., & Kumar, B. (2008). Assessment of carbon dioxide sequestration potential of ultramafic rocks in the greenstone belts of southern India. *Current Science*, *94*(1), 53–60.
- Marone, C. (1998). Laboratory-derived friction laws and their application to seismic faulting. *Annual Review of Earth and Planetary Sciences*, *26*(1), 643–696. <https://doi.org/10.1146/annurev.earth.26.1.643>
- Marone, C., & Kilgore, B. (1993). Scaling of the critical slip distance for seismic faulting with shear strain in fault zones. *Nature*. <https://doi.org/10.1038/362618a0>
- Mclaskey, G. C., & Yamashita, F. (2017). Slow and fast ruptures on a laboratory fault controlled by loading characteristics. *Journal of Geophysical Research: Solid Earth*, *122*(5), 3719–3738. <https://doi.org/10.1002/2016JB013681>
- Moore, D. E., & Lockner, D. A. (1995). The role of microcracking in shear-fracture propagation in granite. *Journal of Structural Geology*. [https://doi.org/10.1016/0191-8141\(94\)E0018-T](https://doi.org/10.1016/0191-8141(94)E0018-T)
- Moore, Diane E., Lockner, D. A., Summers, R., Ma, S., & Byerlee, J. D. (1996). Strength of crisolite-serpentine gouge under hydrothermal conditions: Can it explain a weak San Andreas fault? *Geology*, *24*(11), 1041–1044. [https://doi.org/10.1130/0091-7613\(1996\)024<1041](https://doi.org/10.1130/0091-7613(1996)024<1041)
- Moore, Diane E., Lockner, D. A., Ma, S., Summers, R., & Byerlee, J. D. (1997). Strengths of serpentine gouges at elevated temperatures. *Journal of Geophysical Research: Solid Earth*, *102*(B7), 14787–14801. <https://doi.org/10.1029/97JB00995>
- Moore, Diane E., Lockner, D. A., Tanaka, H., & Iwata, K. (2004). The Coefficient of Friction of Chrysotile Gouge at Seismogenic Depths. *International Geology Review*, *46*(5), 385–398. <https://doi.org/10.2747/0020-6814.46.5.385>
- Moore, Diane E., & Lockner, D. A. (2011). Frictional strengths of talc-serpentine and talc-quartz mixtures. *Journal of Geophysical Research: Solid Earth*. <https://doi.org/10.1029/2010JB007881>
- Morrow, C. A., & Byerlee, J. D. (1989). Experimental studies of compaction and dilatancy during frictional sliding on faults containing gouge. *Journal of Structural Geology*. [https://doi.org/10.1016/0191-8141\(89\)90100-4](https://doi.org/10.1016/0191-8141(89)90100-4)
- Morrow, C. A., Radney, B., & Byerlee, J. D. (1992). Frictional Strength and the Effective Pressure Law of Montmorillonite and Illite Clays. *International Geophysics*. [https://doi.org/10.1016/S0074-6142\(08\)62815-6](https://doi.org/10.1016/S0074-6142(08)62815-6)
- Nakamura, M., & Sunagawa, N. (2015). Activation of very low frequency

- earthquakes by slow slip events in the Ryukyu Trench. *Geophysical Research Letters*. <https://doi.org/10.1002/2014GL062929>
- Nasir, S., Al Sayigh, A. R., Al Harthy, A., Al-Khribash, S., Al-Jaaidi, O., Musllam, A., ... Al-Bu'saidi, S. (2007). Mineralogical and geochemical characterization of listwaenite from the Semail Ophiolite, Oman. *Chemie Der Erde - Geochemistry*, 67(3), 213–228. <https://doi.org/10.1016/j.chemer.2005.01.003>
- Niemeijer, A., & Collettini, C. (2013). Frictional Properties of a Low-Angle Normal Fault Under In Situ Conditions: Thermally-Activated Velocity Weakening. *Pure and Applied Geophysics*, 171(10), 2641–2664. <https://doi.org/10.1007/s00024-013-0759-6>
- Niemeijer, A., Marone, C., & Elsworth, D. (2010). Frictional strength and strain weakening in simulated fault gouge: Competition between geometrical weakening and chemical strengthening. *Journal of Geophysical Research: Solid Earth*. <https://doi.org/10.1029/2009JB000838>
- van Noort, R., Wolterbeek, T. K. T., Drury, M. R., Kandianis, M., & Spiers, C. J. (2017). The Force of Crystallization and Fracture Propagation during In-Situ Carbonation of Peridotite. *Minerals*, 7(10), 190. <https://doi.org/10.3390/min7100190>
- Obara, K. (2002). Nonvolcanic deep tremor associated with subduction in southwest Japan. *Science*. <https://doi.org/10.1126/science.1070378>
- Okazaki, K., & Hirth, G. (2016). Dehydration of lawsonite could directly trigger earthquakes in subducting oceanic crust. *Nature*, 530(7588), 81–84. <https://doi.org/10.1038/nature16501>
- Okazaki, K., & Katayama, I. (2015). Slow stick slip of antigorite serpentinite under hydrothermal conditions as a possible mechanism for slow earthquakes. *Geophysical Research Letters*, 42(4), 1099–1104. <https://doi.org/10.1002/2014GL062735>
- Okazaki, K., Katayama, I., & Takahashi, M. (2013). Effect of pore fluid pressure on the frictional strength of antigorite serpentinite. *Tectonophysics*, 583, 49–53. <https://doi.org/10.1016/j.tecto.2012.10.017>
- Orowan, E. (1944). The fatigue of glass under stress. *Nature*. <https://doi.org/10.1038/154341a0>
- Ougier-Simonin, A., & Zhu, W. (2013). Effects of pore fluid pressure on slip behaviors: An experimental study. *Geophysical Research Letters*, 40(11), 2619–2624. <https://doi.org/10.1002/grl.50543>
- Ougier-Simonin, A., & Zhu, W. (2015). Effect of pore pressure buildup on slowness

- of rupture propagation. *Journal of Geophysical Research: Solid Earth*, 120(12), 7966–7985. <https://doi.org/10.1002/2015JB012047>
- Pabst, W., & Gregorová, E. (2013). Elastic properties of silica polymorphs—a review. *Ceramics - Silikaty*.
- Park, J. O., Tsuru, T., Takahashi, N., Hori, T., Kodaira, S., Nakanishi, A., ... Kaneda, Y. (2002). A deep strong reflector in the Nankai accretionary wedge from multichannel seismic data: Implications for underplating and interseismic shear stress release. *Journal of Geophysical Research: Solid Earth*. <https://doi.org/10.1029/2001jb000262>
- Park, J. O., Fujie, G., Wijerathne, L., Hori, T., Kodaira, S., Fukao, Y., ... Taira, A. (2010). A low-velocity zone with weak reflectivity along the Nankai subduction zone. *Geology*. <https://doi.org/10.1130/G30205.1>
- Passelègue, F. X., Schubnel, A., Nielsen, S., Bhat, H. S., Deldicque, D., & Madariaga, R. (2016). Dynamic rupture processes inferred from laboratory microearthquakes. *Journal of Geophysical Research: Solid Earth*. <https://doi.org/10.1002/2015JB012694>
- Paterson, M. S., & Wong, T. (2005). *Experimental rock deformation - The brittle field*. *Experimental Rock Deformation - The Brittle Field*. <https://doi.org/10.1007/b137431>
- Peacock, S. M., Christensen, N. I., Bostock, M. G., & Audet, P. (2011). High pore pressures and porosity at 35 km depth in the Cascadia subduction zone. *Geology*. <https://doi.org/10.1130/G31649.1>
- Peng, S., & Johnson, A. M. (1972). Crack growth and faulting in cylindrical specimens of chelmsford granite. *International Journal of Rock Mechanics and Mining Sciences And*. [https://doi.org/10.1016/0148-9062\(72\)90050-2](https://doi.org/10.1016/0148-9062(72)90050-2)
- Peng, Z., & Gomberg, J. (2010). An integrated perspective of the continuum between earthquakes and slow-slip phenomena. *Nature Geoscience*. <https://doi.org/10.1038/ngeo940>
- Peuble, S., Andreani, M., Gouze, P., Pollet-Villard, M., Reynard, B., & Van de Moortèle, B. (2018). Multi-scale characterization of the incipient carbonation of peridotite. *Chemical Geology*, 476, 150–160. <https://doi.org/10.1016/j.chemgeo.2017.11.013>
- Plummer, P. S., & Gostin, V. a. (1981). Shrinkage cracks: desiccation or syneresis? *Journal of Sedimentary Petrology*. <https://doi.org/10.1306/212F7E4B-2B24-11D7-8648000102C1865D>
- Poiseuille, J. L. M. (1844). *Recherches experimentales sur le mouvement des liquides*

- dans les tubes de tres petits diametres* (Vol. 11). Imprimerie Royale. Retrieved from <https://www.irphe.fr/~clanet/otherpaperfile/articles/Poiseuille/%0Ahttps://www.irphe.fr/~clanet/otherpaperfile/articles/Poiseuille/poiseuille1840a.pdf>
- Power, I. M., Harrison, A. L., Dipple, G. M., Wilson, S. A., Kelemen, P. B., Hitch, M., & Southam, G. (2013). Carbon Mineralization: From Natural Analogues to Engineered Systems. *Reviews in Mineralogy and Geochemistry*, 77(1), 305–360. <https://doi.org/10.2138/rmg.2013.77.9>
- Proctor, B. P., Mitchell, T. M., Hirth, G., Goldsby, D. L., Zorzi, F., Platt, J. D., & Di Toro, G. (2014). Dynamic weakening of serpentinite gouges and bare surfaces at seismic slip rates. *Journal of Geophysical Research: Solid Earth*, 119(11), 8107–8131. <https://doi.org/10.1002/2014JB011057>
- Rabinowicz, E. (1958). The intrinsic variables affecting the stick-slip process. *Proceedings of the Physical Society*. <https://doi.org/10.1088/0370-1328/71/4/316>
- Rabinowicz, E. (1965). *Friction and Wear of Materials*. Wiley, New York.
- Raleigh, B., & Marone, C. (1986). Dilatancy of quartz gouge in pure shear (pp. 1–10). <https://doi.org/10.1029/GM036p0001>
- Rao, M. V. M. S., & Raman, Y. V. (1974). Dilatant behaviour of ultramafic rocks during fracture. *International Journal of Rock Mechanics and Mining Sciences And*. [https://doi.org/10.1016/0148-9062\(74\)90886-9](https://doi.org/10.1016/0148-9062(74)90886-9)
- Rathbun, A. P., & Marone, C. (2013). Symmetry and the critical slip distance in rate and state friction laws. *Journal of Geophysical Research: Solid Earth*. <https://doi.org/10.1002/jgrb.50224>
- Reches, Z., & Lockner, D. A. (1994). Nucleation and growth of faults in brittle rocks. *Journal of Geophysical Research: Solid Earth*. <https://doi.org/10.1029/94jb00115>
- Reid, H. F. (1911). The Elastic-Rebound Theory of Earthquakes. *Bulletin of the Department of Geology, University of California Publications*.
- Reinen, L. A., Weeks, J. D., & Tullis, T. E. (1991). The frictional behavior of serpentinite: Implications for aseismic creep on shallow crustal faults. *Geophysical Research Letters*, 18(10), 1921–1924. <https://doi.org/10.1029/91GL02367>
- Reinen, L. A., Weeks, J. D., & Tullis, T. E. (1994). The frictional behavior of lizardite and antigorite serpentinites: Experiments, constitutive models, and implications for natural faults. *Pure and Applied Geophysics PAGEOPH*, 143(1–3), 317–358. <https://doi.org/10.1007/BF00874334>

- Rice, J. R. (1975). On the stability of dilatant hardening for saturated rock masses. *Journal of Geophysical Research*. <https://doi.org/10.1029/JB080i011p01531>
- Rice, J. R. (1978). Thermodynamics of the quasi-static growth of Griffith cracks. *Journal of the Mechanics and Physics of Solids*. [https://doi.org/10.1016/0022-5096\(78\)90014-5](https://doi.org/10.1016/0022-5096(78)90014-5)
- Rice, J. R., & Cleary, M. P. (1976). Some basic stress diffusion solutions for fluid-saturated elastic porous media with compressible constituents. *Reviews of Geophysics*. <https://doi.org/10.1029/RG014i002p00227>
- Rice, J. R., & Rudnicki, J. W. (1979). Earthquake precursory effects due to pore fluid stabilization of a weakening fault zone. In *Journal of Geophysical Research: Solid Earth*. <https://doi.org/10.1029/JB084iB05p02177>
- Rice, J. R., & Ruina, A. L. (1983). Stability of Steady Frictional Slipping. *Journal of Applied Mechanics*, 50(2), 343. <https://doi.org/10.1115/1.3167042>
- Rouméjon, S., & Cannat, M. (2014). Serpentinization of mantle-derived peridotites at mid-ocean ridges: Mesh texture development in the context of tectonic exhumation. *Geochemistry, Geophysics, Geosystems*, 15(6), 2354–2379. <https://doi.org/10.1002/2013GC005148>
- Røyne, A., & Jamtveit, B. (2015). Pore-Scale Controls on Reaction-Driven Fracturing. *Reviews in Mineralogy and Geochemistry*, 80(1), 25–44. <https://doi.org/10.2138/rmg.2015.80.02>
- Rubin, A. M. (2008). Episodic slow slip events and rate-and-state friction. *Journal of Geophysical Research: Solid Earth*, 113(11), 1–18. <https://doi.org/10.1029/2008JB005642>
- Rudge, J. F., Kelemen, P. B., & Spiegelman, M. (2010). A simple model of reaction-induced cracking applied to serpentinization and carbonation of peridotite. *Earth and Planetary Science Letters*, 291(1–4), 215–227. <https://doi.org/10.1016/j.epsl.2010.01.016>
- Rudnick, R. L., & Gao, S. (2013). Composition of the Continental Crust. In *Treatise on Geochemistry: Second Edition*. <https://doi.org/10.1016/B978-0-08-095975-7.00301-6>
- Rudnicki, J. W. (1984). Effects of dilatant hardening on the development of concentrated shear deformation in fissured rock masses. *Journal of Geophysical Research*. <https://doi.org/10.1029/JB089iB11p09259>
- Rudnicki, J. W., & Chen, C. H. (1988). Stabilization of rapid frictional slip on a weakening fault by dilatant hardening. *Journal of Geophysical Research*. <https://doi.org/10.1029/JB093iB05p04745>

- Rudnicki, J. W., & Rice, J. R. (1975). Conditions for the localization of deformation in pressure-sensitive dilatant materials. *Journal of the Mechanics and Physics of Solids*. [https://doi.org/10.1016/0022-5096\(75\)90001-0](https://doi.org/10.1016/0022-5096(75)90001-0)
- Ruina, A. (1983). Slip instability and state variable friction laws. *Journal of Geophysical Research: Solid Earth*, 88(B12), 10359–10370. <https://doi.org/10.1029/JB088iB12p10359>
- Rutter, E. H. (1972). The influence of interstitial water on the rheological behaviour of calcite rocks. *Tectonophysics*. [https://doi.org/10.1016/0040-1951\(72\)90003-0](https://doi.org/10.1016/0040-1951(72)90003-0)
- Rutter, E. H. (1974). The influence of temperature, strain rate and interstitial water in the experimental deformation of calcite rocks. *Tectonophysics*. [https://doi.org/10.1016/0040-1951\(74\)90089-4](https://doi.org/10.1016/0040-1951(74)90089-4)
- Rutter, E. H., & Hackston, A. (2017). On the effective stress law for rock-on-rock frictional sliding, and fault slip triggered by means of fluid injection. *Philosophical Transactions of the Royal Society A: Mathematical, Physical and Engineering Sciences*. <https://doi.org/10.1098/rsta.2016.0001>
- Saffer, D. M. (2017). Mapping fluids to subduction megathrust locking and slip behavior. *Geophysical Research Letters*. <https://doi.org/10.1002/2017GL075381>
- Saldi, G. D., Jordan, G., Schott, J., & Oelkers, E. H. (2009). Magnesite growth rates as a function of temperature and saturation state. *Geochimica et Cosmochimica Acta*, 73(19), 5646–5657. <https://doi.org/10.1016/j.gca.2009.06.035>
- Sammis, C. G., & Ashby, M. F. (1986). The failure of brittle porous solids under compressive stress states. *Acta Metallurgica*. [https://doi.org/10.1016/0001-6160\(86\)90087-8](https://doi.org/10.1016/0001-6160(86)90087-8)
- Samuelson, J., Elsworth, D., & Marone, C. (2009). Shear-induced dilatancy of fluid-saturated faults: Experiment and theory. *Journal of Geophysical Research: Solid Earth*, 114(12), 1–15. <https://doi.org/10.1029/2008JB006273>
- Sawai, M., Niemeijer, A., Plümpner, O., Hirose, T., & Spiers, C. J. (2016). Nucleation of frictional instability caused by fluid pressurization in subducted blueschist. *Geophysical Research Letters*, 43(6), 2543–2551. <https://doi.org/10.1002/2015GL067569>
- Scherer, G. W. (2004). Stress from crystallization of salt. *Cement and Concrete Research*, 34(9), 1613–1624. <https://doi.org/10.1016/j.cemconres.2003.12.034>
- Scholz, C. (1998). Earthquakes and friction laws. *Nature*, 391(6662), 37–42. <https://doi.org/10.1038/34097>
- Scholz, C. (2002). *The Mechanics of Earthquakes and Faulting*. Cambridge University Press.

- Scholz, C., Molnar, P., & Johnson, T. (1972). Detailed studies of frictional sliding of granite and implications for the earthquake mechanism. *Journal of Geophysical Research*, 77(32), 6392–6406. <https://doi.org/10.1029/JB077i032p06392>
- Scott, D. R., Lockner, D. A., Byerlee, J. D., & Sammis, C. G. (1994). Triaxial testing of Lopez Fault gouge at 150 MPa mean effective stress. *Pure and Applied Geophysics PAGEOPH*, 142(3–4), 749–775. <https://doi.org/10.1007/BF00876063>
- Scuderi, M. M., & Collettini, C. (2016). The role of fluid pressure in induced vs. triggered seismicity: insights from rock deformation experiments on carbonates. *Scientific Reports*, 6(1), 24852. <https://doi.org/10.1038/srep24852>
- Scuderi, M. M., Collettini, C., & Marone, C. (2017). Frictional stability and earthquake triggering during fluid pressure stimulation of an experimental fault. *Earth and Planetary Science Letters*, 477, 84–96. <https://doi.org/10.1016/j.epsl.2017.08.009>
- Segall, P., Rubin, A. M., Bradley, A. M., & Rice, J. R. (2010). Dilatant strengthening as a mechanism for slow slip events. *Journal of Geophysical Research: Solid Earth*, 115(12), 1–37. <https://doi.org/10.1029/2010JB007449>
- Shelly, D. R. (2010). Migrating tremors illuminate complex deformation beneath the seismogenic San Andreas fault. *Nature*. <https://doi.org/10.1038/nature08755>
- Shelly, D. R., Beroza, G. C., Ide, S., & Nakamura, S. (2006). Low-frequency earthquakes in Shikoku, Japan, and their relationship to episodic tremor and slip. *Nature*. <https://doi.org/10.1038/nature04931>
- Sibson, R. H. (1973). Interactions between Temperature and Pore-Fluid Pressure during Earthquake Faulting and a Mechanism for Partial or Total Stress Relief. *Nature Physical Science*. <https://doi.org/10.1038/physci243066a0>
- Sibson, R. H., & Rowland, J. V. (2003). Stress, fluid pressure and structural permeability in seismogenic crust, North Island, New Zealand. *Geophysical Journal International*. <https://doi.org/10.1046/j.1365-246X.2003.01965.x>
- Singh, S. K. (1988). Relationship among fatigue strength, mean grain size and compressive strength of a rock. *Rock Mechanics and Rock Engineering*, 21(4), 271–276. <https://doi.org/10.1007/BF01020280>
- Song, T. R. A., Helmberger, D. V., Brudzinski, M. R., Clayton, R. W., Davis, P., Pérez-Campos, X., & Singh, S. K. (2009). Subducting slab ultra-slow velocity layer coincident with silent earthquakes in southern Mexico. *Science*. <https://doi.org/10.1126/science.1167595>
- Takahashi, M., Uehara, S. I., Mizoguchi, K., Shimizu, I., Okazaki, K., & Masuda, K.

- (2011). On the transient response of serpentine (antigorite) gouge to stepwise changes in slip velocity under high-temperature conditions. *Journal of Geophysical Research: Solid Earth*. <https://doi.org/10.1029/2010JB008062>
- Tauzin, B., Reynard, B., Perrillat, J.-P., Debayle, E., & Bodin, T. (2017). Deep crustal fracture zones control fluid escape and the seismic cycle in the Cascadia subduction zone. *Earth and Planetary Science Letters*, *460*, 1–11. <https://doi.org/10.1016/j.epsl.2016.12.007>
- Tembe, S., Lockner, D. A., Solum, J. G., Morrow, C. A., Wong, T., & Moore, D. E. (2006). Frictional strength of cuttings and core from SAFOD drillhole phases 1 and 2. *Geophysical Research Letters*, *33*(23), L23307. <https://doi.org/10.1029/2006GL027626>
- Tembe, S., Lockner, D. A., & Wong, T. (2010). Effect of clay content and mineralogy on frictional sliding behavior of simulated gouges: Binary and ternary mixtures of quartz, illite, and montmorillonite. *Journal of Geophysical Research: Solid Earth*, *115*(3), 1–22. <https://doi.org/10.1029/2009JB006383>
- Terzaghi, K. (1943). *Theoretical soil mechanics*. London: Chapman And Hall, Limited.
- Tinti, E., Scuderi, M. M., Scognamiglio, L., Di Stefano, G., Marone, C., & Collettini, C. (2016). On the evolution of elastic properties during laboratory stick-slip experiments spanning the transition from slow slip to dynamic rupture. *Journal of Geophysical Research: Solid Earth*, *121*(12), 8569–8594. <https://doi.org/10.1002/2016JB013545>
- Ulven, O. I., Storheim, H., Austrheim, H., & Malthe-Sørensen, A. (2014). Fracture initiation during volume increasing reactions in rocks and applications for CO₂ sequestration. *Earth and Planetary Science Letters*, *389*, 132–142. <https://doi.org/10.1016/j.epsl.2013.12.039>
- Velbel, M. A. (2009). Dissolution of olivine during natural weathering. *Geochimica et Cosmochimica Acta*, *73*(20), 6098–6113. <https://doi.org/10.1016/j.gca.2009.07.024>
- Velbel, M. A., & Ranck, J. M. (2008). Etch pits on naturally altered olivine from dunites of the Appalachian Blue Ridge Mountains, North Carolina, USA. *Mineralogical Magazine*, *72*(1), 145–148. <https://doi.org/10.1180/minmag.2008.072.1.145>
- Verberne, B. A., He, C., & Spiers, C. J. (2010). Frictional properties of sedimentary rocks and natural fault gouge from the Longmen Shan fault zone, Sichuan, China. *Bulletin of the Seismological Society of America*. <https://doi.org/10.1785/0120090287>

- Vergnolle, M., Walpersdorf, A., Kostoglodov, V., Tregoning, P., Santiago, J. A., Cotte, N., & Franco, S. I. (2010). Slow slip events in Mexico revised from the processing of 11 year GPS observations. *Journal of Geophysical Research: Solid Earth*. <https://doi.org/10.1029/2009JB006852>
- Walder, J., & Nur, A. (1984). Porosity reduction and crustal pore pressure development. *Journal of Geophysical Research*. <https://doi.org/10.1029/JB089iB13p11539>
- Wech, A. G., & Creager, K. C. (2011). A continuum of stress, strength and slip in the Cascadia subduction zone. *Nature Geoscience*. <https://doi.org/10.1038/ngeo1215>
- Wells, R. K., Xiong, W., Sesti, E., Cui, J., Giammar, D. E., Skemer, P., ... Conradi, M. S. (2017). Spatially-variable carbonation reactions in polycrystalline olivine. *Geochimica et Cosmochimica Acta*, 204, 252–266. <https://doi.org/10.1016/j.gca.2017.02.003>
- Weyl, P. K. (1959). Pressure solution and the force of crystallization: a phenomenological theory. *Journal of Geophysical Research*, 64(11), 2001–2025. <https://doi.org/10.1029/JZ064i011p02001>
- Wilson, M. J. (2004). Weathering of the primary rock-forming minerals: processes, products and rates. *Clay Minerals*, 39(3), 233–266. <https://doi.org/10.1180/0009855043930133>
- Wilson, M. J., & Jones, D. (1983). Lichen weathering of minerals: implications for pedogenesis. *Geological Society, London, Special Publications*, 11(1), 5–12. <https://doi.org/10.1144/GSL.SP.1983.011.01.01>
- Winkler, E. M., & Singer, P. C. (1972). Crystallization pressure of salts in stone and concrete. *Bulletin of the Geological Society of America*, 83(11), 3509–3514. [https://doi.org/10.1130/0016-7606\(1972\)83\[3509:CPOISS\]2.0.CO;2](https://doi.org/10.1130/0016-7606(1972)83[3509:CPOISS]2.0.CO;2)
- Wintsch, R. P., Christoffersen, R., & Kronenberg, A. K. (1995). Fluid-rock reaction weakening of fault zones. *Journal of Geophysical Research*, 100(B7), 13021. <https://doi.org/10.1029/94JB02622>
- Wong, T., Gu, Y., Yanagidani, T., & Zhao, Y. (1992). Chapter 5 Stabilization of Faulting by Cumulative Slip. In *International Geophysics* (Vol. 51, pp. 119–143). Academic Press. [https://doi.org/10.1016/S0074-6142\(08\)62820-X](https://doi.org/10.1016/S0074-6142(08)62820-X)
- Xing, T., Zhu, W., Fousseis, F., & Lisabeth, H. P. (2018). Generating porosity during olivine carbonation via dissolution channels and expansion cracks. *Solid Earth*, 9(4), 879–896. <https://doi.org/10.5194/se-9-879-2018>
- Zhang, S., Tullis, T. E., & Scruggs, V. J. (1999). Permeability anisotropy and pressure dependency of permeability in experimentally sheared gouge materials.

Journal of Structural Geology. [https://doi.org/10.1016/S0191-8141\(99\)00080-2](https://doi.org/10.1016/S0191-8141(99)00080-2)

- Zhang, S., Tullis, T. E., & Scruggs, V. J. (2001). Implications of permeability and its anisotropy in a mica gouge for pore pressures in fault zones. *Tectonophysics*, 335(1–2), 37–50. [https://doi.org/10.1016/S0040-1951\(01\)00044-0](https://doi.org/10.1016/S0040-1951(01)00044-0)
- Zhang, X., & Spiers, C. J. (2005). Compaction of granular calcite by pressure solution at room temperature and effects of pore fluid chemistry. *International Journal of Rock Mechanics and Mining Sciences*. <https://doi.org/10.1016/j.ijrmms.2005.05.017>
- Zhu, W., Fusses, F., Lisabeth, H. P., Xing, T., Xiao, X., De Andrade, V., & Karato, S. (2016). Experimental evidence of reaction-induced fracturing during olivine carbonation. *Geophysical Research Letters*, 43(18), 9535–9543. <https://doi.org/10.1002/2016GL070834>
- Zhu, W., & Wong, T. (1997). The transition from brittle faulting to cataclastic flow: Permeability evolution. *Journal of Geophysical Research: Solid Earth*. <https://doi.org/10.1029/96jb03282>
- Zhu, W., Montési, L. G. J., & Wong, T. (1997). Shear-enhanced compaction and permeability reduction: Triaxial extension tests on porous sandstone. *Mechanics of Materials*, 25(3), 199–214. [https://doi.org/10.1016/S0167-6636\(97\)00011-2](https://doi.org/10.1016/S0167-6636(97)00011-2)
- Ziese, F., Maret, G., & Gasser, U. (2013). Heterogeneous nucleation and crystal growth on curved surfaces observed by real-space imaging. *Journal of Physics Condensed Matter*, 25(37). <https://doi.org/10.1088/0953-8984/25/37/375105>
- Zoback, M. D., & Townend, J. (2001). Implications of hydrostatic pore pressures and high crustal strength for the deformation of intraplate lithosphere. *Tectonophysics*. [https://doi.org/10.1016/S0040-1951\(01\)00091-9](https://doi.org/10.1016/S0040-1951(01)00091-9)
- Zoback, M. D., Zoback, M. Lou, Mount, V. S., Suppe, J., Eaton, J. P., Healy, J. H., ... Wentworth, C. (1987). New Evidence on the State of Stress of the San Andreas Fault System. *Science*. <https://doi.org/10.1126/science.238.4830.1105>